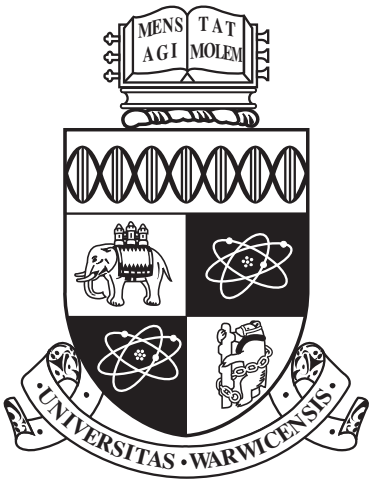

Advanced Electron Microscopy Study of Charged Ferroelectric Domain Walls in Multiferroic $BiFeO_3$

by

Wanbing GE 葛宛兵

Thesis

Submitted to the University of Warwick

for the degree of

Doctor of Philosophy

Department of Physics

July 2023

THE UNIVERSITY OF
WARWICK

Contents

List of Tables

List of Figures

Acknowledgments

This morning, I randomly picked up the book *Lean In* by Sheryl Sandberg, and found this sentence in its preface that gives a neat summary of my PhD and many others: Before I got the right, I got many wrongs. Here I would like to express my sincere appreciation of the help from the following people, without whom I would not have been able to complete this research:

I would like to express my deepest appreciation to my supervisor Prof Ana Sanchez, whose insight and knowledge into electron microscopy and invaluable patience and feedback has steered me through this research. The amazement is hard to forget when her magic-touch corrected the microscope's alignment in seconds where I was stuck for hours. Although she generously offered the recipe and demonstrated it multiple times, I find it hard to copy.

Thanks are owned to Prof Marin Alexe and Prof Richard Beanland for offering their expertise in ferroelectricity and electron microscopy, and more importantly for sharing their curiosity for science. Thanks to Dr Jonathan Peters, Dr James Gott, Prof Quentin Ramasse, and Dr Mingmin Yang for teach me hand-in-hand in the lab and for their patience and time in answering my simple questions. Thanks to the valuable help from the RTP: Dr Yisong Han, Steve Hindmarsh and Steve York, who made it seemingly effortless to run a smooth microscope session. Thanks to the help and company from Ebrima Saho, Dr Reza Kashtiban, Dr Raghavendra Juluri, Dr Aruni Fonseka, Dr Jere Tidey, Prof Peng Wang, Dr Alex Robertson, Dr Michele Conroy, Dr Dorin Rusu, Anton Cleverley, Francisco Alvarado, Yining Xie, Dr Eoin Moynihan and Dr Wen Dong. Thanks to all of you for those wonderful coffee breaks.

The beautiful content from Prof Hans Rosling, Lord Stephen Green and Dr John Campbell has given me good comfort, thus helped the finish of this work and should be mentioned.

Finally, thanks to my father, my mother and my brother. Although during a big part of this PhD, we had to be separated by distance, or by time, your unconditional love has always managed to reach where it is most needed. Wo Ai Ni Men.

Declarations

I declare that this thesis contains an account of my research work carried out at the Department of Physics, University of Warwick, between October 2019 and June 2023 under the supervision of Prof Ana M. Sanchez. The research reported here has not been previously submitted, wholly or in part, at this or any other academic institution for admission to a higher degree.

The work presented (including data generated and analysis) was carried out by the author, except: the diffraction contrast transmission electron microscopy images and converged beam electron diffraction patterns were collected by Prof Richard Beanland and Prof Ana M. Sanchez. The single crystal samples examined in this work were provided by Prof Marin Alexe. The displacement mapping on atomic resolution images was performed by the author using algorithms developed by Dr Jonathan J. P. Peters. The EELS data and high angle annular dark field images were collected by Prof Quentin Ramasse.

Parts of this thesis have been published by the author and co-workers in:

- Ge, W., Beanland, R., Alexe, M. and Sanchez, A.M. (2023), 3D Reconstruction of Sawtooth 180° Tail-to-Tail Domain Walls in Single Crystal BiFeO3. Adv. Funct. Mater. 2301171. https://doi.org/10.1002/adfm.202301171

- Ge, W., Beanland, R., Alexe, M., Ramasse, Q. and Sanchez, A.M. (2023), 180° head-to-head flat domain walls in single crystal BiFeO3. Microstructures 2023;3:2023026. http://dx.doi.org/10.20517/microstructures.2023.13

Abstract

Ferroelectric materials, characterized by the existence of non volatile polarization vector whose direction can be switched by external field, have formed a large functional applications and raised extended and profound research interests. As the result of achieving a lowest possible energy profile, ferroelectric materials are generally divided into smaller domains with different orientations of the polarization vector, separated by a thin interface known as the domain wall. Domain walls, where the polarization transition happens, take up only a small share of the sample volume and were used to regarded as topological defects. However, they are found to possess a different electrical property unobserved in the bulk domain, which boosted the study and design of domain-wall dedicated devices. The object of this thesis is to build a comprehensive understanding of the complex domain and domain wall structure inside the flux-grown single crystal $BiFeO_3$, examine ferroelectricity at vicinity of the domain wall down to the atomic scale, and study the change of electrical/chemical properties at the domain wall by the help of advanced transmission electron microscopy techniques.

First, domain structure in the flux-grown $BiFeO_3$ single crystals was reconstructed covering a broad range from the bulk size down to atomic scale. A dense array of stripe nanodomains separated by sawtooth and flat domain walls were found to repeat within the crystal. Moreover, both domain walls were found to be 180°-type, a very rare structure which was conventionally believed to have high energy cost. The domain structure indicates the head-to-head flat domain walls were highly negatively charged, while the tail-to-tail sawtooth domain walls were either neutral or positively charged.

Next, local polarization transition was studied at the vicinity of both domain walls by polarization mapping at atomic resoltuion. The neutral sawtooth domain walls are found to be Ising-type, while the charged sawtooth walls show a mixture of Ising/Bloch/Néel behaviour. On the other side, the flat domain walls were found to have a reconstructed atomic structure that is stoichimetricly different from the bulk material, and there is no polar transition at the flat walls.

Finally, local bonding status of the flat domain walls were investigated by high resolution EELS. Reconstructed flat domain walls are revealed to consist of alternating Bi clusters and Fe+O clusters, and have a slightly increase bandgap compared to the bulk. Fine ELNES analysis indicates Fe atoms are under the vary similar octahedra condition to the bulk material.

Abbreviations

ABF Annular Bright Field

ADF Annular Dark Field

BF Bright Field

BFO $BiFeO_3$

BTO $BaTiO_3$

CBED Converged Beam Electron Diffraction

CDW Charged Domain Wall

EELS Electron Energy Loss Spectroscopy

ELNES Electron Energy Loss Near Edge Structure

FIB Focused Ion Beam

HAADF High Angle Annular Dark Field

NDW Neutral Domain Wall

PFM Piezoresponse Force Microscopy

$\mathbf{P_s}$ Spontaneous Polarization

PTO $PbTiO_3$

SAED Selected Area Electron Diffraction

STEM Scanning Transmission Electron Microscopy

STO $SrTiO_3$

$\mathbf{T_C}$ Curie Temperature

TEM Transmission Electron Microscopy

Chapter 1

Introduction

1.1 Introduction

1.1.1 Background

The term 'ferro', which means 'iron' in a literal sense, has been used to describe physics properties (ferromagnetism, ferroelectricity, ferroelasticity, etc.) that possess at least two hysteretically switchable states (magnetization, polarization, strain. etc.), which started from the discovery and wide application of magnetism in metal iron and its minerals.[1; 2] If a material has two or more ferroic orders, it falls into the category of multiferroic materials,[3; 4; 5] where the coexistence and coupling of those orders make it possible for their mutual control, i.e., electrical control of magnetic bits and vice versa, and might induce novel functionalities not present in either state alone, thus promises a wide range of applications in multifunctional devices.[6; 7] For example, compared to the conventional magnetic/electric binary memory, four memory states can be obtained in multiferroic tunnel junctions (MFTJs) given by resistance variation upon switching among different ferroelectric polarization orientations.[8; 9; 10; 11]

Historically, very few multiferroic materials exist in nature or could be synthesized in the lab, and the scarcity was addressed by Spaldin in 2000[3]. The author proposed that in perovskite materials, ferroelectricity emerges because of the hybridization of the electron clouds of neighbouring ions, which supports off-centring polar shift of the ions, so called displacive ferroelectricity, and is particularly energetically favourable when the 3d shell is empty. On the contrary, magnetic ordering requires partially filled 3d shells. This realization triggered an intensive search for materials whose ferroelectricity is driven by other non-displacive mechanisms that are compatible with magnetic order,[7; 12; 13; 14] for example, the lone pair mech-

anism based on the spatial asymmetry created by the anisotropic distribution of unbonded valence electrons around the host ion,[15; 3; 16] and the charge ordering mechanism where valence electrons are distributed non-uniformly around their host ions which might introduce an electric polarization.[17; 18]

Bismuth Ferrite ($BiFeO_3$, BFO) is the most extensively investigated multiferroic material which simultaneously exhibits anti-ferromagnetism and ferroelectricity.[16; 15; 3; 2; 4; 1] SO far, it is still the only room-temperature single phase multiferroic material that possess a large ferroelectric polarization (~ 100 μCcm^{-2}) which originates from the local dipole created by a pair of Bi^{3+} valence electrons in the 6s orbital that is not involved in sp hybridization. Together with its versatile perovskite structure[15; 19; 20] and a broad set of physical properties[21; 22; 16], BFO is considered ideal for the host material of multiferroic devices.[16; 7] While historically the growth of single crystal BFO was found to be rather difficult, and its ceramic specimens were too conductive to be used in any practical devices.[16] Early measurement of bulk ferroelectricity around 1970s in single crystals yielded small values ~ 6 μCcm^{-2},[23] and the authors viewed this small measurement as a lack of saturation and marked that the actual polarization of BFO should be a magnitude higher as expected from a material with such large polar shift ~ 40 pm.[23; 24] As a comparison, another perovskite ferroelectric barium titanate has a polar shift ~ 5 pm and a polarization of ~ 30 μCcm^{-2}.[25; 26; 27; 28; 29] Research interests of BFO were re-ignited by the successful growth of high quality thin films in 2003[15] where a large polarization of ~ 60 μCcm^{-2} was demonstrated for the first time, which was then proposed to originate from a high sensitivity of the polarization to small changes in lattice parameters. Later, large polarization of 90-100 μCcm^{-2} has also been found in ceramics[30] and single crystals,[31; 32; 33; 34; 35] together with first principle calculations[36; 37] they support the statement that polarization of bulk BFO is intrinsically high and relatively insensitive to strain.[37]

High quality BFO single crystals have been successfully grown by flux-growth technique and later studied in detail.[32; 33; 34; 35] Nanoscale domain structures and a local hysteresis loop of the crystal was studied by piezoresponse force microscope,[33; 34] and the polar shift was revealed by atomic resolution imaging[33; 34; 35] to be as large and comparable to thin film samples[15; 38; 19] and other single crystal samples[31] where a large polarization value ~ 100 μCcm^{-2} was found. Yet experimentally, this batch of single crystals failed to demonstrate any indication of bulk ferroelectricity or to show any movement of the domain walls, despite how strong the applied electric field. On the other hand, there has been disagreement among explanations of nanoscale domain structure for this same batch of single

crystals,[33; 34; 35] even though observations reported by different groups share considerable similarity.

1.1.2 Aims and objective

The presence of domains and domain walls in ferroelectric materials is believed to have a profound influence on the their properties,[2; 39] particularly, charged domain walls can possess different electrical properties not observed in bulk material, for example, enhanced conductivity and photovoltaic effects.[40; 41; 21] Yet at the time of writing, there has been less study covering the possible influence of domains and domain walls on the discrepant polarization values. Meanwhile, a large part of the scientific literature on BFO describes investigations of domain structure in thin films, often using mismatch to the substrate to tune strain in the epitaxial layer and the interesting domain structures that result.[15; 21; 38; 42; 43; 44] In comparison, much less research has been performed on the domains in single crystal $BiFeO_3$, where the material has its intrinsic crystal structure and a much richer domain structure, since it is no longer constrained along thickness direction.[45; 46]

Fortunately, advanced electron microscopy techniques are now available which are applied in this thesis to re-investigate the BFO single crystal and help address these fundamental aspects of BFO. This thesis aims to understand the complex three-dimensional structure of domains in single crystal bismuth ferrite using characterization and measurements made from different viewpoints, as well as investigating the local polar transition at charged domain walls, in hope of building the link between microscopic structure and bulk properties of the material, and answering the question if local domain structure would influence the measured spontaneous polarization. Various electron microscopy methods have been employed to investigate the structure at different scales, ranging from conventional diffraction contrast to advanced atomic resolution imaging and electron energy loss spectroscopy. This thesis is organized as follows:

Chapter 1 commences with the introduction of fundamental concepts in ferroelectricity, followed by a general description of perovskite ferroelectrics. Later in this chapter, further details on BFO are described, since this multiferroic is the main material of interest in this thesis. Additionally, the formation of domains and domain walls is covered, as well as a brief summary of the quantitative polarization calculation at atomic scale.

The experimental equipment and methods that empower this study are covered in Chapter 2. It contains the main imaging techniques and mechanisms, and electron microscopy associated techniques. The main procedure for sample growth

is described and the detailed process of the calculation method is also explained.

Chapter 3 focuses on revealing the domain structure in single crystal BFO down to nanometer scale. Previous studies on the same crystals[33; 34; 35] failed to understand the structure due to overlapping of features in transmission images. This problem was overcame here by multiple observations along different directions including an edge-on direction. A 3D model has been proposed based on the observations.[47]

Chapter 4 commences with the procedure used to quantify ferroelectric polarization in the single crystal BFO by atomic resolution scanning transmission electron microscopy (STEM) images. Polar transitions at the charged domain walls, observed using atomic resolution STEM imaging techniques, are analysed in detail.[48]

Finally, in Chapter 5, the electronic and chemical information of the reconstructed domain walls found in the BFO single crystal is investigated. High resolution electron energy loss spectroscopy (EELS), covering both low and high energy losses, has been used to study the elemental distribution as well as potential changes of bonding and bandgap.

1.2 Ferroelectricity

Ferroelectrics are part of a larger class of materials known as ferroics, generally described as having two or more energetically equivalent polar states (Figure 1.1) with an order parameter (e.g. magnetization/strain/electrical polarization) which can be switched by application of an external field (e.g. magnetic/mechanical/electrical).[45; 2; 1] Ferroelectric materials have two or more discrete states of spontaneous polarization ($\boldsymbol{P_s}$), which is non-zero in the absence of an applied external electric field but can be switched by a sufficiently large applied electrical field.[25; 39] A typical hysteresis loop is shown in Figure 1.2. The coercive field (E_c) corresponds to the electric field at the point where $\boldsymbol{P_s}$ changes sign, and the remnant polarization (P_r) is the polarization at zero external field. All ferroelectrics are, at the same time, piezoelectric materials, i.e. a proportional electric charge is produced when mechanical stress applied to them and vice-versa. Most ferroelectrics lose their spontaneous polarisation above a temperature T_C, known as the Curie temperature.

Ferroelectricity was first recognised in Rochelle salt ($NaKC_4H_4O_6{\cdot}4H_2O$) by Valasek in 1920,[49] whose experiments found the existence of a permanent polarization in this crystal and its hysteresis in electrical switching was, in many respects, similar to the ferromagnetic properties of iron. For a period afterwards, it was believed that only certain complex structures, with hydrogen bonds, could exhibit

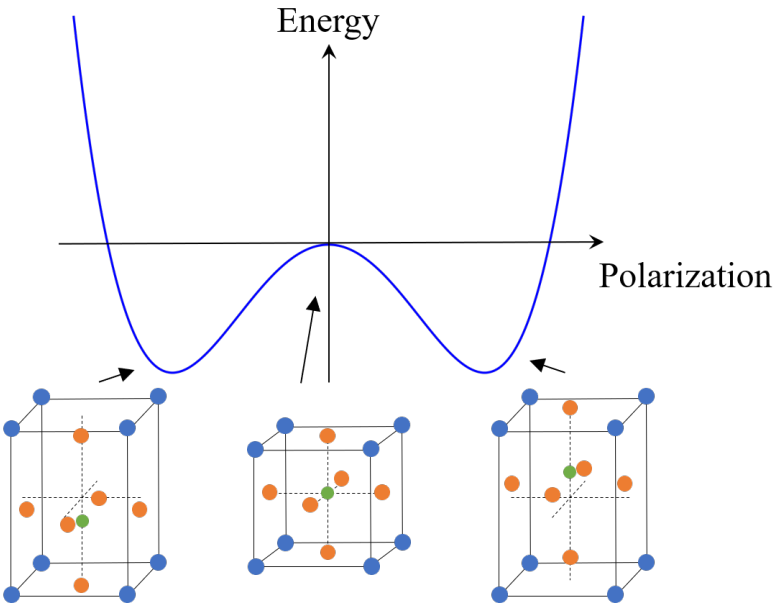

Figure 1.1: Energy of a ferroic material as a function of polarisation. Two different polar states are stable, found at the minima in the curve. The accompanying distortions of the unit cell and sub-unit cell atomic displacements for a tetragonal ferroelectric like $PbTiO_3$ are also shown.

ferroelectricity,[45]. It was around 1945 when ferroelectricity was reported in barium titanate ($BaTiO_3$, BTO),[50; 26] a simple perovskite structure only contains five atoms per unit cell without hydrogen. With the importance of its discovery quickly recognised, BTO became the most extensively investigated ferroelectric material and has also raised intense studies into the perovskite ferroelectric family.[26; 27; 51]

A nonzero ferroelectric polarisation $\boldsymbol{P_s}$ can only be present in a crystal with a non-centrosymmetric point group since it is a bulk vector property. At the same time, to ensure the presence of different polar states and to enhance the possibility of switching between them with external field, the crystal structure needs to be obtained as a small symmetry-breaking distortion of a higher symmetry non-polar state,[45], known as the prototype or aristotype phase. Of all 32 point groups, 21 are non-centrosymmetric, among which 20 are piezoelectric, describing materials that exhibit electrical polarity when subject to stress. Of the 20 piezoelectric crystal classes 10 are ferroelectric/pyroelectric, characterized by the fact that they have a unique polar axis and possess $\boldsymbol{P_s}$ along the polar axis.

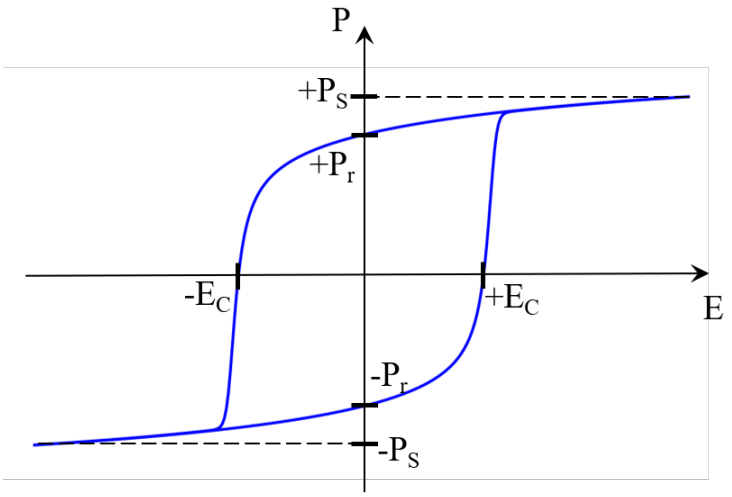

Figure 1.2: A ferroelectric $P - E$ hysteresis loop

1.2.1 Modern theory of ferroelectricity

Ferroelectric polarization in a material cannot be directly measured by electrical means. Instead, it is the charge flowing through an external circuit connecting the electrodes of the ferroelectric capacitor that is measured, usually in the units of μCcm^{-2}, and in this case the movement of charge corresponds to a change in polarization of the ferroelectric.[52] Although this experimentally measured charge flow has been one way, and probably the most critical way, to identify ferroelectrics, it does not build a link between the macroscopic measurement with the internal structure/property or the fundamental physics of the material. Conventionally, the classic Clausius-Mossotti model[53; 54] pictures dielectric solids as an assembly of separate and independently polarized units, and each single unit has its own dipole and when summed up they form the bulk $\boldsymbol{P_s}$. This scheme can be safely applied to ionic or molecular crystals, which represent one extreme case of inter-atomic bonding. At the other extreme are covalent materials, where electronic charge is delocalized and electron cloud distribution is continuous, periodic and cannot be unambiguously partitioned into single units and the dipole of a unit cell is completely ill defined. In real materials the two extreme mechanisms coexist and bulk $\boldsymbol{P_s}$ has contributions from both ionic (P_{ion}) and electronic (P_{el}) part,[55; 56] each given by

$$\boldsymbol{P_{ion}} = \frac{1}{v}\sum(\boldsymbol{r_i} q_i) \tag{1.1}$$

$$\boldsymbol{P_{el}} = \frac{1}{v}\int \boldsymbol{r}\rho(\boldsymbol{r})\, d\boldsymbol{r} \tag{1.2}$$

where $\boldsymbol{r_i}$ and q_i are the positions and charges makes up the ionic dipole, $\rho(\boldsymbol{r})$ is the electronic charge density.

The modern theory of polarization[57; 58; 59] views the polarization $\boldsymbol{P}$ as elusive and non-measurable, and is an intrinsic equilibrium property of the material, while sees the measurable $\Delta\boldsymbol{P}$ as the finite difference between the polar structure and the suitable non-polar prototype structure of the same material, expressed as[55; 56]

$$\Delta\boldsymbol{P} = \int_0^1 \frac{\partial \boldsymbol{P}}{\partial \lambda} d\lambda \tag{1.3}$$

where λ is a continuous variable parameterizes the transformation: $\lambda = 0$ corresponds to the prototype structure (high symmetry) and $\lambda = 1$ corresponds to the ferroelectric structure (low symmetry). From this viewpoint, ΔP can be derived upon making an adiabatic change in the Kohn-Sham Hamiltonian of the solid,[55; 57] and interpreted as a displacement of the center of charge of the Wannier functions, so called Berry phase theory of polarization.[57] Two important conclusions of this theory are: first, polarization of a solid is not a vector but a lattice $\boldsymbol{P_0} + 2e\boldsymbol{R}/\Omega$, where $\boldsymbol{R}$ is a lattice vector in the direction of polarization, and Ω is the volume of the unit cell; second, the linearity of the polarization given in terms of Born effective charges as

$$\Delta\boldsymbol{P} = \frac{e}{\Omega} \sum Z_i^* \boldsymbol{u_i} \tag{1.4}$$

where Z_i is the Born effective charge and $\boldsymbol{u_i}$ is polar shift of element i. This result enables one to directly estimate the $\boldsymbol{P_s}$ in ferroelectrics if the atomic position of each element was given, i.e., by performing atomic resolution STEM/TEM displacement mapping.

1.2.2 Perovskite ferroelectrics

Perovskite oxides are some of the most studied ferroelectric structures.[45; 51; 44] Named after the mineral perovskite $CaTiO_3$, the prototype perovskite structure is simple cubic and has the composition ABO_3, where A and B represent two different cations alongside the oxygen anions. The physical properties of the perovskite family are extremely diverse: they can be metallic or insulating depending on the composition and also exhibit different types of structural and magnetic order.[25]

At high temperature, perovskite oxides have a paraelectric phase where the structure is non-polar ($\lambda = 0$ in Equation 1.3) and, for many, this phase is cubic with a crystal parameter of around 4 Å and $Pm\bar{3}m$ space group. A typical repre-

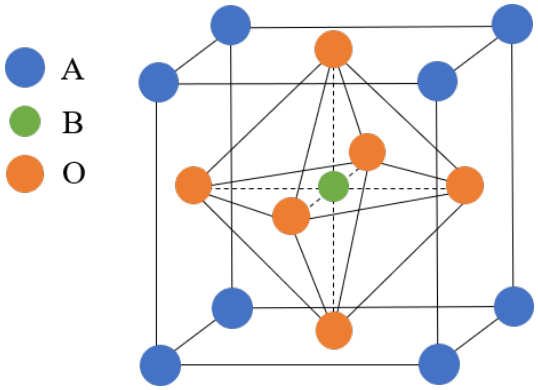

Figure 1.3: Paraelectric cubic perovskite unit cell

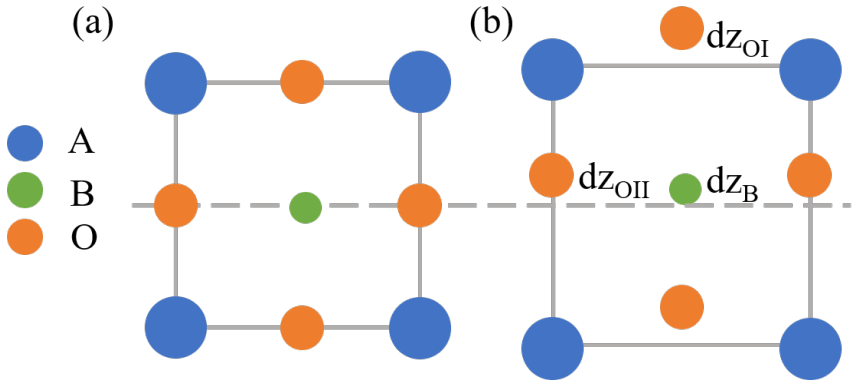

Figure 1.4: Distortion of (a) cubic perovskite unit cell to (b) tetragonal unit cell, as the case of BTO and PTO. From the perspective of B cation, among the 6 oxygen atoms forming the octahedra, the 2 along the polar direction are generally classified as OI, and the 4 perpendicular (nearly) in the same plane as B cation are OII.

sentation corresponding to an unit cell of this structure is shown in Figure 1.3. It corresponds to a cubic unit cell with B cations placed in the center, oxygens centered on the cube faces and A cations on the cube vertices. The six oxygens form an oxygen octahedron with the B cation in its center (6 oxygen first neighbours) and A cation in its facet center (12 oxygen first neighbours), and shares corner vertices with six neighbouring octahedra. When cooled down to below T_C, the symmetry is lowered from cubic to its ferroelectric phase ($\lambda = 1$ in Equation 1.3), together with a change in bond distances, cation and anion positions (Figure 1.4), and/or rotation/distortion of oxygen octahedron. The anions and cations and, most importantly, the local displacements and distortions in the crystal form the basis of ferroelectricity in such materials.

The deviation from an ideal perovskite structure can be measured through

a tolerance factor t[60]

$$t = \frac{r_A + r_O}{\sqrt{2}(r_B + r_O)} \tag{1.5}$$

where r_A, r_B and r_O are the radii of A, B and O ions, respectively. When $t > 1$, the structure is fixed by the A–O distance and the B atom is too small for the oxygen octahedron so that the structure will develop a small polar distortion, as in BTO. Conversely, when $t < 1$, the A atom is small in comparison to the space between the oxygen octahedra, so the A atom cannot effectively bond with all 12 neighboring O atoms. If t is only slightly less than one, rotations and tilting of the oxygen octahedra will be favored (as in BFO); for smaller t the compound will favor a strongly distorted structure with only 6 neighbors for the A atom as in $LiNbO_3$.

BTO was the first perovskite oxide compound identified as being ferroelectric. It has a paraelectric cubic phase($Pm\bar{3}m$) above T_C = 393 K, below which it undergoes successive transformations to tetragonal($P4mm$), orthorhombic($Amm2$, below 278 K) and rhombohedral phase($R3m$, below 183 K). In the three ferroelectric phases, its polar axis lies on [001], [011] and [111], respectively, and the measured polarization is 27 μCcm^{-2}, 36 μCcm^{-2} and 33 μCcm^{-2}, respectively.[25; 26; 27] Hybridization between B-site Ti and O is essential to weaken the short-range repulsion and allow the ferroelectric transition.[61]

Another important perovskite ferroelectric is lead titanate ($PbTiO_3$, PTO) which maintains its ferroelectric $P4mm$ tetragonal phase under 763 K, above which it possesses paraelectric cubic structure. Its $\boldsymbol{P_s}$ lies along [001], i.e. the c-axis, with a value about 60-70 μCcm^{-2} at room temperature.[62; 29; 25] In this phase the lattice parameters are a = 3.904 Å and c = 4.152 Å, corresponding to a c/a ratio 1.063 and unit cell volume 63.28 Å^3. Similar to BTO, hybridization between the B-site Ti and O is essential to weaken the short-range repulsion and allow the ferroelectric transition; but in PTO, Pb and O states hybridize, leading to a large strain that stabilizes the tetragonal phase, whereas in BTO the interaction between Ba and O is completely ionic.[61] When Pb atom selected as the origin of PTO unit cell, one will have Ti at (½, ½, ½), OI at (½, ½, 0) and OII at (½, 0, ½) and (0, ½, ½) in the cubic paraelectric unit cell, and those atoms move to Ti at (½, ½, ½+Δz_{Ti}), OI at (½, ½, 0+Δz_{OI}) and OII at (½, 0, ½+Δz_{OII}) and (0, ½, ½+Δz_{OII}) for tetragonal phase, where $\Delta z_{Ti} = 0.040$, $\Delta z_{OI} = \Delta z_{OII} = 0.112$ with a value of Δz_{Ti} = 17 pm, $\Delta z_{OI} = \Delta z_{OII}$ = 47 pm.[29] In contrast to BTO, all O atoms in the PTO unit cell move in the same direction as the Ti atom, but a larger distance.

1.2.3 Octahedral tilting

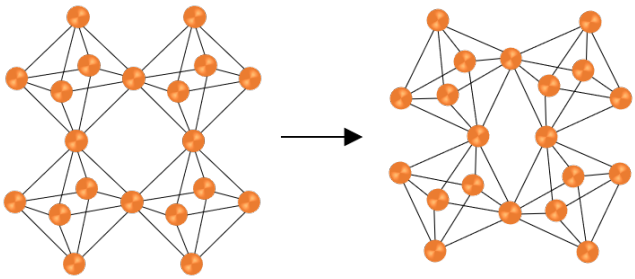

Figure 1.5: Octahedral tilting. Perpendicular to the tilt axis, neighbouring octahedra are constrained to tilt oppositely.

The octahedron formed by the six oxygen atoms in a perovskite unit cell could be seen as a rigid body but in fact their connection with neighbouring octahedra can change easily. When an octahedron is tilted in some particular way it causes tilting of neighbouring octahedra. If we focus on a single layer of lateral-connected octahedra and its in-plane tilting (part of this layer is shown in Figure 1.5), it is easy to understand that neighbouring octahedron have to tilt oppositely to the central one. When multiple layers are stacked horizontally, along the stacking direction neighbouring octahedron have the freedom to tilt either the same sense as the central one, described as 'in-phase', or tilt in the opposite sense as 'antiphase'. An effective notation of tilted octahedra in perovskites was developed by Glazer[63] to describe the tilting about the pseudocubic axes, in the order [100], [010], [001], of the perovskite unit cell, under the following rules: first, a letter is assigned to describe the tilting magnitude/angle about each axis, for example *abc* means unequal tilts about the three axes and *aac* means equal tilts about [100] and [010] with a different tilt about [001]; second, each letter is followed by a superscript +/-/0 to describe the in-phase/antiphase/no-tilting of neighbouring octahedra along a particular axis, for example $a^+b^-c^0$ describes a system with in-phase tilting about [100] axis, antiphase tilting about [010] axis with a different magnitude, and no tilts about [001] axis. In total there are 23 possible tilt systems under Glazer's notation.

A consequence following the octahedral tilting is the rise of ½(ooo) reflections (where 'o' indicates an index with an odd number) in electron diffraction patterns (Figure 1.6).[64; 65] Thus, in the case of $a^-a^-a^-$ tilting system, the oxygen octahedra tilt about the [111] axis and only 6 of the twelve ⟨110⟩ variants contain superstructure reflections and the other six do not. To be specific, it is those which are perpendicular to the [111] tilting axis, such as [$\bar{1}$10] in Figure 1.6(b), that do not have superstructure reflections. As diffraction patterns represent the atomic ar-

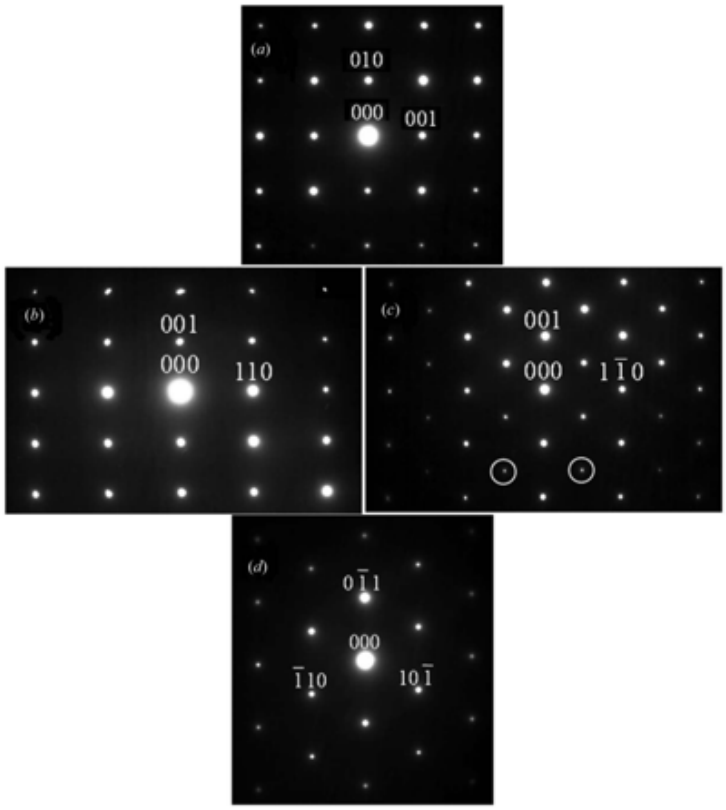

Figure 1.6: Electron diffraction patterns obtained from a sample of BFO from (a) [100], (b)[$\bar{1}$10], (c) [110] and (d) [111] view-direction. Superlattice reflections arising from antiphase tilting are ringed. Reproduced with permission of the International Union of Crystallography.[64]

rangement in reciprocal space, those two $\langle 110 \rangle$ groups of the $a^-a^-a^-$ tilting system have different atomic projections. The antiphase tilting is presented in the (110) projection (Figure 4.6) but is absent in the ($\bar{1}$10) projection (Figure 4.2).

1.2.4 Bismuth Ferrite

The idea that a material can be simultaneously ferromagnetic (symmetry breaking of time) and ferroelectric (symmetry breaking of space) is fascinating: thinking of a device whose magnetic order can be manipulated/read by electrical signal and vice versa, which naturally have higher efficiency and storage intensity than the current devices based on only one order. The term 'multiferroic' has been used to describe this class of materials that, to be inclusive, simultaneously possess more than one ferroic properties.[6] Historically, finding a multiferroic material that makes practical microelectronic applications has not been easy. Nicola Spaldin has asked

the question 'Why there are so few magnetic ferroelectrics?'[3] and in her discussion about perovskite oxides, she observed that ferroelectrics have B-site ions with d^0 electrons, whereas magnetics require partially filled d^j ($j > 0$) electrons. In the case of BFO, its ferroelectric $\boldsymbol{P_s}$ is mostly caused by the lone pair s^2 of A-site Bi^{3+} ions, while its magnetization comes from the B-site Fe^{3+} ions. This idea triggered the search for perovskites with possible A-site ferroelectricity and B-site magnetism, such as $Bi(Cr,Fe)O_3$ and $BiMnO_3$, and those theoretically predicted ones await experimental verification.

BFO is arguably the most investigated multiferroic material to date, yet it had not always been like this. For a period, its study was hindered by the difficulty to grow high quality single crystals while the ceramics were too highly conductive.[23] Research interest on BFO was reignited by the success of growing high quality BFO thin films with an unexpectedly large spontaneous polarization, about 100 μCcm^{-2},[15] an order of magnitude larger than measurements of the bulk value at the time,[23] together with large ferromagnetism of ca. 1.0 Bohr magneton (μ_B) per unit cell. At that time, it was proposed that the structural distortion of BFO unit cells, from rhombohedral to tetragonal(-like) due to the epitaxial mismatch with the substrate, played the crucial role in generating large $\boldsymbol{P_s}$. This was later proved not to be the case, since good quality single crystals[31; 33] or ceramics[30] were found to have a similar $\boldsymbol{P_s}$ value.

The phase diagram of the Bi_2O_3/Fe_2O_3 system is shown in Figure 1.7. The instability of BFO at elevated temperatures was recognised by the slow decomposition at $T > 700$ °C, well below its peritectic decomposition, into phases like Bi_2O_3, Fe_2O_3, $Bi_2Fe_4O_9$ and $Bi_{25}FeO_{39}$. The α phase of BFO is rhombohedral, and at about 825 °C it has a first-order phase transition into a high temperature β phase. Although the exact symmetry of the β phase is debatable, it is widely agreed to be centrosymmetric.[67; 68; 69] Above $\sim$ 925 °C, there is a $\beta - \gamma$ transition into a cubic $Pm\bar{3}m$ phase, which is quite unstable since it is close to the deposition temperature $\sim$ 933 °C and rapidly decomposes into parasitic phases like $Bi_2Fe_4O_9$ or Fe_2O_3. As a result, secondary phases like Bi-rich $Bi_{25}FeO_{39}$ and Bi-poor $Bi_2Fe_4O_9$ readily form during a crystal growth to accommodate deviations from perfect stoichiometry, e.g. due to the relative volatility of Bi_2O_3.[70; 34]

BFO maintains rhombohedral structure (space group $R3c$) below its Curie temperature $T_C = 1100$ K.[24; 16] It has a pseudocubic lattice parameter of 3.965 Å and rhombohedral angle 89.4° (See Figure 1.8. It is called 'pseudocubic' because the structure is close to the cubic perovskite shown in Figure 1.3).[24] A switch between different indexing systems can be found in Table 1.1, while pseudocubic indexing is

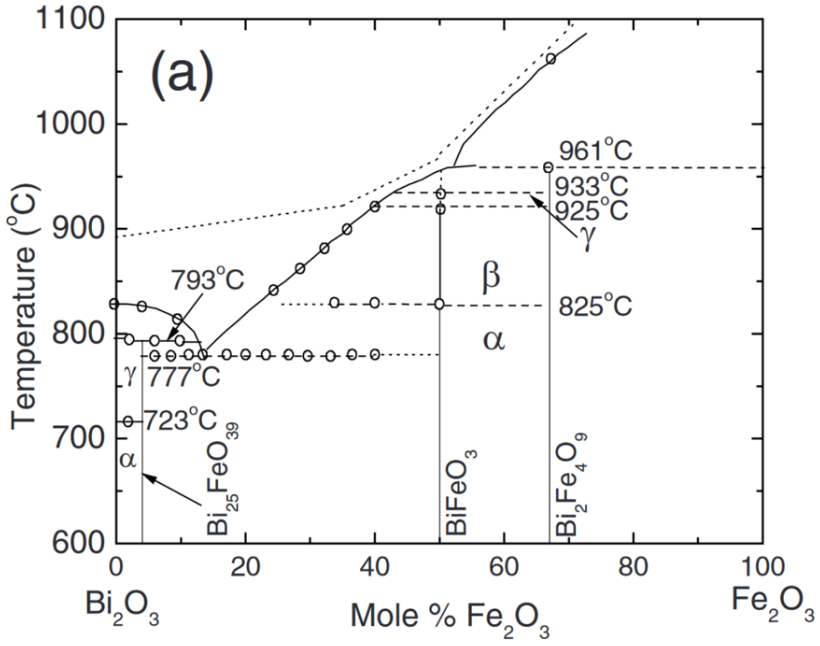

Figure 1.7: Phase diagram of the Bi_2O_3/Fe_2O_3 system. Reprinted figure with permission from [66]. Copyright 2023 by the American Physical Society.

used throughout this thesis.

Pseudocubic	Rhombohedral	Hexagonal
1, 0, 0	1, 1, -1	2, 4, 1
1, 1, 0	0, 1, 0	2, 1, 1
-1, 1, 0	1, 0, -1	0, 1, 0
1, 1, 1	1, 1, 1	0, 0, 1

Table 1.1: Index switch between pseudocubic, rhombohedral and hexagonal unit cell.

The tolerance factor of BFO is $t = 0.88$, i.e. less than one, so the octahedra must buckle in order to fit into a cell that is too small. As a result, oxygen octahedra in each neighbouring unit cell are tilted in an antiphase fashion around the [111] polar axis by 11°-14° ($a^-a^-a^-$ in Glazer's notation).[24; 72; 73] Along the [111] polar axis, Fe ions are shifted by about 13.4 pm away from the center of their containing octahedra, and Bi ions are shifted about 54.0 pm along the same direction.[24] A relative shift of Fe to Bi of $\sim$ 40.6 pm can be yielded along [111] direction, and this shift is often referred as the $\boldsymbol{\delta}_{FB}$ vector (Figure 1.9) whose direction is antiparallel to $\boldsymbol{P_s}$.[24; 38] Projection of the BFO unit cell and the $\boldsymbol{\delta}_{FB}$ vector from various viewpoints are shown in Figure 1.9.

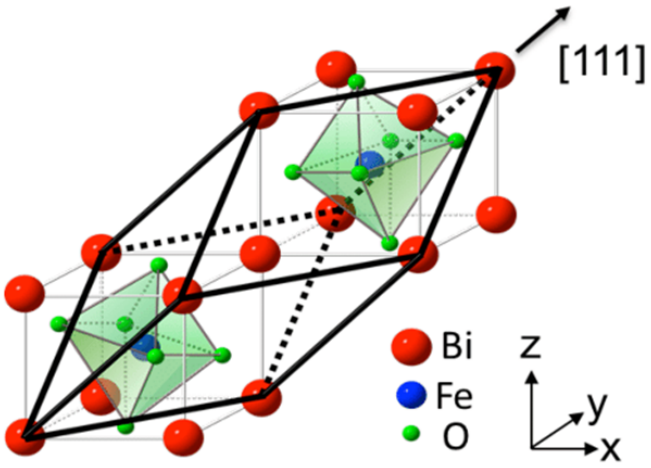

Figure 1.8: Pseudocubic transformation in BFO. The two corner-linked cubes are two pseudocubic unit cells, and the thick dark lines form a rhombohedral unit cell.[71]

BFO has *G*-type anti-ferromagnetic short-range magnetic ordering below the Néel temperature $T_N = 370$ °C, that is each Fe^{3+} spin is surrounded by six antiparallel spins on the nearest Fe neighbors.[31] The spins are in fact not perfectly antiparallel, as there is a weak canting moment caused by the local magnetoelectric coupling to the polarization. Superimposed on this canting is also a long-range superstructure consisting of an incommensurate spin cycloid of the anti-ferromagnetically ordered sublattices (Figure 1.10. The cycloid has a very long repeat distance of 62-64 nm, and a propagation vector along the [110] direction.[74]

The optical bandgap of BFO at room temperature has been reported ranging from 2.3 to 2.8 eV.[75; 76; 77] A clear bandgap lowering at charged domain walls has been reported both by experimental observation[78] and theoretical calculation[79], possibly leading to locally enhanced conductivity,[41; 78; 40] while accumulation of oxygen vacancy could also play a role.

1.3 Domains and domain walls

1.3.1 Formation of domains

The formation of domains, and domain walls, in ferroelectric materials along with their size and shape, is the result of a finite size effect together with boundary conditions.[39] In an infinite ferroic sample, a single-domain state (Figure 1.11(a)) will be most favoured because it has minimum interaction energy.[80; 81] However, in

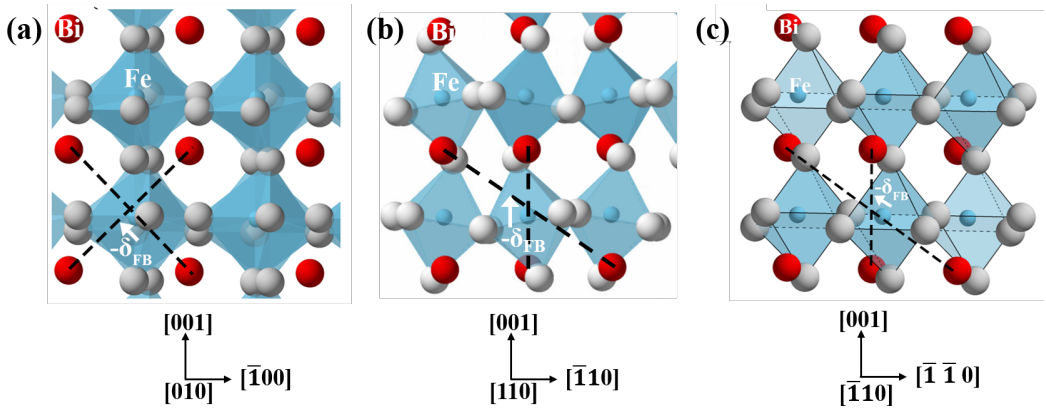

Figure 1.9: Ideal projection of BFO from (a) [010], (b) [110] and (c) [$\bar{1}$10] view-direction. The polar shift vector $-\boldsymbol{\delta}_{FB}$ is labelled on each image, which is parallel to $\boldsymbol{P_s}$.

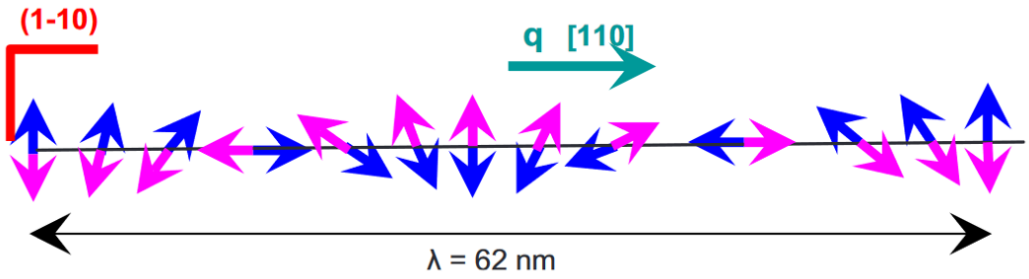

Figure 1.10: Schematic anti-ferromagnetic structure of BFO where the two anti-ferromagnetic sublattices are organized along a cycloidal spiral. The propagation vector $\boldsymbol{q}$ is along [110] and the plane of spin-rotation is (1$\bar{1}$0). Reprinted figure with permission from [74]. Copyright 2023 by the American Physical Society.

a finite ferroic, taken here as ferroelectric material, surfaces perpendicular to the $\boldsymbol{P_s}$ direction have a charge density equal to the dipole moment per unit volume. This charge generates an electric field with opposite sign to $\boldsymbol{P_s}$ and a magnitude of $E = P/\epsilon$ (ϵ = dielectric constant), typically an order of magnitude larger than the coercive field.[39] So, if nothing compensates for the surface charge, the depolarization field will cancel the ferroelectricity. Mobile charges, such as those from electrodes, can partly do the job, while a material can reduce this field by dividing the single-polar state into smaller domains with alternating polarity (Figure 1.11(b)), or a closure domain configuration (Figure 1.11(c)), so that the average polarization is zero. Domain formation can thus be regarded as a finite size effect, driven by the need to minimize surface energy and thus the system's total energy.

Domain size is determined by the competition between the energy required

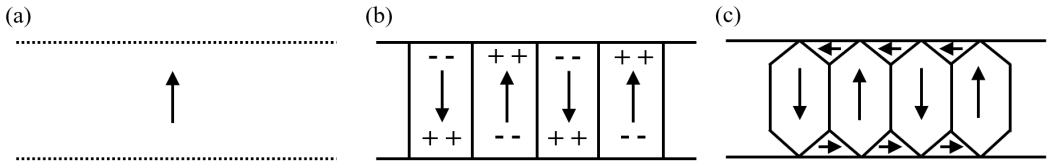

Figure 1.11: (a) In an infinite crystal, a single domain with uniform $\boldsymbol{P_s}$ alignment would be mostly favoured. (b) Conventional stripe domain configuration. (c) Closure domain configuration. Inspired by Ref.[81]

to create the domains. The domain size follows Kittel's law,[81] with the square root of the domain size proportional to the thickness of the material [80; 81]

$$w = \sqrt{\frac{\sigma}{U}d} \tag{1.6}$$

where w is the domain width, σ is the energy density per unit area of the wall, U is the volume energy density of the domain, and d is the sample thickness. More recently, Scott[82] observed that for each given material one could rewrite the square root dependence as

$$\frac{w^2}{\delta d} = G \tag{1.7}$$

where G is an adimensional parameter and δ is domain wall thickness. This equation is also useful in that it can be used in reverse to estimate the domain wall thickness of any ferroic with well-defined boundary conditions,[83] and is independent of the type of ferroic and allows comparisons between different material classes (Figure 1.12).

A good example of how the domain structure is modulated by surface/interface condition is the ferroelectric superlattice structure. Yadav et al.[84] reported the presence of long-range ordered vortex–antivortex (clockwise-anticlockwise) arrays that exhibit nearly continuous polarization rotation in superlattices of alternating PTO (ferroelectric) and STO (insulator) layers, as the result of the competition between charge, orbital and lattice degrees of freedom. Their phase-field modelling confirms that the vortex array is the low-energy state for a range of superlattice periods. Within this range, the large gradient energy from the vortex structure is counterbalanced by the corresponding large reduction in overall electrostatic energy (which would otherwise arise from polar discontinuities at the PTO/STO interfaces since the latter is a centrosymmetric and non-ferroelectric material) and the elastic energy associated with epitaxial constraints (tensile strain from the $DyScO_3$ substrate) and domain formation. All told, in this system, these three energies combine to create a new topology of polarization, that is the system localizes the

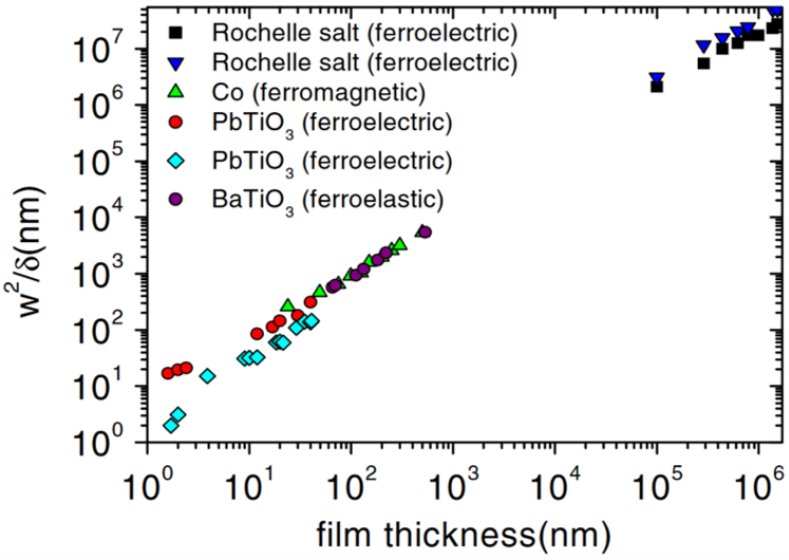

Figure 1.12: Universality of Kittel's law on different ferroelectrics. Reprinted figure with permission from [39]. Copyright 2023 by the American Physical Society.

in-plane $P_{[100]/[010]}$ components at the PTO/STO interfaces and forms alternating out-of-plane $P_{[001]}$ components mid-layer- thereby creating a rotating polarization. Later, Rusu et al.[85] examined a domain structure in a single PTO epitaxial layer sandwiched between $SrRuO_3$ (SRO) electrodes. They observed periodic clockwise and anticlockwise ferroelectric vortices that are modulated by a second ordering along their toroidal core. Whilst, in principle, SRO should provide better screening than STO and reduce the depolarization field at the interface, the authors' models show that it is still unable to screen the large bound surface charges of the ferroelectric layer. The resulting topology, triggered by the electric analogue of the Dzyaloshinskii-Moriya interaction (DMi), is a labyrinth-like pattern with two orthogonal periodic modulations that form an incommensurate polar crystal that provides a ferroelectric analogue to the recently discovered incommensurate spin crystals in ferromagnetic materials.[86; 87]

A final mark of the bulk property of domains is their optical birefringence.[45] All polar crystals are optically anisotropic, meaning the refractive index for light polarized along the polar axis is different from the refractive index for light polarized perpendicular to the polar axis. Between crossed polarizers, domains polarized in the view direction appear dark for all rotations about the polar axis, while domains polarized in any other direction are birefringent and appear bright provided the polar axis of the crystal and the polarizer axes are not co-planar. This technique is particularly useful because of its simplicity, however it cannot generally be used

for the observation of antiparallel domains since the optical index is invariant under domain reversal.[45]

1.3.2 Domain wall types

Domain walls are the boundaries that separate neighbouring domains. Ferroelectric domain walls are typically a thin interface where $\boldsymbol{P_s}$ changes direction and/or amplitude from one domain into another.[39; 88] The fact that domain walls often hold different properties compared to the bulk material attracts intense research interest.[89; 41; 21; 39]

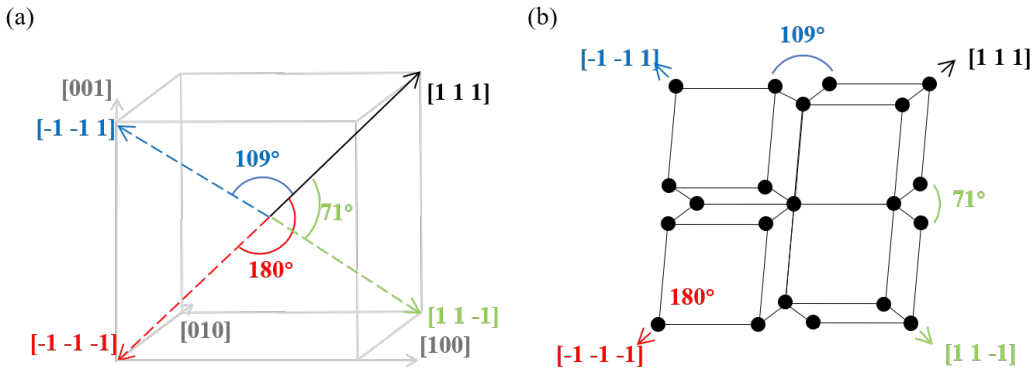

Figure 1.13: (a) Ferroelectric 180° wall and two ferroelastic 71°/109° walls in BFO. (b) The atomic arrangement shows how an elastic component is absent/present in the three cases.

When classifying domain walls, there are three factors to be considered: the angle between polarization in neighbouring domains, the amount of $\boldsymbol{P_s}$ discontinuity at the wall, and the chirality of the $\boldsymbol{P_s}$ transition. The angle aspect simply considers the different directions of $\boldsymbol{P_s}$ in neighbouring domains, which is often linked to the crystallography of the material. A typical example is the 90° change in c/a domains or 180° in antiparallel domains for tetragonal ferroelectrics.[90] Rhombohedral BFO has a [111] polar axis and there are three possible domain walls, one ferroelectric 180° wall and two ferroelectric-ferroelastic walls of 71° / 109° type (Figure 1.13).

For two adjacent domains 1 and 2 with polarization $\boldsymbol{P}_1$ and $\boldsymbol{P}_2$, a bound charge with surface density σ_p is present at the wall separating them given by[89]

$$\sigma_p = (\boldsymbol{P}_2 - \boldsymbol{P}_1) \cdot \boldsymbol{n}_1, \tag{1.8}$$

where $(\boldsymbol{P}_2 - \boldsymbol{P}_1)$ is the $\boldsymbol{P_s}$ discontinuity and $\boldsymbol{n}_1$ is the wall normal vector pointing to domain 1. Domain walls with zero $\boldsymbol{P_s}$ discontinuity, i.e. $\sigma_p = 0$, are called neutral

domain walls (NDW, Figure 1.14(a)). On the other hand, domain walls with non-zero bound charge σ_p are called charged domain walls (CDW, Figure 1.14(b) and (c)). And depending on the angle difference, although there is no strict standard, there are weakly charged (Figure 1.14(b)) or strongly charged (Figure 1.14(c)) domain walls. The head-to-head (tail-to-tail) configuration leads to positive (negative) bound charge at the wall. The presence of bound charge needs to be screened by free charges, i.e. electrons, holes, and/or mobile ions such as oxygen vacancies. Those compensating charges may lead to unusual properties at the interface, for example, enhanced conductivity[41] or photovoltaic properties[21] at charged domain walls.

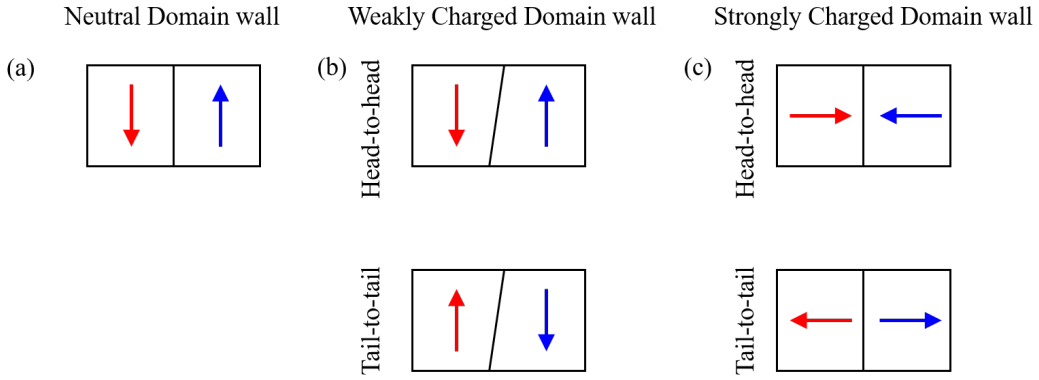

Figure 1.14: Different types of charged domain walls: (a) neutral domain walls, (b) weakly charged domain walls, and (c) strongly charged domain walls. Inspired by Ref.[91]

The transition of ferromagnetic or ferroelectric vectors at the domain wall may demonstrate chiral properties (Figure 1.15).[92; 39; 48] In a 180° domain wall, for example, a non-chiral transition is obtained if the polar vector changes its amplitude from positive maximum to negative maximum without any rotation of its direction (Ising-type, Figure 1.15(a)). Conversely, if the polar vector can either rotate in a plane parallel to the domain wall (Bloch-type, Figure 1.15(b)) or normal to the domain wall (Néel-type, Figure 1.15(c)). A 180° magnetic wall is typically Bloch or Néel-type, as its spin and magnitude is quantized.[39] On the other hand, ferroelectric polarization is not quantized and domain walls are conventionally believed to be Ising-like, because the rotation of polarization vector brings a significant electrostatic and elastic cost.[39; 93] Nevertheless, Houchmandzadeh et al.[94] has shown that whenever there are two order parameters involved (as in any multiferroic system), the coupling between them can induce chirality at the domain walls. Domain walls in BFO are also multiferroic, and in a big way, ferroelectricity, ferroelasticity, anti-ferromagnetism, and anti-ferrodistortive octahedral rotations all

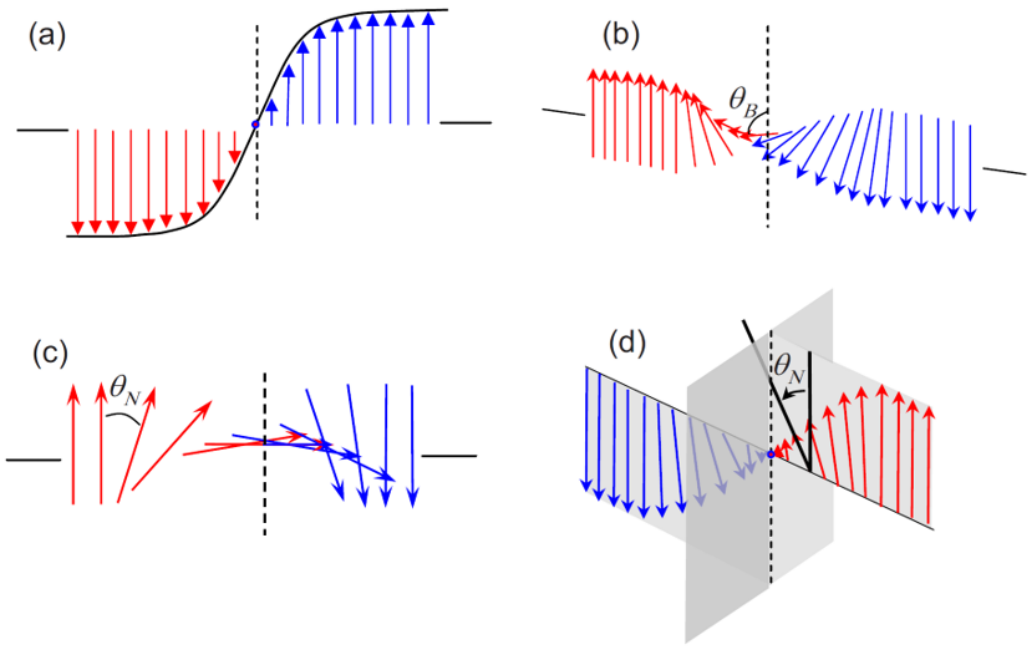

Figure 1.15: Different types of domain walls: (a) Ising type, (b) Bloch type, (c) Néel type, and (d) Mixed Ising-Néel type walls. Reprinted figure with permission from [92]. Copyright 2023 by the American Physical Society.

occur in this material. It is therefore not surprising that the domain walls of this material are found to be chiral.[41; 95]

1.4 Summary

In this chapter, basic physics of ferroelectricity and domains have been covered which helps understand the fundamental knowledge of the material side of this work. Ferroelectricity has been conventionally represented by the indirect measurement of electrical current flowing through the material during a polar switch, while the modern theory of ferroelectricity has build a link between the bulk property and the microscopic structure of the material, thus enabling the direct calculation of polarization if the atomic positions were available, which will be achieved by the advanced electron microscopy methods introduced in the next chapter. Although the shape of domains and domain walls could be complicated and seemingly random, as shown in the result chapters, their formation is the result of energy competition inside the material to help attain a lowest possible energy profile, and several key factors listed in this chapter, such as domain size and domain wall types, would be helpful for their understanding and investigation.

Chapter 2

Methodology

2.1 Introduction

The experimental studies of novel domain structure in ferroelectrics requires advanced microscopy techniques that are capable of providing accurate structural and electronic information of the material. This chapter contains the basic working principles of the microscopy techniques used in this thesis that backs up the investigations. Specifically, structural and electronic investigations at atomic scale are performed using aberration corrected scanning transmission electron microscopy and monochromated electron energy loss spectroscopy, with the support of conventional transmission electron microscopy and its diffraction modes such as selected area electron diffraction and diffraction-contrast imaging. High resolution imaging of the surface domain structure are performed using piezoresponse force microscopy. At the same time, material growth and specimen preparation are covered, since they play a crucial role in determining what will be presented under a microscope. Finally, detailed explanation of polarization calculation based on atomic resolution images is presented.

2.2 Transmission Electron Microscopy

2.2.1 Conventional TEM

In conventional TEM, an incident parallel electron beam illuminates the sample, transmitting through and being projected onto a fluorescent screen or a charged-coupled device (CCD) detector.[97] During the process multiple lenses, before and after the sample, are employed to produce increased magnification of the object. TEM image contrast arises because of the scattering of the incident beam by the

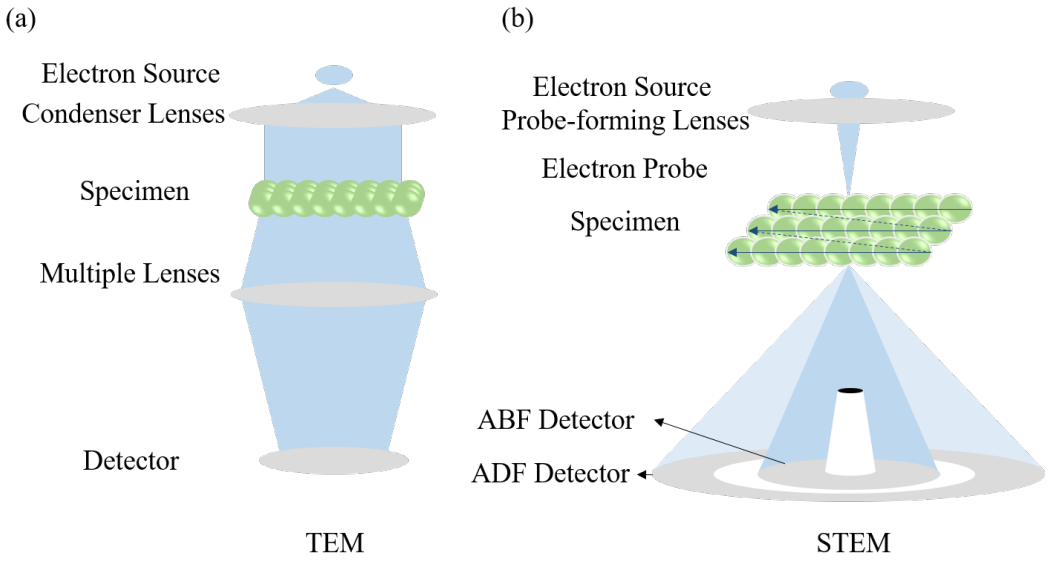

Figure 2.1: Scheme of (a) conventional TEM mode and (b) STEM mode. The STEM collector semiangle used in this thesis is $75-280$ mrad for ADF and $11.5-24$ mrad for ABF, while the incident probe has a convergence semiangle ≤ 30 mrad.

specimen, and the change of amplitude and phase of the electron beam both contribute to the final image by forming amplitude contrast and phase contrast, although most of the time one type tends to dominate. There are two principal types of amplitude contrast, namely mass-thickness contrast- which results from variations in mass and/or thickness since heavier/thicker specimen scatters more electrons off axis- and diffraction contrast, where coherent elastic scattering is strongly excited when Bragg condition is satisfied.[97] Contrast in TEM images can also arise due to the phase alteration of the electron waves scattered through a thin specimen. For the specimens studied in this thesis, imaging areas are usually very close to the thinnest amorphous area, so a useful description of the image formation in a microscope is the weak phase object approximation where the specimen only alters the phase of the electron wave.[98; 99] In this case, with an incident plane electron wave ψ_{in} the interaction with the specimen changes only the phase of the wave, i.e.

$$\psi_{exit}(\boldsymbol{r}) = 1 - i\phi(\boldsymbol{r}) \tag{2.1}$$

where $\phi(\boldsymbol{r})$ is the object function, which represents the phase shifts induced by the specimen. This exiting wave at the back focal plane (diffraction plane) is described by its Fourier transform

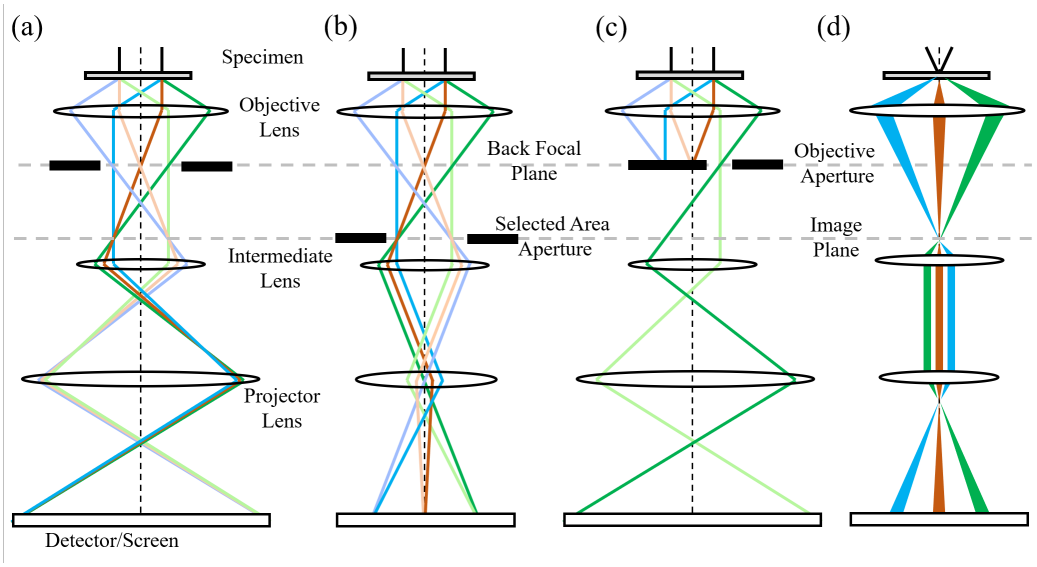

Figure 2.2: (a) TEM imaging. (b) Electron diffraction. (c) Diffraction contrast imaging. (d) CBED

$$\psi_{exit}(\boldsymbol{q}) = \texttt{FT}[\psi_{exit}(\boldsymbol{r})] \tag{2.2}$$

where $\boldsymbol{q}$ is a reciprocal space vector and taking the modulus squared of the amplitude $\psi_{exit}(\boldsymbol{q})$ gives the intensity in the diffraction pattern. The effect of the post specimen lenses and apertures is described by a transfer function, $t(\boldsymbol{r})$, such that the wave function at the image plane is given by the convolution,

$$\psi(\boldsymbol{r}) = \psi_{exit}(\boldsymbol{r}) \otimes t(\boldsymbol{r}) \tag{2.3}$$

and the actual intensity measured by a detector is

$$I(\boldsymbol{r}) \propto |\psi(\boldsymbol{r})|^2 \tag{2.4}$$

The transfer function usually consists of two parts, an objective aperture and the lens system. The objective aperture, t_a, is often modelled as a simple top-hat function

$$t_a = \begin{cases} 1, & \texttt{if } |\boldsymbol{q}| < |\boldsymbol{q}_a|, \\ 0, & \texttt{otherwise} \end{cases} \tag{2.5}$$

where $|\boldsymbol{q}_a|$ is the radius of the aperture. Lens transmission, t_l, is expressed as

$$t_l(\boldsymbol{q}) = \texttt{exp}[-\frac{2\pi i}{\lambda}\chi(\boldsymbol{q})] \tag{2.6}$$

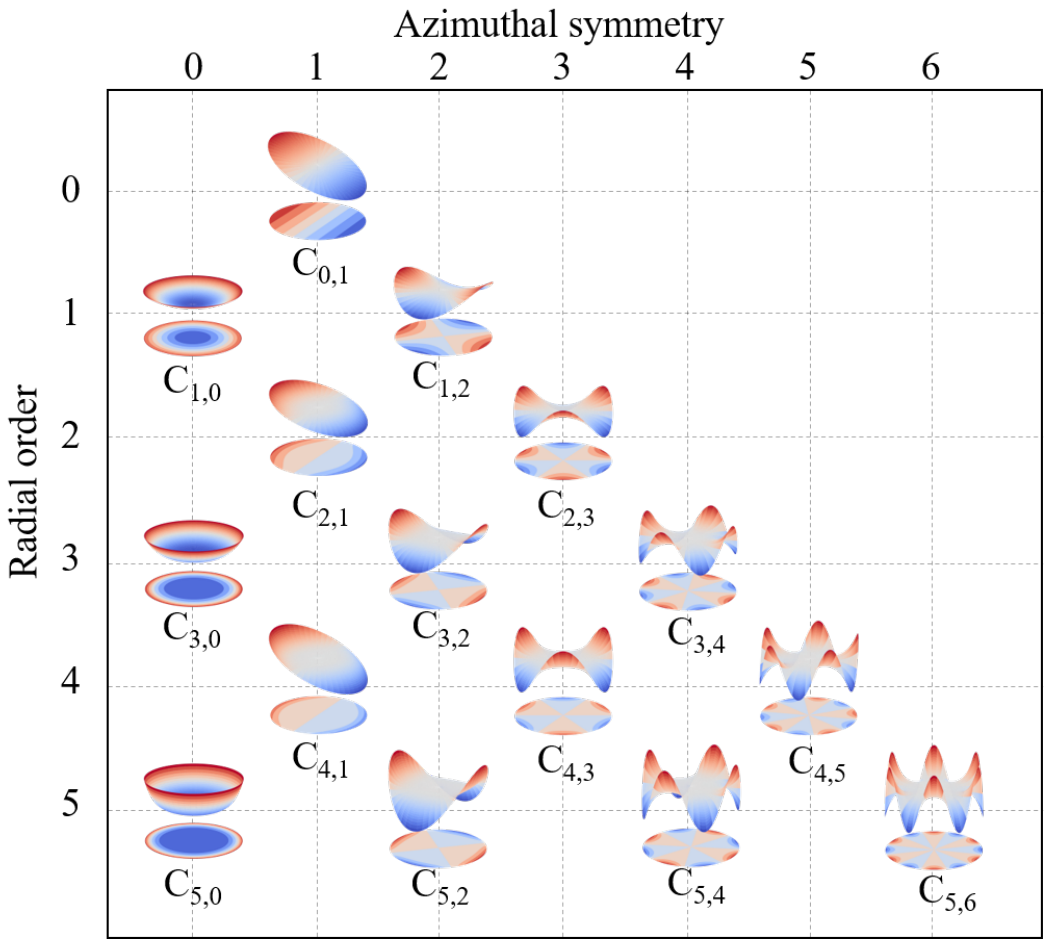

Figure 2.3: Three-dimensional graphic glossary of the aberration coefficients, along with their projection on a plane. Inspired by Figure 4.3 of Ref.[96]

where $\chi(q)$ is the aberration function caused by imperfect lenses that obstructs the achievable resolution of the microscope, which can be described by the expansion

$$\begin{aligned}\chi(\omega) = \texttt{Real}[&\frac{1}{2}C_{1,0}\omega^{*}\omega + \frac{1}{2}C_{1,2}\omega^{*2}+\\ &\frac{1}{3}C_{2,1}\omega^{*2}\omega + \frac{1}{3}C_{2,3}\omega^{*3}+\\ &\frac{1}{4}C_{3,0}\omega^{*2}\omega^{2} + \frac{1}{4}C_{3,2}\omega^{*3}\omega + \frac{1}{4}C_{3,4}\omega^{*4}+\\ &\frac{1}{5}C_{4,1}\omega^{*3}\omega^{2} + \frac{1}{5}C_{4,4}\omega^{*4}\omega + \frac{1}{5}C_{4,5}\omega^{*5}+\\ &\frac{1}{6}C_{5,0}\omega^{*3}\omega^{3} + \frac{1}{6}C_{5,2}\omega^{*4}\omega^{2} + \frac{1}{6}C_{5,4}\omega^{*5}\omega + \frac{1}{6}C_{5,6}\omega^{*6} + ...]\end{aligned} \tag{2.7}$$

where ω is the complex angle $\lambda(\boldsymbol{q_x} + i\boldsymbol{q_y})$ and ω^* and its conjugate, $C_{N,S}$ are the aberration coefficients where N is the radial order and S is the azimuthal symmetry (Figure 2.3). Some of the coefficients can be recognised as $C_{2,1}$ is coma and $C_{3,0}$ is the spherical aberration which plays a central role in electron microscopy.[96] A practical method to remove spherical aberration is to break the rotational symmetry of the optical system by aberration corrector, which uses multipole lenses that produces magnetic field lines perpendicular to the electron beam, achieving the desired deflection of the incident beam.[96; 98]

2.2.2 Electron diffraction

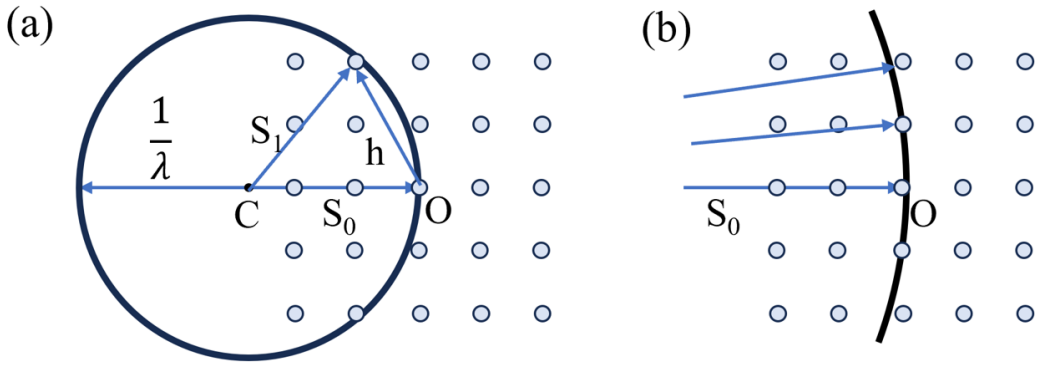

Figure 2.4: Ewald sphere of reflection of (a) X-rays diffraction and (b) electron diffraction, and their interaction with the reciprocal lattice. (a) λ is the incident wavelength and $1/\lambda$ is the radius of the sphere. Vector CO ($\boldsymbol{S_0}$) is the wave vector of incident beam, and O is the origin of reciprocal lattice, $\boldsymbol{S_1}$ is any wave vector. The Bragg condition is satisfied when the sphere cuts through a reciprocal lattice point, i.e., $\boldsymbol{h} = \boldsymbol{S_1} - \boldsymbol{S_0}$ is a reciprocal lattice vector. (b) As incident electron wave has a smaller wavelength, the sphere will interact with more reciprocal lattice points.

When an image of the back focal plane is projected onto the detector, an electron diffraction pattern (DP) is obtained (Figure 2.2(b)). Usually a selected area aperture is employed to isolate a specific region of interest that contributes to the diffraction pattern, so it is often referred as selected area electron diffraction (SAED) pattern. Electron diffraction exhibits four main distinctions from X-ray diffraction.[100; 97] First, the electron wavelength is significantly shorter than that of X-rays (e.g. $\lambda_e = 2.51 \times 10^{-2}$ Å for 200 kV electrons, in comparison with $\lambda_X = 1.54$ Å for Cu $K\alpha$ X-rays), resulting in a much larger Ewald sphere in reciprocal space (Figure 2.4. Second, the thinness of the sample causes each reciprocal lattice point to appear elongated along the direction of the incident beam. As a

result, the Ewald sphere intersects with a greater number of points, including those that are slightly away from Bragg's law, leading to the observation of numerous diffraction spots. Third, diffraction patterns can be acquired from small and precise locations within the specimen, making it ideal for nano-area investigation. Finally, diffracted intensities in electron diffraction are strongly affected by multiple scattering, which makes it less suitable for structure solution. However the breaking of Friedel's law that results from multiple scattering[101] has the advantage that the change of local structure can be readily spotted. This is particularly useful for ferroelectric materials since the polarity of the material can change diffracted intensities and thus give image contrast.

2.2.3 Diffraction contrast imaging

In conventional TEM imaging the beams diffracted by the sample are focused on top of each other to provide a final image (Figure 2.2(a)). However, using an objective aperture it is possible to allow only one diffracted beam through to form a dark field (DF) image (Figure 2.2(c)). This image will give an indication of where the diffraction is stronger/weaker at the reciprocal vectors selected by the aperture, i.e., the area appears bright is where the Bragg condition is met. Diffraction contrast images are usually acquired under two-beam condition[97] where the specimen is tilted in such a way that only one diffracted beam is strong, apart from the direct beam. A displacive ferroelectric may scatter the electrons differently for different polarisation directions and DF images can be used to visualise the domains.

2.2.4 CBED

If the incident beam is converged onto a single point on the specimen, a convergent beam electron diffraction (CBED) pattern[101] is formed at the back focal plane (Figure 2.2(d)). In contrast to the discrete spots observed in an SAED, the CBED pattern consists of circular discs, which correspond to the range of incident momenta. Each disc encompasses a multitude of additional features resulting from dynamical scattering, and these features are often utilized to determine the crystal's symmetry, making it a great tool to study displacive ferroelectrics. In comparison to other diffraction techniques, CBED offers a significant advantage as it extracts most of its information from minute regions that are beyond the reach of alternative diffraction methods.

2.2.5 Scanning transmission electron microscopy

Scanning transmission electron microscopy (STEM) differs principally from TEM in the way it addresses the specimen. This mode of operation requires the beam to be condensed down to a point, created by a probe forming lens before the specimen, to address each pixel in series as the probe rasters across the specimen. At each point on the sample, the intensity of the transmitted electrons is collected at a set of scattering angles to form images. The most common imaging modes are annular dark field (ADF) that collects a ring of high scattering angles, and bright field (BF) that collects a disk of low angles, as well as annular bright field (ABF) which blocks the direct beam, usually by a beam stopper (Figure 2.1(b)).

The most commonly used imaging detector in STEM is the annular dark field (ADF) detector, which consists of a ring detector positioned at the center of the optic axis (see Figure 2.1(b)). Typically, the ADF detector has a semi-angle ranging from approximately 50 to 150 mrad, while the incident beam has typical semi-angles of < 30 mrad.[97; 96] Because of the large detector area, ADF imaging can be described as incoherent imaging and is therefore insensitive to phase information.[96] Consequently, the resulting images are intuitive, where regions with higher signal or intensity correspond to the positions of atoms, while regions without signal represent vacuum. The scattered intensity is approximately proportional to the square of the atomic number (Z^2) of the atom column. However, it is worth noting that the exact exponent of proportionality may deviate from Z^2, depending on the collection angles of the detector, and can be as low as $Z^{1.5}$.

The primary alternative is the bright field (BF) detector, where a circular detector with a collection range approximately matching the incoming probe angle (~ 30 mrad) is placed on the beam axis (Figure 2.1(b)). Its main apparent difference from ADF is that the image appears inverted: low intensity indicates scattering by atom columns, while full intensity corresponds to vacuum. However, BF imaging involves more than just this inversion. The phase differences between the diffracted beams overlap and give rise to fringes that correspond to the atom planes. As these fringes are of similar size to the BF detector, this phase contrast is retained in the final images, leading to coherent imaging. This is in contrast to ADF's incoherent imaging, where the large detector averages over multiple fringes. An extension of BF is annular bright field (ABF), where the centre region (< 10 mrad) of the BF signal is blocked (in our lab it is achieved by the insertion of a beam stopper). ABF imaging allows for the visualization of very light atoms (such as carbon and oxygen), which typically provide weak contrast because at lower angles, the phase contrast is destructive, and any phase shifts can only increase constructive interference while at

the outer angles (about $10-20$ mrad) the opposite is true.[96; 98] By selecting only the destructive interference in the outer BF region, the contrast of atom columns is enhanced.

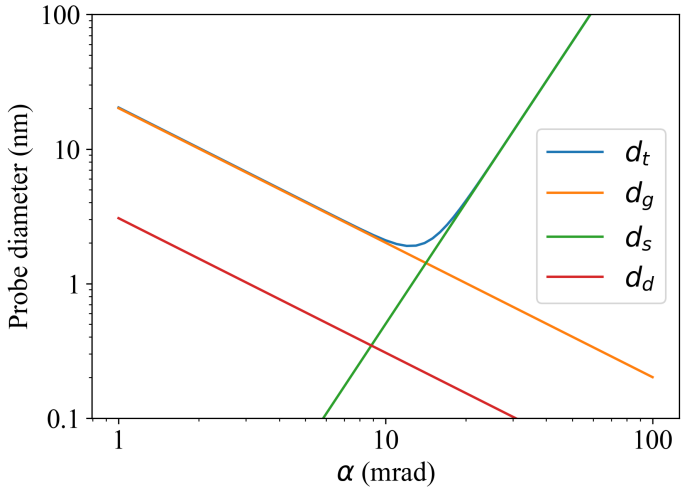

Figure 2.5: Plot of STEM probe diameter on varying convergence semi-angle α (i.e. choice of condenser aperture). d_t is the total diameter, made up of components from electron gun (d_g), diffraction (d_d) and the aberration term (d_s). Parameters used for the estimation are $i_p = 10^{-8}$ A, $\beta = 10^{13}$, $C_s = 1$ mm.

Resolution of STEM in principle is determined largely by the beam diameter generated by the probe forming lens which is also limited by aberrations. The probe diameter is determined by an initial Gaussian diameter at the electron gun (d_g).[97; 98] This diameter is broadened by the effects of spherical aberration in the probe forming lens (d_s) and diffraction at the final aperture (d_d). The expression for d_g is

$$d_g = \frac{2}{\pi}\left(\frac{i_p}{\beta}\right)^{1/2}\frac{1}{\alpha} \tag{2.8}$$

where i_p is the probe current, β is the brightness and α is the semi-convergence angle. The disc of minimum confusion caused by aberration $C_{N,S}$, for simplicity only the aberrations with cylindrical symmetry (N is odd and $S = 0$) are considered, has a diameter given by

$$d_s = A_N^2 C_{N,0}\alpha^n \tag{2.9}$$

where A_N is a constant and for chromatic aberration $A_1 = \Delta E/E_0$, for spherical aberration $A_3 = 0.5$.[96] The calculated diameter due to diffraction is the Rayleigh

criterion[97] which refers to a spacing between two overlapping images of the probe

$$d_d = 1.22\frac{\lambda}{\alpha} \tag{2.10}$$

where λ is the electron wavelength (about 2.51 pm at 200 kV). All these terms give an estimated total beam size (d_t) as

$$d_t = (d_g^2 + d_s^2 + d_d^2)^{1/2} \tag{2.11}$$

It can be seen from Figure 2.5 as well as their respective expression that, the component from electron gun (d_g) and diffraction (d_d) give a smaller probe as the convergence semi-angle increases, while the aberration term (d_s) keeps increasing and from a certain point it will dominate the probe diameter.

Resolution is also limited by imperfections in the scanning system, where the precise beam position may not align perfectly with the pixel grid of the image. Additionally, since the acquisition for each pixel occurs sequentially, any specimen drift during the image capture time can introduce distortions in the final image. One simple yet effective approach to address specimen drift is to wait for the sample to stabilize and maintain low environmental noise levels during the scanning process. However, it is important to note that some degree of drift will inevitably occur due to microscope or holder design as well as thermal expansion. In practice, one method to compensate for specimen drift is by employing drift correction techniques. A region of the specimen with suitable contrast and detail, close to the area of interest, is selected as a drift correction area. A short exposure survey image is initially acquired, which includes this region. Since the acquisition time is brief, any drift during this period has a negligible impact. Subsequently, during the image acquisition process, the acquisition is intermittently interrupted, such as after every tenth line, and the image of the drift correction region is re-acquired. By comparing this re-acquired image with the original reference image, the magnitude and direction of the drift can be determined and corrected. Another approach to mitigate specimen drift is to acquire a sequence of successive image scans, forming an image stack. Each rapid scan in the stack minimizes the drift, while simultaneously increasing the signal-to-noise ratio. Later, image analysis techniques can be utilized to combine the stack, effectively averaging out the imperfections caused by individual scans, thereby reducing the impact of drift.[102]

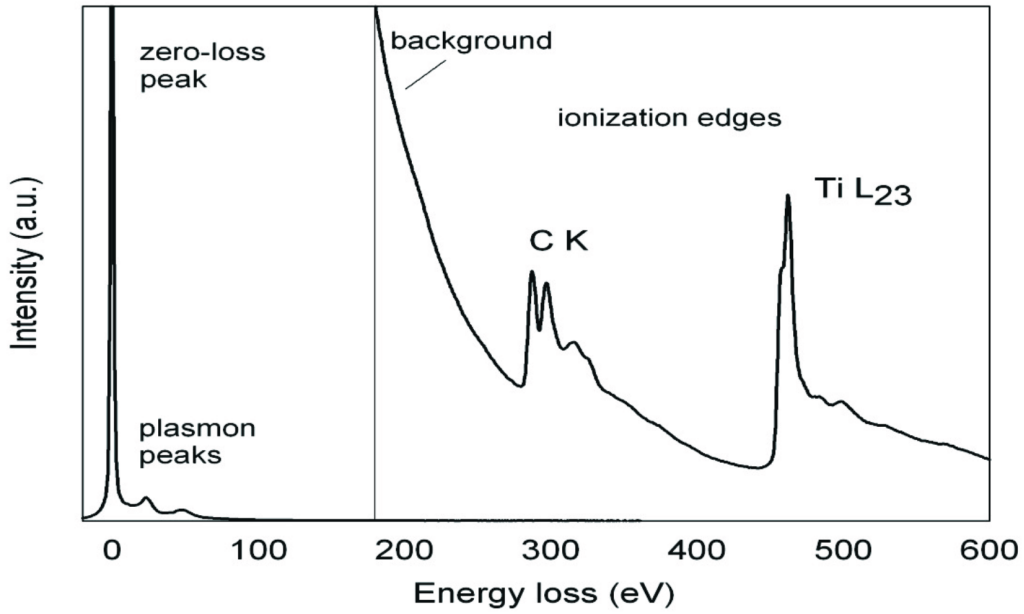

Figure 2.6: EELS of a 20 nm thin titanium carbide specimen recorded in a conventional 200 kV TEM equipped with an energy-filtering spectrometer. Reprinted figure with permission from IOP Publishing.[103]

2.2.6 Electron energy loss spectroscopy

A typical Electron Energy Loss spectrum (EELS) consists of three regions: the zero energy loss peak, the low loss region, and the high loss region (an example[103] can be found in Figure 2.6). The zero loss peak, situated around 0 eV, exhibits the highest intensity within the spectrum and contains elastically and quasi-elastically scattered electron components. The spectral resolution, quantified by the full width half-maximum (FHWM) of the zero loss peak, mainly depends on the inherent energy dispersion in the electron source which typically ranges from $\sim 0.3 - 2$ eV, depending on the type of emitter. Recent advancements in electron monochromators have enabled achievable resolutions < 6 meV.[104]

The low loss region spans from the zero loss peak up to ~ 50 eV energy loss and reflects the collective excitation of electrons in the outermost atomic orbitals. This region unveils the solid-state characteristics of the specimen, manifesting features arising from resonant plasmon oscillations of valence electrons and inter-band transitions from valence to conduction bands.

The high loss region extends from ~ 50 eV to several thousand eV and reflects the atomic nature of the specimen. Within this region, ionization edges become apparent, corresponding to the excitation of inner shell electrons superimposed on

a gradually decreasing background intensity. This region contains the excitation of electrons from localized orbitals to extended and unoccupied electron energy levels situated just above the Fermi level of the material, thus it is characteristic for the elements involved. The various ionization edges are classified using conventional spectroscopic notation, such as K excitation for the ionization of $1s$ electrons, L_1 for $2s$, $L2$ for $2p1/2$, $L3$ for $2p3/2$, and M_1 for $3s$, and so on. Since the energy of the ionization edge threshold is determined by the binding energy of the particular electron sub-shell within an atom–a characteristic value, the atomic type may be easily identified with reference to a tabulated database (for example, the EELS database in the Gatan DigitalMicrograph software).

In solids, the unoccupied electronic states near the Fermi level, i.e., the highest occupied electronic energy level, can be modified by chemical bonding, leading to a complex density of states (DOS) and this is reflected in the electron energy loss near-edge structure (ELNES) which lies superimposed on the basic atomic shape within the first 30–40 eV above the edge threshold. The ELNES effectively represents the available electronic states above the Fermi level, specific to the environment of the atom being ionised, and hence gives information on the local crystallographic structure and chemical bonding.[96]

2.2.7 Specimen preparation

The imaging principles in TEM/STEM mentioned above work together to achieve the best resolution. However, they would work in vain if the specimen is not of good quality. And for our experiment, a good specimen refers to one that is thin enough for incident electrons to pass through with minimal phase shift and beam spread. At the same time, it should be thick enough to withstand beam radiation without melting and maintain its characteristics. Usually the specimen should have a wedge shape with the thinnest part, typically bombarded to be amorphous, at the edge, and gradually increasing in thickness. In this thesis, most of the images with atomic resolution were captured in the crystalline region located just adjacent to the amorphous layer.

Conventional TEM sample preparation involves a combination of mechanical polishing and a subsequent ion thinning. The sample is first thinned down to $\sim$ 20 μm via polishing using diamond lapping film of decreasing sizes to 0.1 μm. Then the specimen is thinned to electron transparent using a Gatan precision ion polishing system (PIPS) using argon ions accelerated at 5-6 kV at incident angles of 3° and 4°. To remove redeposition and surface damage, final thinning was performed using 3 kV.

Focused ion beam (FIB) has been a popular technique due to its advantage in easy preparation of specimens at specific sites with designed orientations. The FIB uses a high energy Ga^+ beam to precisely bombard the target area of the sample surface, fabricating a small lamella which is subsequently lifted out and attached to a TEM copper grid (since FIB preparation has been used throughout this work, the term 'lamella' will be used as an equivalent to 'TEM sample'). Then, the sample is thinned to electron transparency using the ion beam (accelerating voltage 30 kV) at an incident angle of 1.5° to the surface. As the lamella gets thinner, the accelerating voltage of the ion beam has to be lowered, otherwise a single scan under 30 kV would be enough to destroy the sample. Usually, final polishing is performed at an accelerating voltage of 5 kV or 2 kV. During the lifetime of a TEM sample, contamination from air or the microscope chamber would be an inevitable but critical problem for atomic resolution imaging. Thus, it is a good idea to clean the sample before a TEM session, either by FIB/PIPS low voltage cleaning or high temperature baking.

Finally, it is important to consider the potential influence of sample preparation on the experiment. For example, will the FIB milling change the domain structure by exposing the material to air or by ion beam radiation? As will be discussed later in this thesis that the domain structure can hardly be moved by electron beam radiation or PFM high-voltage poling, meanwhile the domain structures observed by TEM/PFM show a good consistency (also with previous publications), we believe that sample preparation will not change the domain structure of this sample, and what we have observed in the microscopes is authentic to the actual domain structure inside the crystals.

2.2.8 Microscopes

In this thesis, TEM and STEM images are collected using two dedicated microscopes. Conventional TEM images, diffraction contrast images, SAED and CBED patterns were collected on a JEOL 2100 fitted with a LaB_6 source operated at an accelerating voltage of 200 kV and using a Gatan Orius CCD camera. STEM BF, ABF and ADF images were collected on a JEOL ARM-200F with a Schottky filed emission gun operated at 200 kV. The ARM is aberration-corrected both in probe-forming optics (probe size FWHM < 80 pm) and in image-forming optics (image resolution < 80 pm).[98] The ARM uses JEOL ADF ($75 - 280$ mrad) and ABF ($11.5 - 24$ mrad) detectors and Gatan Orius SC1000 CCD camera. A Tescan Amber dual beam FIB-SEM is used for TEM sample preparation. A Zeiss Axioimager optical microscope fitted with a light polarizer was used for mm-scale investigation.

EELS data and related HAADF images were acquired at the UK SuperSTEM Laboratory on a monochromated Nion UltraSTEM 100MC operating at 60 kV and beam convergence semi-angle of 32 mrad. The EELS and ADF acceptance semi-angles were 44 mrad and $79 - 185$ mrad, respectively.

2.3 Polarization Calculation at atomic scale

2.3.1 Theory and history

In Section 1.2, the modern theory of ferroelectricity was introduced based on which the ferroelectric $\boldsymbol{P_s}$ can be derived from Born effective charge and atomic shift, which enables direct calculation of $\boldsymbol{P_s}$ provided that atomic positions are available. To do that, one would need the Born effective charge of the relevant elements, ideally from related theoretical works, and the polar shift relative to the reference non-polar structure. Since it has been proved that the final $\boldsymbol{P_s}$ will not be influenced by the exact transition path,[55; 59] the reference non-polar structure is often taken after eliminating the polar strain of the ferroelectric structure, for example, simply elongate the PTO cubic cell along c axis, without any other sub-lattice shift, to reach a centro-symmetric tetragonal.[105] In practice, this is usually done by finding the A-site unit cell and defining its face/body center as the reference position of O/B-site atoms, and separation from those ideal positions is taken as polar shift.[90; 38]

The pioneering work of quantifying $\boldsymbol{P_s}$ by electron microscopy was conducted by Jia et al.[90] on a PTO thin film on a STO substrate. When the atomic displacement of Ti and O atoms are obtained from the atomic resolution images by negative C_s TEM, the author proposed the following equations

$$\boldsymbol{P_s} = k(\boldsymbol{\delta_O} - \boldsymbol{\delta_{Ti}}) \tag{2.12}$$

$$\boldsymbol{P_s} = \frac{1}{v}(3\boldsymbol{\delta_O}\bar{Z}_O + \boldsymbol{\delta_{Ti}}\bar{Z}_{Ti}) \tag{2.13}$$

where k is a constant, δ_i is the atomic shift of atom i compared to the Pb unit cell, v is the unit cell volume and Z_i is the effective charge of atom i.[106] Equation 2.12 was inspired by Abraham et al.,[107] where the authors found that across multiple ferroelectric systems, there was a linear dependence of the polar shift versus the $\boldsymbol{P_s}$ value. While Equation 2.13 was the product of modern theory of ferroelectricity.[105] By combining Equation 2.12 and Equation 2.13, $k = 2726$ μCcm^{-2}nm^{-1} was obtained, and a $\boldsymbol{P_s}$ range of $20 - 50$ μCcm^{-2} was derived in their thin films.

Although the transfer of the linear dependence into the PTO system is not

very steady: in the original paper,[107] the linear dependence was found by comparison across multiple materials (for example, PTO vs LNO vs BTO), and no study has indicated that the dependence is applicable to only one material (for example, paraelectric PTO vs ferroelectric PTO). Yet later, this technique was applied to directly observe continuous electric dipole rotation in flux-closure domains in ferroelectric PZT,[108] and the experimental evidence was found to agree well with the theoretical prediction,[109; 110] as well as with the results of calculations for thin film epitaxial systems by first-principles techniques,[111; 112; 113; 93] showing its vivid usability.

This technique has been widely used to reveal atomic scale $\boldsymbol{P_s}$ distribution of various PTO-based samples[84; 43; 85] and achieved great success in a sense that the experimental work agrees well with simulations. Following those works, Nelson et al.[38] applied the linear dependence to calculate $\boldsymbol{P_s}$ in BFO as

$$\boldsymbol{P_s} = k\delta_{FB} \tag{2.14}$$

where $\boldsymbol{\delta_{FB}}$ is polar shift of Fe compared to Bi unit cell. The authors proposed $k = -2.5$ μCcm^{-2}pm^{-1}, and the minus sign means the $\boldsymbol{P_s}$ vector has a direction opposite to $\boldsymbol{\delta_{FB}}$.

2.3.2 Experimental

Above mentioned microscopy principles give us high quality atomic resolution images, which enables the following $\boldsymbol{P_s}$ calculation. The $\boldsymbol{P_s}$ calculation at atomic scale relies on the acquisition of the position of each atom column, and a critical step is to acquire high quality images. Conventionally, increasing the signal-noise ratio of an electron microscopy image, at a given instrument set-up, involves a longer acquisition time. This can be achieved by squeezing more pixels into the image and allocating a longer dwell time for each pixel, subsequently enduring image distortions which come from scan distortion or sample drifting; or, by collecting a stack of fast scan images, preferably with incremented scanning rotation,[114] and using alignment algorithm to eliminate distortion. Atomic resolution ADF and ABF STEM images in this work were collected in the latter fashion: a set of ADF and ABF images were collected in a stack, usually containing 12-20 fast scans with an incremental 90° scan rotation, were simultaneously collected and later aligned by the SmartAlign algorithm[114]. A slight Gaussian filter (sigma=1.0 and order=0) was applied to further eliminate noise. The atom position is identified and classified using either the Peak-Pair algorithm[98] or the Atomap package[115], while results

from the two are found to be very close.

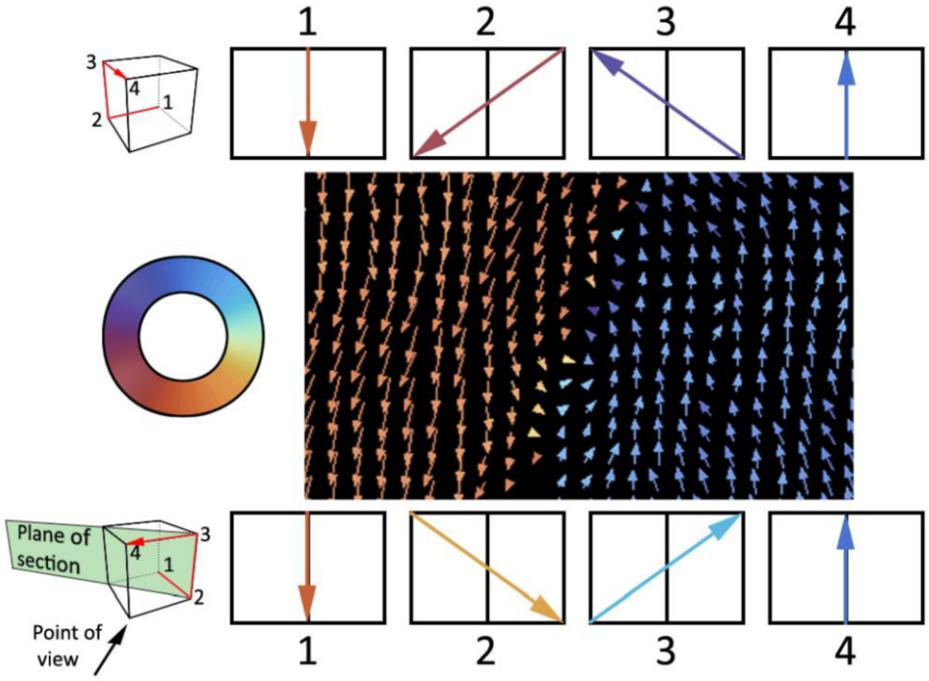

Figure 2.7: An example of different chiralities of the polarisation vectors at an inclined 180° domain wall, with their angle represented by a color wheel that is used throughout this thesis.

Once we have the position of atoms, it is important to categorise them into sub-groups, i.e., A-site, B-site or oxygen for perovskites. Conventionally, the A-site atoms are chosen to be the reference framework upon which the polar shift vector of B-site/oxygen atom is calculated (Figure 1.4); in another word, polar shift of A-site is set to be zero, which will not be a problem since we are actually interested in relative shifts. Calculated $\boldsymbol{P_s}$ vectors are represented by arrows in a quiver map,[108; 84; 85; 38] whose magnitude is linearly proportional to the shift value. A small imaging area gives sparse quiver map where the directions of $\boldsymbol{P_s}$ vectors are easy to see. However, if hundreds of vectors are included in one map, using a color wheel is a good idea to show the $\boldsymbol{P_s}$ rotation more clearly. An example of a colored quiver map is given in Figure 2.7 (the same color wheel is used throughout this thesis). Here we assume a rhombohedral unit cell where $\boldsymbol{P_s}$ lies along the body diagonal $\langle 111 \rangle$ pointing to Point 1. A 180° switch along the path 1-2-3-4 can happen via clockwise rotation (top) or counter-clockwise rotation (bottom), and their projection on a $\langle 110 \rangle$ plane is shown accordingly. With the color contrast, the chirality of the polarisation change (clockwise or anticlockwise rotation of the $-\boldsymbol{\delta_{FB}}$ vectors) can be clearly presented.

The polarisation component out of the image plane must pass through zero at some point between the two domains, and at this point the polarisation lies completely in the plane of the figure, as the case of Point 2 and Point 3. If the magnitude of $\boldsymbol{P_s}$ is unchanged (that is the Bloch-type wall), we would see the observed magnitude of the polarisation apparently increase at the domain wall, since there is no out-of-plane component. However, the opposite is found in the quiver map, indicating that the magnitude of polarisation is decreased at the domain wall (a mixture of Ising and Bloch type wall).

2.4 Piezoresponse force microscopy

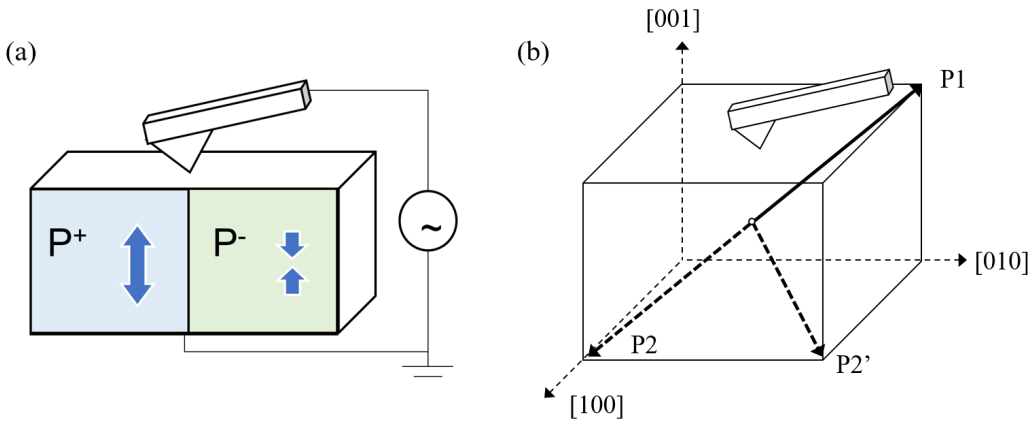

Figure 2.8: (a) Simplified scheme of PFM. An AC driving signal is applied between the tip and the sample. Domains with different $\boldsymbol{P_s}$ will correspond differently to the driving signal. (b) If P1 is taken as reference, PFM cannot distinguish the difference between P2 and P2′ since they both give opposite in-plane and out-of-plane contrast to P1.

Piezoresponse Force Microscopy (PFM) is an application mode of scanning probe microscopy (SPM) platform dedicated to imaging nanoscale domain structure in ferroelectric/piezoelectric materials.[116; 117; 118] The reason why we need the help of PFM in an electron microscopy-oriented thesis is that, PFM has been proved a powerful tool to image ferroelectric domains[21; 22; 119; 41] as it directly interacts with the inverse-piezoelectric property of ferroelectrics. While in electron microscopy we focus more on the structural aspects of the material, well-established PFM analysis procedure offers a good reference from the electrical side. Moreover, it is always worth trying a different sample preparation technique to double-check potential side-effects on the final domain structure.

SPM in general operates by moving a cantilever, with a sharp tip at its end, across the sample surface and at the same time detecting the cantilever's deflection caused by various tip-sample interactions such as mechanical, electrostatic, or magnetic. Different properties of the sample can be studied with high resolution and precision by altering the tip's type, controlling its movement, or applying additional stimulus to the system, thus changes the dominating interaction forces. In PFM mode, a small AC signal is applied to a conductive tip that is in contact with the sample (Figure 2.8(a)). As a result of the inverse-piezoelectric effect, the surface layers of the sample, typically a few nm thick, are distorted at the frequency of the driving signal.[116] At the same time, a laser beam is pointing towards the back of the cantilever and reflected onto a quadrant photodetector. Any movement of the cantilever will be captured by the photodetector and translated into electrical outputs. Response to the driving force varies on the piezoelectric tensors of the domains, therefore domains with different orientations exhibit different responses to the same driving force, which gives the contrast of phase/amplitude signals. Another popular PFM application is in switch mode, where a DC voltage is applied between the tip and the sample during a raster scan. If the tip-induced electrical field is stronger than the sample's coercive field E_c and opposite to the $\boldsymbol{P_s}$ direction, domains under the tip will be forced to switch its direction to align with the tip field.[117]

In order to interpret the domain structure under the tip, the primary signals used are the in-plane and out-of-plane phase signals. The in-plane component results from the cantilever's lateral declination, while the out-of-plane component is caused by its vertical deflection. A vertically (horizontally) antiparallel domain pair will result in a 180° out-of-plane (in-plane) phase contrast, as the case in Figure 2.8(a). However, it is important to note that an opposite contrast from both in-plane and out-of-plane phase channel does not necessarily mean there are opposite domains under the tip. For example, as shown in Figure 2.8(b), both domain P2 and P2′ will give an opposite in-plane (left vs right) and out-of-plane (down vs up) phase difference to domain P1, while P2 is a 180°-type domain to P1 but P2′ is a 109°-type. Of course, this problem is by no means exclusive to PFM and occurs as long as we are limited to see the projection instead of the real object in 3D space. In a TEM session, for example, we will not be able to distinguish P2 and P2′ if the incident beam is parallel to [010] axis in Figure 2.8(b) because their out-of-plane component will not be detectable.

In this work, PFM measurements were conducted on a Bruker Dimension Icon AFM at a scan rate of 0.5 Hz using a Bruker OSCM-PT-R3 tip with Pt coat-

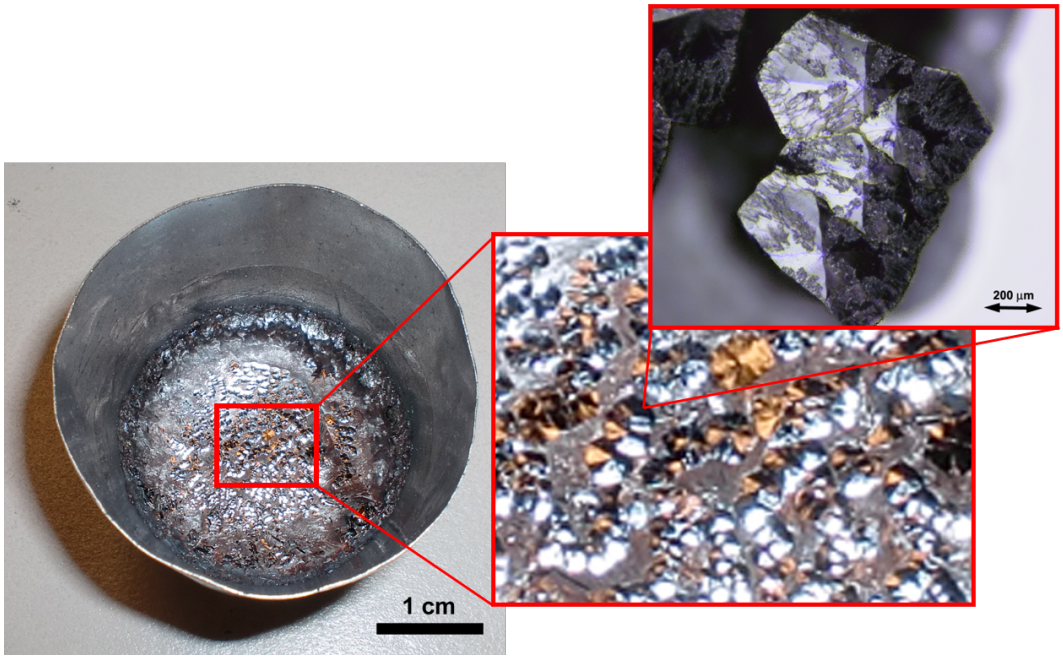

Figure 2.9: A platinum crucible after the growth of BFO single crystals. Enlarged visions show the what the crystals look like before/after exfoliated from the crucible. Image courtesy of Prof Marin Alexe.

ing, a drive frequency of about 254 kHz, that is left side shoulder of the contacting resonance peak (around $260 - 280$ kHz) to increase the strength of response signal, and a drive voltage of 2 V. PFM sample preparation is mostly mechanical. To minimize crosstalk between topography and piezoresponse signal, a simple but very effective way is to make the sample surface as flat as possible, so the topography feature is reduced to a much lower frequency. In our lab this is achieved by the same mechanical polishing procedure as the TEM sample preparation, using diamond lapping film of decreasing sizes to 0.1 μm, finishing with a dilute 0.04 μm colloidal silica solution. Particularly for the flux-grown single crystal BFO, a surface contamination layer, having the same stripe feature as the domains, will form if the sample has been exposed to the air for a period of time. A possible reason is the $\boldsymbol{P_s}$ discontinuity at the sample surface will attract polar molecules from the air. To collect data authentic to the real domain structure on the sample surface, it would be worthwhile to fine-polish the sample surface again immediately before each PFM session.

2.5 Sample growth

Even though growing BFO single crystals is difficult (Section 1.2.5), not to mention high quality ones, we are fortunate to be offered some best of the kind. The BFO single crystals investigated in this thesis were grown by flux growth technique.[32; 34] During the growth, a platinum crucible is loaded with a combination of dry powders of the flux, also known as the solvent, and the raw material.[46] The sealed crucible is then placed into a furnace and heated until the contents fully melt and form a homogeneous solution. Because the saturation condition is a dependence of temperature, decrease of the crucible temperature will push the solution into a state of supersaturation, where the solute concentration surpasses the solution's solubility limit. At this point, small microscopic nuclei of the desired crystal begin to appear, and as the temperature continues to drop, additional solute particles attach to the nuclei which eventually results in visible crystals. After reaching the endpoint temperature, the furnace is turned off and cools to room temperature (one crucible after a growth process is shown in Figure 2.9). Finally, the flux can be dissolved in hot acid which leaves only the target crystals inside the crucible. When deciding what flux material to use, various factors need to be taken into account. It is important to select a material that has a low melting point, has the ability to dissolve the target material without reacting with it, and ideally does not react with the platinum crucible and is easy to remove.

The flux-grown BFO single crystals investigated in this work were grown from a flux prepared on the basis of B_2O_3, Bi_2O_3 and stoichiometric $BiFeO_3$ corresponding to a net 4/1/0.8 $Bi_2O_3/Fe_2O_3/B_2O_3$ mole ration[34]. The milled starting mixture was homogenized in a platinum crucible for 12 h at 1170 K and subsequently cooled at a very slow rate of 0.01 K/min through the liquidus temperature of 893 K to 875 K followed by cooling to ambient temperature at a rate of 0.1 K/min. The platinum crucible can only be used once because the reaction of Bi_2O_3 with Pt during the process,[46] and only the crystals on top and are far away from the crucible walls are collected for further study. The same batch of crystals were also investigated in Refs. [32; 33; 34; 35].

Chapter 3

Domain structure inside single crystal BFO

3.1 Introduction

Domain formation in ferroelectric materials, and subsequently the domain size and shape, is the result of the material properties, its surface conditions and energy competition as the system seeks to attain the lowest energy profile (Section 1.3.1). Thus, a thorough investigation of the domain and domain wall structure is crucial for understanding the energy profile of the material and the physics of the domain interface, and promoting the advent of domain-/domain wall-based electronic devices.

Previous studies of flux-grown single crystal BFO have found a dense domain structure with alternating sawtooth and flat domain walls, while the nature of these domains and their 3D structure is under discussion and has remained elusive to date. In this chapter, we focus on exploring the domain structure in the single crystal BFO using various microscopy techniques including optical, PFM, diffraction-contrast TEM, CBED, SAED and STEM. By examining the domain structure at various scales, from millimeters to nanometers, all domain walls in this sample are found to be 180° type, with the flat walls being head-to-head polarity and sawtooth walls being tail-to-tail. Subsequently, a 3D model to explain this unique domain structure has been proposed, which is consistent with TEM observations from different view-directions. Finally, reasons of the deviation between existing studies have been covered.

3.2 Bulk domain structure

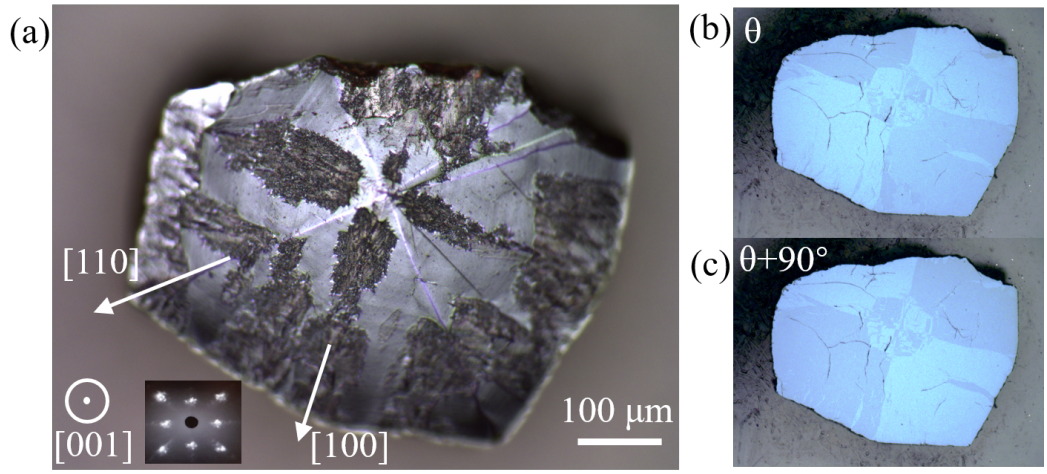

Figure 3.1: (a) A typical BFO crystal of its as-grown state with crystal orientation labelled. This crystal was subsequently polished parallel to (001) plane and (b) studied under a polarized optical microscope showing quadrant distribution of ferroelastic domains, whose contrast flipped (c) after the polarized light was rotated 90°. Laue diffraction, shown in (a) inset, indicates the [001] base direction of the crystal.

Figure 3.1(a) shows an optical image of an as-grown BFO crystal. The rosette-like crystal has a [001] orientated plateau and on its top there are four triangle facets aligned along [110] ridges. Its appearance resembles that of a flattened pyramid with a sturdy base. The typical diameter of the crystal ranges between 500 μm to a few mm, with a thickness of $100 - 300$ μm. The otherwise shining top-surface was marred by rough scratches after the crystals were exfoliated from the crucible by diluted HNO_3 (see Section 2.5), and the acid displayed a preferable etching orientation along [100] direction, which is at an angle of 45° to the [110] ridges. The backside surface of the crystal is very rough (not shown), and all TEM samples were left-out from the shinning area of the top-surface. Here a well-formed single sample is shown, while a larger sample is more likely to be found (inset of Figure 2.9) which contains multiple single crystals fused together.

The same sample in Figure 3.1 was polished parallel to the base plane and studied under polarized optical microscope (Figure 3.1(b) and (c)). At the scale of its size, the crystal has a quadrant distribution of four large domains separated by [100] domain boundaries, each taking up approximately 20 percent of the crystal's volume (slightly smaller than a quarter, because there is another set of smaller do-

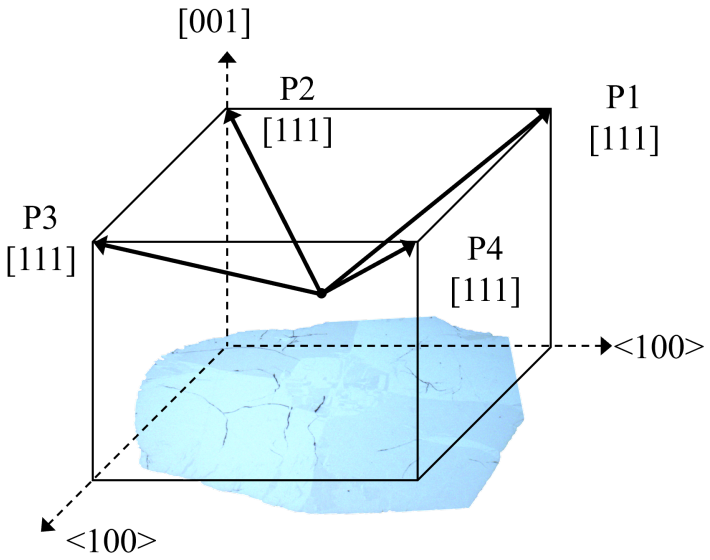

Figure 3.2: Quadrant ferroelastic domain distribution within the BFO crystal.

mains in the center of the crystal in Figure 3.1(b)). The domains' contrast switched after the polarized incident light was rotated 90° (i.e., 0° in Figure 3.1(b) and 90° in Figure 3.1(c)), a typical birefringence behaviour that shows the variation of ferroelectric polar axis.[45; 33; 31] So, those quadrant domains are 71° ferroelastic domains, and their polar distribution is shown in 3.2, following a typical domain pattern for rhombohedral perovskite ferroelectrics.[120] However, it should be noted that the birefringence behaviour of ferroelectrics only provides information on the variation of polar axis and cannot distinguish opposite polarities along the same polar axis, i.e., 180° ferroelectric domains. Therefore, it is not appropriate to conclude that these quadrant domains are 'single domains' based solely on the results from the polarized optical microscope (Ref.[121] for example).

3.3 Nanoscale domain structure

3.3.1 PFM observation of the domains

PFM provides evidence that the four large ferroelastic domains in the crystal are not single ferroelectric domains. The nanoscale domain structure of the same crystal in Figure 3.1(b) was revealed by PFM phase and amplitude images in Figure 3.3. In the phase images, the domain structure follows a stripe pattern where sawtooth domain walls are sandwiched by straight domain walls, with only two colors (representing the phase value) repeating in the whole scan area. The spacing between stripes(L)

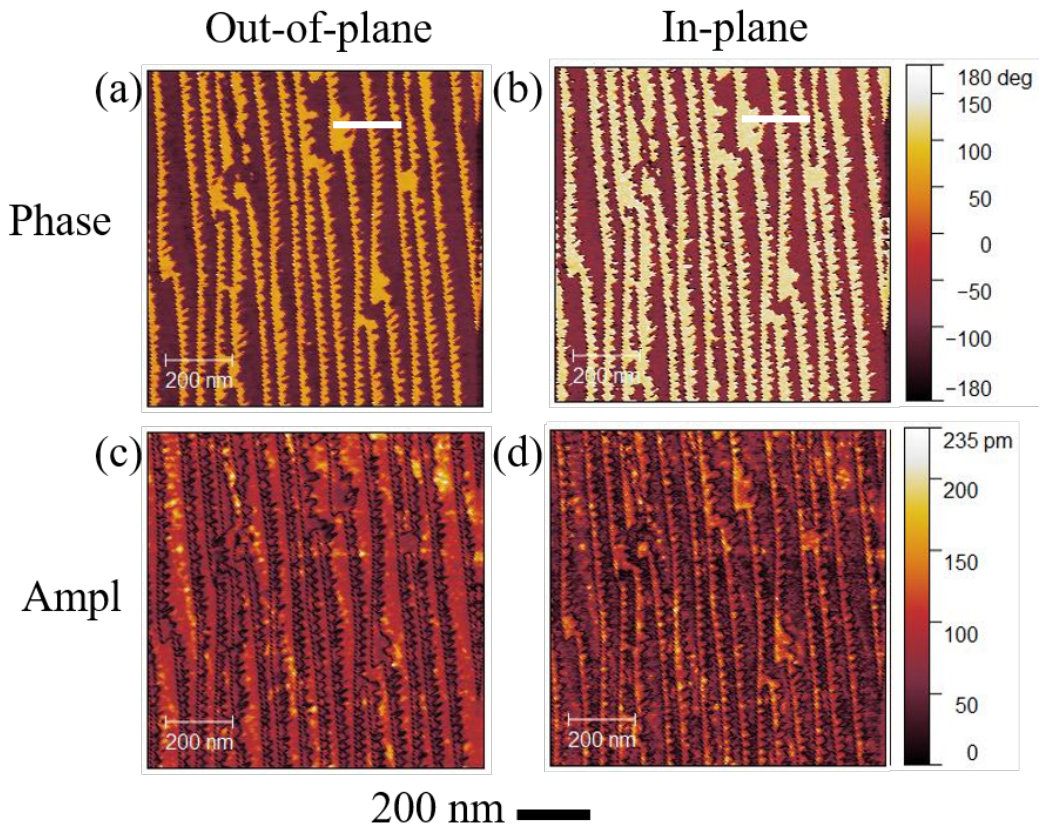

Figure 3.3: Simultaneously collected PFM out-of-plane (a) phase and (c) amplitude and in-plane (b) phase and (d) amplitude data on a random areas in Figure 3.1(b). View-direction is [001].

ranges from 60-120 nm, and the distance between two sawtooth vertices(w) varies between 20-40 nm. Although the domains' detailed appearance varies from location to location, PFM phase data (Figure 3.4) shows a consistent 180° phase difference across either sawtooth or straight domain walls, indicating that the domains have opposite in-plane and out-of-plane components. Based on the PFM's working principle (introduced in Section 2.2 and Figure 2.8(b)), the result suggests that the domain walls could either be 109° or 180°, but the equivalence can not be distinguished by PFM alone.[118]

Figure 3.5 presents a plot of L (the spacing between stripes) plotted against w^2 (square of the distance between sawtooth vertices), and the two variables should be linearly dependent if Kittel's square root law is applicable (Equation 1.7). In this sample, we found as L increases (the stripes become larger), w increases accordingly (the sawtooth domains tend to be larger as well). This relationship is understandable

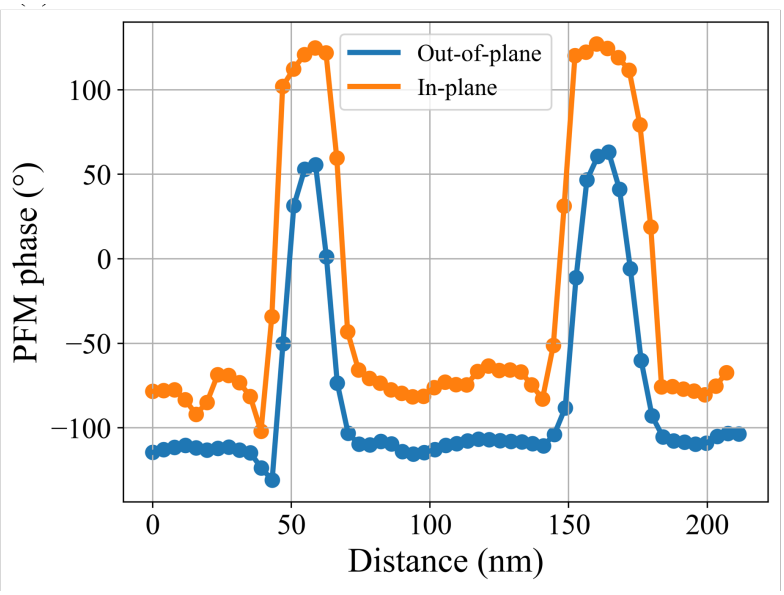

Figure 3.4: Value of PFM out-of-plane phase and in-plane phase, extracted from area 1 in Figure 3.3.

since the sawtooth domains occupy roughly half of the stripes' area. As for the linear dependence, we calculated a Pearson correlation coefficient of 0.684, showing a positive yet moderate correlation. The linear relationship is not evidently strong, and we do not find it suitable to conclude that the two variables follow the Kittel's square root law.

It is worth noting that we attempted several PFM switches on the sample by applying a DC voltage to the PFM tip during scanning to induce domain switch. However, even at the instrument's maximum DC amplitude of ± 10 V, no noticeable change in the domain structure can be observed. In contrast, a voltage of 2.5 V is usually sufficient to induce domain switch in thin-film BFO samples (with a thickness of hundreds nm) on this same PFM instrument. The reasons behind this sample's remarkable domain structure stability will be discussed in the following sections.

3.3.2 TEM observation of the domains

The challenge of obtaining a large, flat and steady area under the PFM tip makes it difficult to study the nanoscale domain structure from multiple view-directions. As a result, only [001] direction is used for PFM imaging of the crystal. To conduct a more detailed and comprehensive study, various FIB lamellae with different designed orientations were lift-out within a compact region near a [110] ridge from another crystal in its as-grown state. Lamellae with [110], [010], and [$\bar{1}$10] zone-axes

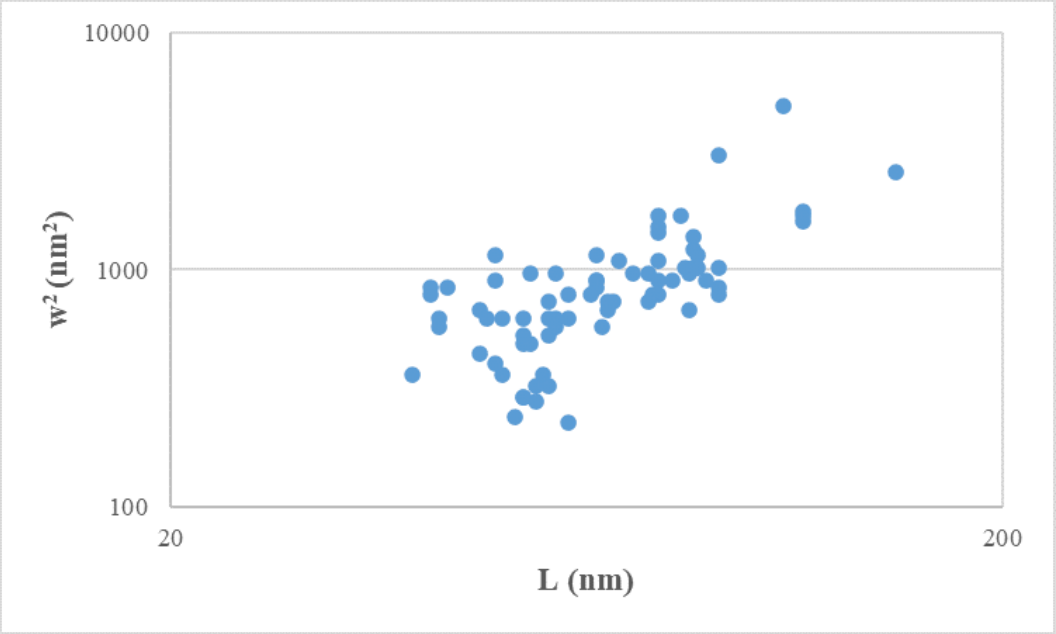

Figure 3.5: Log-log plot of w^2 (width between two sawtooth vertices) against L (distance between the two flat walls containing the sawtooth domains). Data are counted from $\sim$ 10 PFM images.

were studied under diffraction-contrast TEM (Figure 3.6(a)-(c), with [001] direction aligned upwards) which gives different dark/bright contrast for ferroelectric domains (Section 2.2.3). Intriguingly, the domains in these lamellae always appear with alternating flat and zig-zag sawtooth domain walls, same as the PFM result in Figure 3.3, irrespective of the plane of lamella or which area is chosen. At the same time, each orientation is found to have its distinct domain shape. For example, in the (110) lamella the straight bands are parallel to the (001) surface; while in the (010) lamella they are inclined at an angle of $\sim 25°$, running along the $[\bar{2}01]$ direction; in $(\bar{1}10)$ they are inclined at an angle of $\sim 35°$, running along $[11\bar{1}]$ direction. Meanwhile, the sawtooth structure also changes. From all view-directions, sawtooth walls appear as laterally connected V-shapes along the flat walls. While V-shapes in (110) sample are symmetric about [001] axis, when seen from the other two view-directions they are not symmetric against any axis, with one edge close to be perpendicular to the flat walls, and the other edge more inclined. Together, those observation difference leaves an impression that we are observing projections of a three-dimensional object- for example, imagine rotating the letter b and depending on the view-direction you might end up seeing letter d, p, q or l; or on a bad day, an ill-aligned microscope could give you a letter h. These could be the case of our

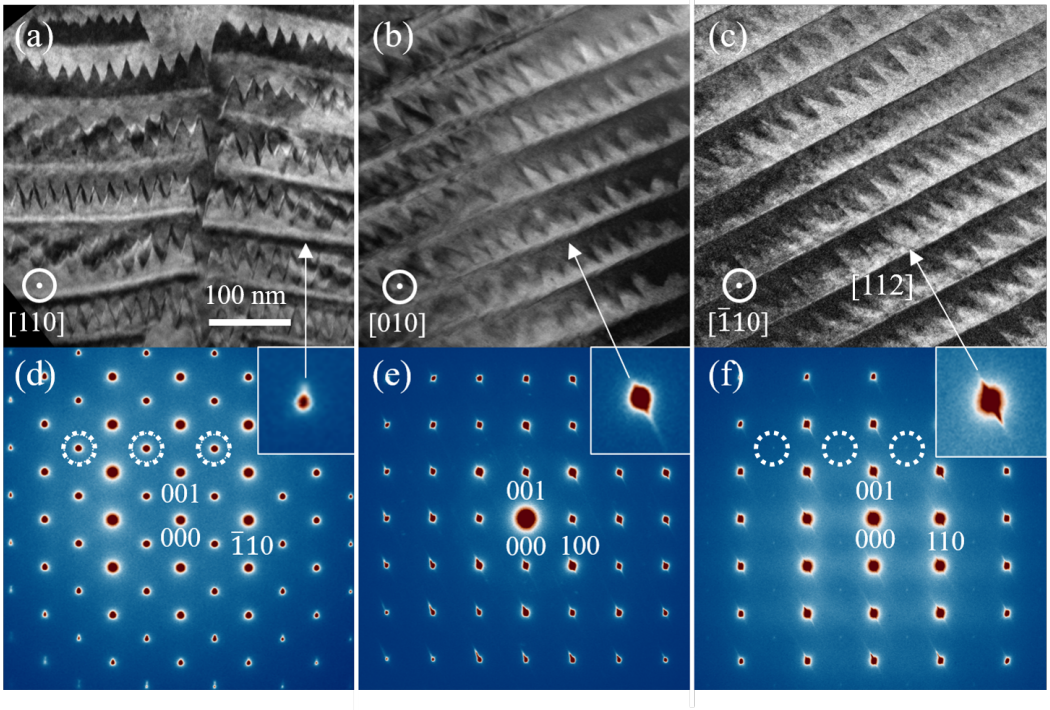

Figure 3.6: Diffraction contrast TEM images of (a) (110), (b) (010) and (c) ($\bar{1}$10) lamellae, the 100 nm scale bar applies to all three TEM images. SAED pattern of (d) (110), (e) (010) and (f) ($\bar{1}$10) lamellae. Some of the {½, ½, ½} superlattice reflections in (d) the (110) SAED are circled for highlight, which is missing in (f).

observations of those V-shapes, which will be investigated later in Section 3.3.4.

The lamellae's SAED patterns (Figure 3.6(d)-(f)) agree well with the simulated results of rhombohedral perovskites[64]. As the result of $a^-a^-a^-$ antiphase tilting about [111] axis, {½, ½, ½} superlattice reflections are present in the (110) SAED (circled in Figure 3.6(d)) but are absent in the ($\bar{1}$10) SAED (Figure 3.6(f)). An interesting feature of the SAED pattern is that the flat domain walls produce streaks along [112] in the [$\bar{1}$10] SAED, shown in the inset for Figure 3.6(f). In the [010] SAED, streaks are seen along [102] (inset Figure 3.6(d)), while in the [110] SAED the streaks run along [001] direction (inset Figure 3.6(e)); both correspond to the [112] projection onto each diffraction plane.

3.3.3 Determination of domain type

At the moment, based on PFM and SAED data the $\boldsymbol{P_s}$ of the sawtooth domains can be determined. PFM observations agree with those of previous studies[33; 34],

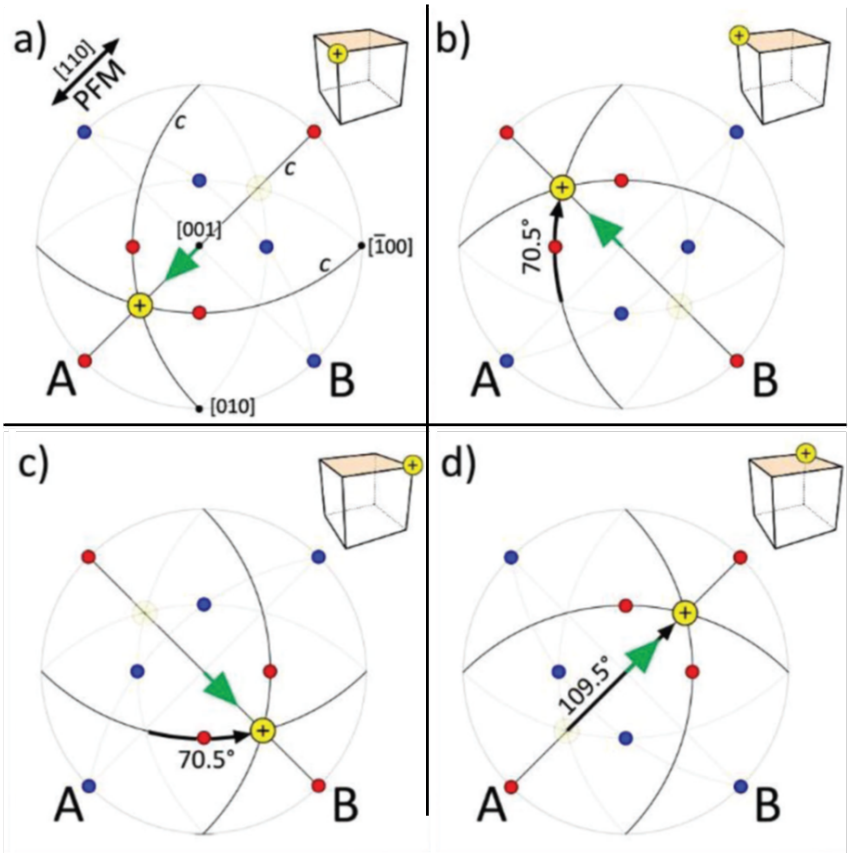

Figure 3.7: (Part 1/2) {001} Stereographic projections showing the eight possible orientations of the [111] polar axis in $R3c$ BFO as yellow circles, with the polarity marked + or -. The traces of the three c-glide planes are marked by solid lines, all other traces shown in grey. The polar axis on the opposite side of the projection is shown as a faint yellow circle and the in-plane component of the polarisation is shown by the green arrow.

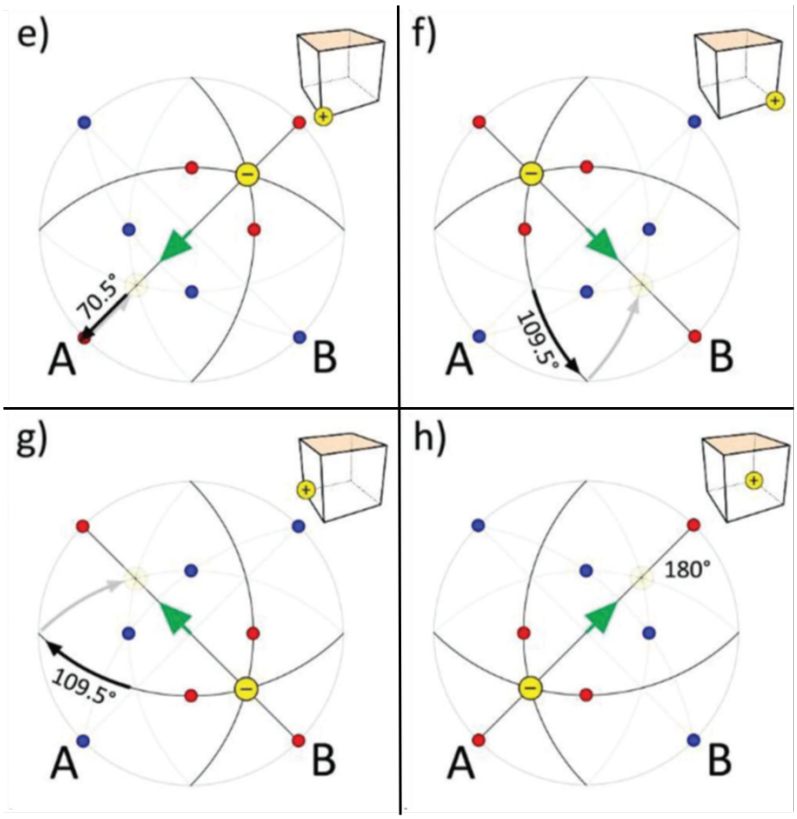

Figure 3.7: (Part 2/2) {001} Stereographic projections showing the eight possible orientations of the [111] polar axis in $R3c$ BFO as yellow circles, with the polarity marked + or -. The traces of the three c-glide planes are marked by solid lines, all other traces shown in grey. The polar axis on the opposite side of the projection is shown as a faint yellow circle and the in-plane component of the polarisation is shown by the green arrow.

showing a change in the phase of the PFM signal across the domain walls for both out-of-plane and in-plane components. The consistency of phase differences between domains in PFM shows that the material is essentially divided into just two domains, but it is not clear if they are 109° or 180° domains (reason explained in Section 2.4).

In an $R3c$ perovskite with a [111] polar axis, domain walls can be of 71°, 109° or 180° type and all the different possibilities of polarity are shown in Figure 3.7. Here, taking (a) as the orientation of a domain with positive polarity in the PFM image, this requires the second domain to have a change in the out-of-plane component (yellow circle) from + to -, and a change in direction of the in-plane component (green arrow). This leaves only (f), (g) or (h) as possibilities, but PFM cannot distinguish between them. Additional information can be provided by at zone axes of the type $\langle 110 \rangle$, which have half odd-odd-odd {½, ½, ½} spots if the zone axis is at an angle of about 35° to the [111] polar axis (for example [110] axis), while these spots are absent from the zone axes that are perpendicular to [111] polar axis (for example $[\bar{1}10]$ axis)[64; 65]. These zone axes are marked by red and blue dots, respectively, on Figure 3.7. The orientation of the two $\langle 110 \rangle$ SAEDs shown in Figure 3.6(d) and 3.6(f) are marked in Figure 3.7(a) by A and B respectively. It is important to note that the diffraction volume that contributes to a SAED is much larger than the domain size here; these diffraction patterns sample over many domains. In Figure 3.6(f) it is clear that the $[\bar{1}10]$ SAED has no {½, ½, ½} spots indicating that the latter is perpendicular to the polar axis for both domains. Thus, in Figure 3.7, the equivalent of point B in the second domain remains blue, eliminating (b), (c), (f) and (g). The only possibility consistent with both PFM and SAED is that the domain walls are of 180° type shown in Figure 3.7(h).

In CBED the electron probe can be made small enough (< 10 nm diameter) to be placed inside individual domains, avoiding the averaging effect of SAED. The patterns obtained from such a measurement at the [110] zone axis are shown in Figure 3.8(a)-(d). The CBED patterns from both domains have {½, ½, ½} spots and $(\bar{1}10)$ mirror symmetry, with intensities in Figure 3.8(b) and (c) that are related by a 180° rotation or horizontal (001) mirror plane. Figure 3.8(d) shows a simulated pattern at a specimen thickness of 10.6 nm with a known direction of polarization. Comparing simulation with experiment reveals that polarization points towards flat domain walls and away from sawtooth domain walls. A similar set of $[\bar{1}10]$ CBED measurements is shown in Figure 3.9(a)-(d). The patterns of Figure 3.9(b) and (c) have no mirror symmetry, and here the intensities in adjacent domains are related by a 180° rotation. Comparison with simulation, Figure 3.9(d), gives the direction of polarization. These results are consistent with the [110] CBED measurement,

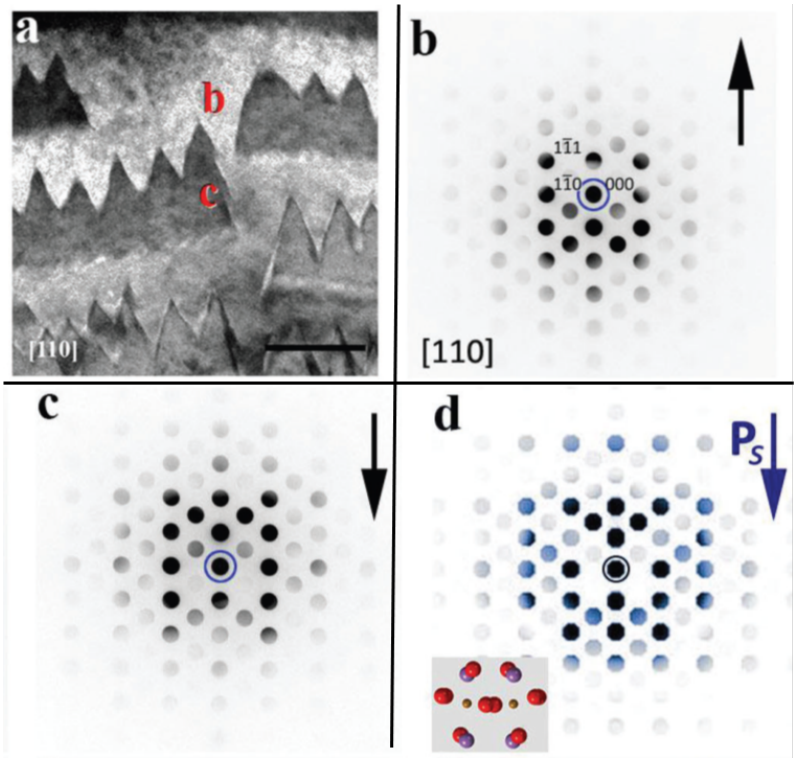

Figure 3.8: CBED data sets of (110) BFO single crystal sample. (a) Diffraction contrast TEM image with beam direction parallel to [110] direction, and the crystal orientation applies to (b-d). Areas where the converged beam was placed are marked correspondingly in the TEM images, accompanied by arrows showing $\boldsymbol{P_s}$ direction. Scale bars 50 nm. (b-c) CBED patterns collected at domains with opposite TEM contrast, and insets show their corresponding unit cell projection. (d) Simulated CBED pattern for 10.6 nm thick (110) BFO specimen. During the experiment, multiple positions on the lamellae have been chosen to collect CBED data, and no other diffraction pattern can be observed except the results shown here.

showing the flat walls have head-to-head $\boldsymbol{P_s}$ and the sawtooth walls have tail-to-tail $\boldsymbol{P_s}$. They are also consistent with the PFM and SAED observations and with consideration to Figure 3.7 these results eliminate (d) and (e), showing that the two domains present are those shown in Figure 3.7(a) and (h) and are of 180° type.

3.3.4 Domain geometry

Flat domain walls

Having established the type of domain wall, we now consider the domain structure. Let us start from the flat walls because their stripe structure is much simpler than the sawtooth walls. Previous studies concluded that the flat walls are flat

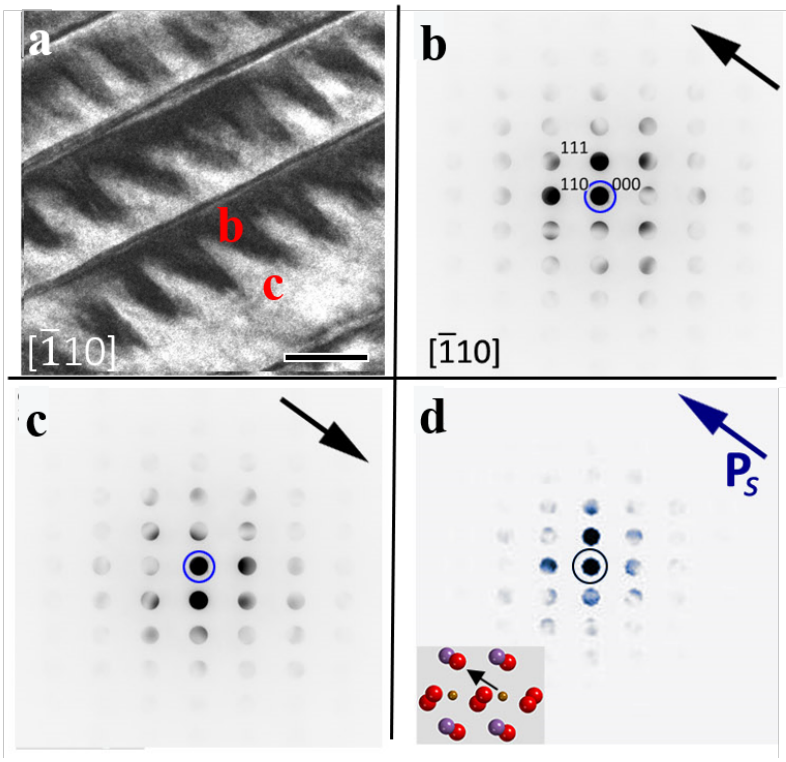

Figure 3.9: CBED data sets of ($\bar{1}$10) BFO single crystal sample. (a) Diffraction contrast TEM image with beam direction parallel to [$\bar{1}$10] direction, and the crystal orientation applies to (b-d). Areas where the converged beam was placed are marked correspondingly in the TEM images, accompanied by arrows showing $\boldsymbol{P_s}$ direction. Scale bars 50 nm. (b-c) CBED patterns collected at domains with opposite TEM contrast, and insets show their corresponding unit cell projection. (d) Simulated CBED pattern for 81.6 nm thick ($\bar{1}$10) BFO specimen. During the experiment, multiple positions on the lamellae have been chosen to collect CBED data, and no other diffraction pattern can be observed except the results shown here.

domains with finite width[33], and the reason of this misconclusion can be easily understood by STEM BF images (Figure 3.10). In all orientations the domain walls appear as alternating sawtooth and straight bands of contrast, same to the PFM result collected from (001) planes (Figure 3.3) and diffraction-contrast TEM images (Figure 3.6). In these BF images, the crystal is aligned to the zone axis and local conditions such as strain, composition, or a small change in crystal orientation across a boundary, can strongly affect transmission of the electron probe.[96] As a result, domain boundaries appear darker and we see a variation of the width of the straight bands, changing from position to position and from sample to sample (Figure 3.11). Their width in (110) and (010) lamellae (about $25-50$ nm) is noticeably

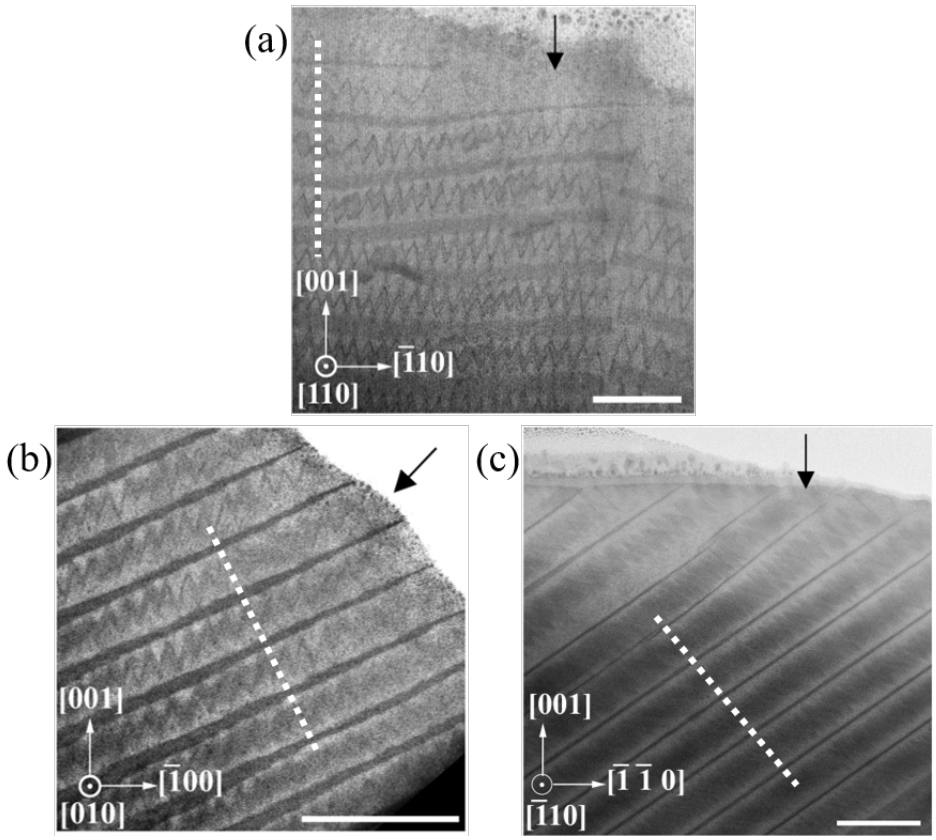

Figure 3.10: STEM BF images of (a) (110), (b) (010) and (c) ($\bar{1}$10) lamellae. The [001] base direction of the crystal is aligned upwards in those images. Black arrows are placed at the thinnest part of each lamella and pointing to the thickness increase direction. Scale bars are 100 nm.

larger than ($\bar{1}$10) lamella (about 8 nm). Besides, there is a clear pattern that in (110) and (010) lamellae the straight bands' width decreases as they approach the edge of the sample, while in ($\bar{1}$10) lamella they keep a thin profile throughout the whole sample.

Here we are reminded that the FIB sample preparation produces wedge-shaped lamella with its thinnest part at the edge (Figure 3.12), so there is a gradual increase of sample thickness from the edge towards the body (the increment direction is denoted as black arrows in Figure 3.10). As a result, even a thin object inside the lamella could be projected into a wider band on the detector plane if the object is inclined to the view-direction (Figure 3.12(a) and (b)), and this model explains perfectly the STEM observation (Figure 3.10(a) and (b)). At the same time, there shall exist such an edge-on view-direction that the thin object is projected into a single line whose thickness is independent of the lamella thickness (Figure 3.12(c)).

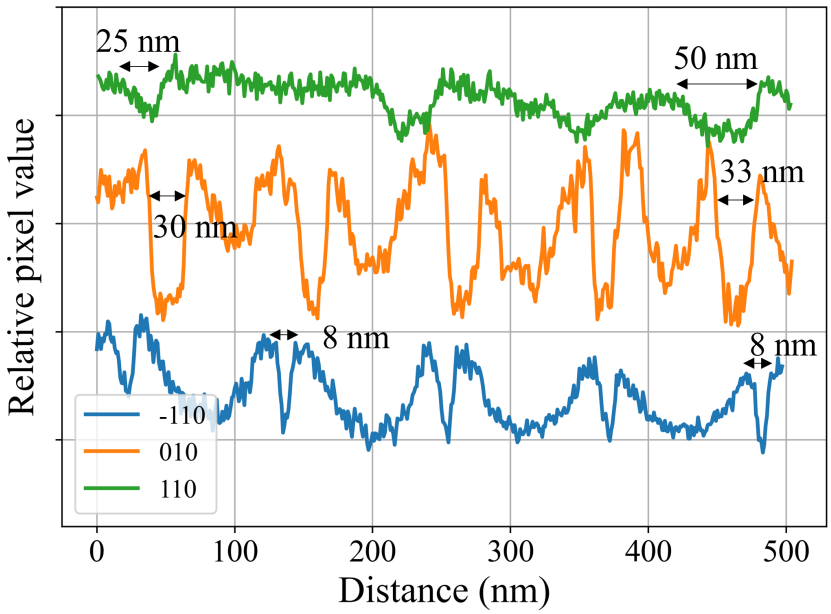

Figure 3.11: Pixel value profiles of STEM BF images in Figure3.10, extracted perpendicular to the flat domain walls. The drop in the profile shows the position and width of the straight bands since they appear darker in the BF images.

And it is exactly the case seen from [$\bar{1}10$] view-direction (Figure 3.10(c)).

Along with the qualitative description, there should exist a valid quantitative representation of this analysis, that is the mathematical indexing according to the crystal lattice. Not surprisingly, the orientations of the straight bands, [001] in the (110) lamella, [$\bar{2}01$] in (010) lamella, [$11\bar{1}$] in ($\bar{1}10$) lamella and [$02\bar{1}$] in ($\bar{1}12$) lamella, as well as their appearance as streaks in the SAED patterns (Figure 3.6 (d)-(f)), all correspond to the projection of (112) planes into respective image planes. So, we know that those straight bands are not separate stripe domains; instead, they are flat domain walls running along (112) planes inside the crystal. And we are confident now that the domain structure in this crystal is indeed three-dimensional, on which later analysis will be based.

Sawtooth domain walls

Orientations of the sawtooth domain walls can be determined by counting their positions on the lattice when high-resolution atomic images are available (Figure 3.13). When observed from a [110] view-direction, the sawtooth domain walls appear as projected edges along the [$1\bar{1}5$] and [$\bar{1}15$] directions, symmetrically positioned about the [001] axis. However, when viewed from the [$\bar{1}10$] direction, one edge is pro-

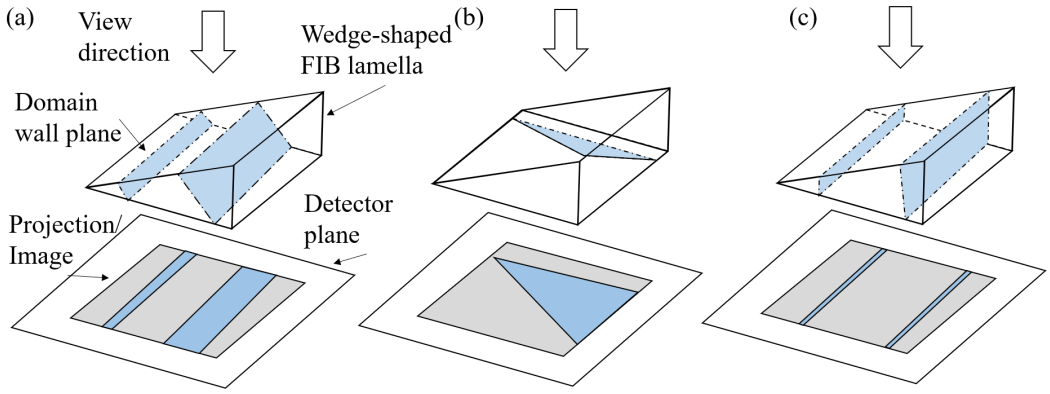

Figure 3.12: Projections of planes inside a wedge-shaped lamella sample. If the planes are inclined to the view-direction like (a) and (b), they will be projected into wider bands whose thickness is dependent on the wedge thickness. If the planes are parallel to the view-direction like (c) and seen edge-on, they will be projected into thin bands with constant thickness.

jected as [111], running parallel to the polar axis and nearly perpendicular to the flat wall, while the other edge is projected as [221]. The next step is to establish a 3D structure that satisfies the following requirements: first, the structure is going to be projected into zig-zag shapes despite the choice of view-direction; and second, mathematical expression of the structure and its projection need to follow the self-consistent numbers given above, like our analysis of the flat walls. The calculation is simple: two crossed lines determine a plane by their cross product. For example, the facet projected into $[1\bar{1}5]$ in (110) lamella and [221] in $(\bar{1}10)$ lamella has the direction of $(1, \bar{1}, 5) \times (2, 2, 1) = (\bar{1}1, 9, 4)$; the facet projected into $[\bar{1}15]$ in (110) lamella and [221] in $(\bar{1}10)$ lamella has the direction of $(1, \bar{1}, 5) \times (2, 2, 1) = -(9, \bar{1}1, 4)$. And for the sake of easier illustration, those two vectors with high index has been replaced by $(3, \bar{2}, 1)$ and $(\bar{2}, 3, 1)$. Lastly, the facet seen edge on from $(\bar{1}10)$ lamella as [111] has the direction of $(1, 1, 1) \times (\bar{1}, 1, 0) = -(1, 1, \bar{2})$.

Based on the stereology of these TEM observations, we propose a crinkled 3D structure for the tail-to-tail sawtooth domain walls, as schematically shown in Figure 3.14(d). This structure consists of three-faceted peaks, composed of a re-entrant $(11\bar{2})$ facets and two facets with orientations close to $(3\bar{2}1)$ and $(\bar{2}31)$. What is more, having a three-dimensional domain model at hand offers a quite convenience: the calculation of $\boldsymbol{P_s}$ discontinuity at the domain walls becomes straightforward as simple vector multiplication. Let us assume a $\boldsymbol{P_s}$ value of 100 μCcm^{-2} for BFO along the [111] polar axis (see our calculation in Chapter 4). The re-entrant $(11\bar{2})$ walls are parallel to the [111] polar axis and therefore being a neutral domain wall

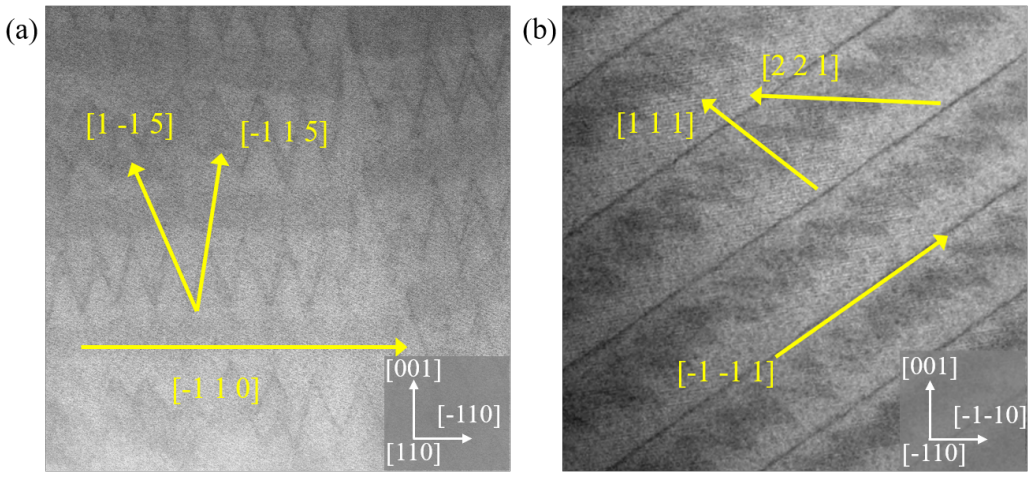

Figure 3.13: STEM BF images of (a) (110) and (b) ($\bar{1}$10) lamella, with crystal orientation and domain wall orientation labelled.

(NDW) and exhibit no $\boldsymbol{P_s}$ discontinuity; the (3$\bar{2}$1) and ($\bar{2}$31) facets are inclined at an angle of approximately 18.0° to [111]. Hence, their local $\boldsymbol{P_s}$ discontinuity can be calculated as $-2 \times P_s \times sin(18.0°)$, which yields approximately -62 μCcm^{-2}, so they are positively charged domain walls (CDWs) with this same charge density magnitude to compensate the polar discontinuity.

While the energy of any given domain wall configuration requires the calculation of short- and long-range electrostatic and polarisation/screening components for all domain wall facets and surrounding material,[122; 123] it is not immediately obvious that a crinkled domain wall that has re-entrant facets (and thus a larger CDW area than a flat domain wall) is the lowest energy configuration. The presence of these facets therefore requires some consideration. Importantly, the 180° ferroelectric domain walls are inherently more flexible than 71° or 109° ferroelectric-ferroelastic domain walls, since the latter have two constraints, i.e. matching of lattice planes to minimise strain[88] and continuity of oxygen octahedral rotations across the domain wall.[124; 125] These constraints favour certain orientations and control the geometry of ferroelastic domain wall configurations. Conversely, both octahedral rotations and lattice strain are unaffected in principle by a change in polarisation magnitude (including reversal), allowing 180° domain walls to take any orientation. The formation of re-entrant facets from an initially flat tail-to-tail (112) CDW may be understood using the principle that the local energy per unit area of a domain wall increases with its charge density, proportional to $\boldsymbol{P_s} \cdot \boldsymbol{n}$, where $\boldsymbol{n}$ is the unit normal. Thus, NDWs have very low energy per unit area, and CDWs have an energy per unit area that increases as $\boldsymbol{n}$ is more parallel to [111] $\boldsymbol{P_s}$. A flat CDW

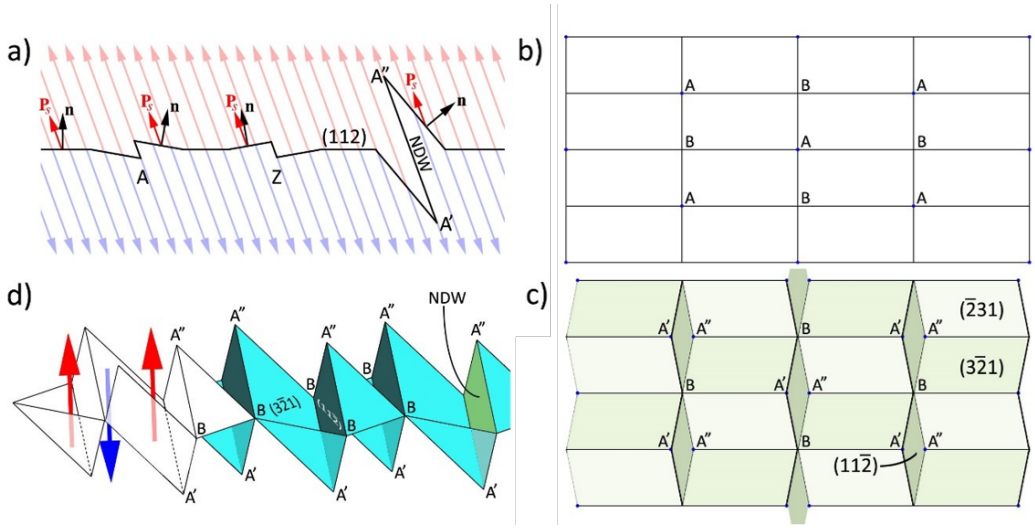

Figure 3.14: Formation and geometry of the crinkled tail-to-tail domain wall. (a) side view of a flat (112) domain wall, which lies at 70.5° to the polar vector $\boldsymbol{P_s}$. An 'up' step A (left) produces a local change in orientation decreasing $\boldsymbol{P_s} \cdot \boldsymbol{n}$, while a 'down' step Z (right) gives a local increase in $\boldsymbol{P_s} \cdot \boldsymbol{n}$ and domain wall energy. Growth of the step A into a NDW facet A'A" results in a re-entrant sawtooth corrugated structure. (b, c) In three dimensions, an array of nodes of instability A on the flat domain wall (seen from above) can develop into a crinkled structure by splitting into vertices A' and A" that bound diamond-shaped re-entrant NDWs. A complementary array of points B lies at junctions between facets. (d) Perspective view of the crinkled domain wall.

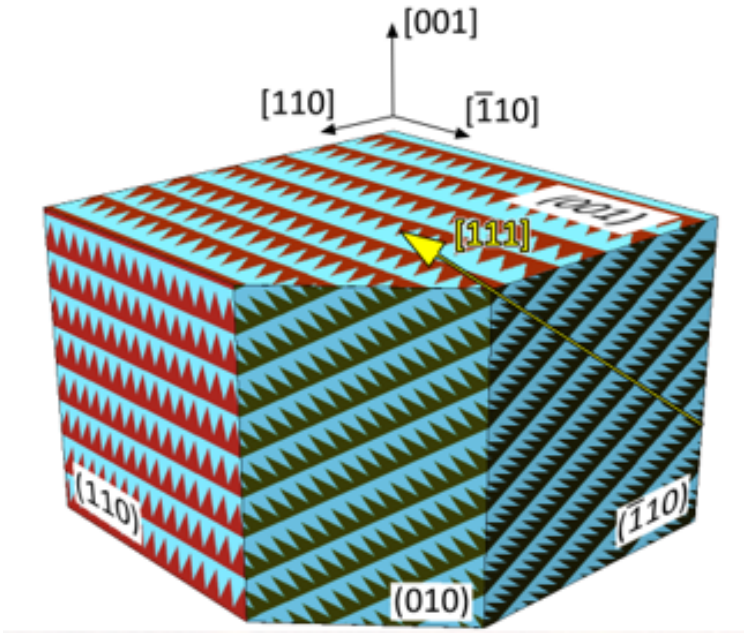

Figure 3.15: Nanoscale domain distribution inside the flux-grown BFO crystal, represented by a cube with crystal orientations labelled.

is unstable if the local reduction in energy, produced by a change in CDW orientation that gives lower $\boldsymbol{P_s} \cdot \boldsymbol{n}$, is larger than the increase in energy arising from the increased domain wall area (that must take place, if the average orientation of the domain wall remains unchanged). To understand how the crinkled surface develops, it is instructive to first consider a corrugated surface consisting of just two facets as shown in Figure 3.14(a). Due to the angle between $\boldsymbol{P_s}$ and the domain wall, an 'up' step A rotates the local domain wall normal away from $\boldsymbol{P_s}$ while a 'down' step Z does the opposite. Therefore, energy is lowered at the A step and there is a driving force for it to expand into a re-entrant NDW facet A'A" . Conversely, local energy is increased at the Z step, which suppresses the formation of non-re-entrant NDW facets. This means that re-entrant facets readily form to reduce local energy-even though a lower total CDW wall area, and perhaps lower total energy, could be achieved with facets that form a surface that is not re-entrant. In three dimensions, further reduction of local energy can be obtained by CDW orientations that further minimise $\boldsymbol{P_s} \cdot \boldsymbol{n}$, i.e. forming peaks rather than corrugations. Such a structure can be obtained from an initial flat CDW by an array of nodes of alternating type, labelled A and B (Figure 3.14(b)). The nodes A act as nucleation sites for NDWs that expand to form diamond-shaped re-entrant NDW facets with vertices A' , B, A" and B as shown in Figure 3.14(b). The 3D shape is illustrated

in Figure 3.14(c) where it can be seen that A' vertices move downwards while A" vertices move up. Although the real structure appears much less regular than the illustration of Figure 3.14(d), this model satisfies the requirement that the domain wall must be continuous and agrees with all the observations. Together with the flat domain walls, a complete scheme of the nanoscale domain structure inside the flux-grown single crystal BFO is shown in Figure 3.15.

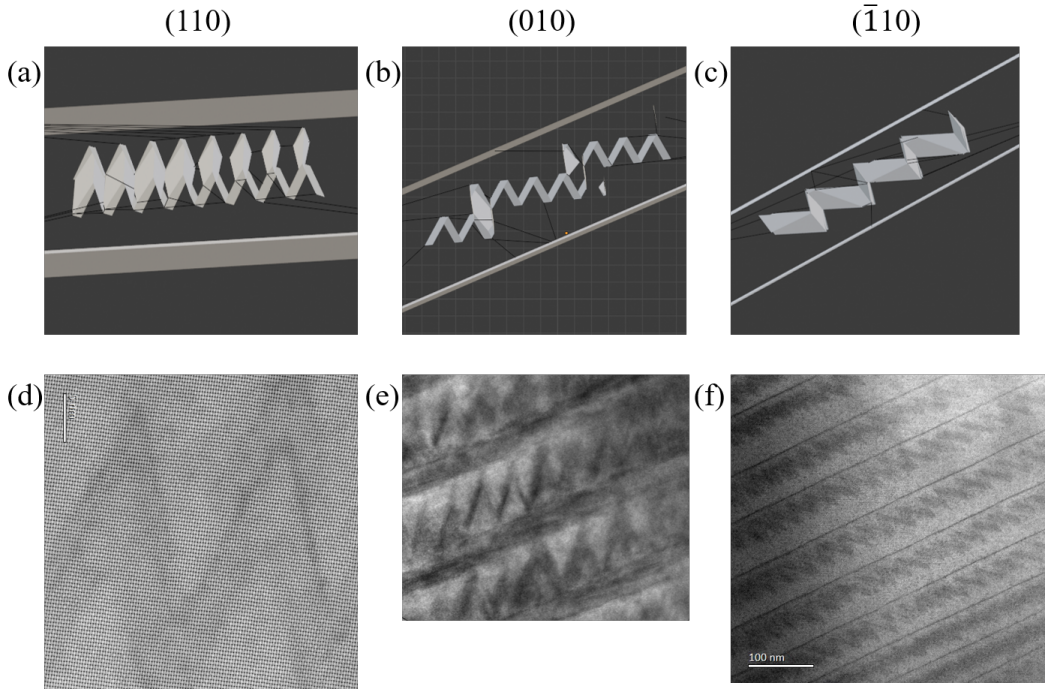

Figure 3.16: (a)-(c) Projections of virtual lamellae prepared in 3D software with orientation planes labelled, compared to (d)-(f) the electron microscopy images of real lamellae.

To further validate our proposal, the 3D model was reproduced in a 3D graphic software, using the same mathematical expressions, which enables us to cut thin cross-sections of the object. By its help, virtual TEM lamellae were prepared (Figure 3.16(a)-(c)) and compared with real-space electron microscopy images (Figure 3.16(d)-(f), as well as Figure 3.10). The comparison reveals a significant agreement between the virtual cross-sections and real space images of thin lamellae, supporting our proposed model.

3.4 Summary and Discussion

In this chapter we have examined the domain structures in the flux-grown single crystal BFO. At the scale of its size, the crystal has four large ferroelastic domains. Within each ferroelastic domain, the crystal has a dense array of flat domain walls running along (112) planes with a spacing between $60-120$ nm, and those flat walls are revealed to have a reconstructed atomic structure than the bulk BFO. Between each pair of flat domain walls, the bulk BFO is divided into two domains with opposite polarity, separated by sawtooth domain walls comprised of three-faceted peaks consisting of a $(11\bar{2})$ NDW and two CDWs with orientations close to $(3\bar{2}1)$ and $(\bar{2}31)$.

Since our work is not the first attempt to explain the domain structure in this crystal, it is necessary to explain why our model is different from the existing literature and where the deviation comes from. Previous investigations of the same batch of flux-grown single-crystals BFO[33; 34; 35] revealed a dense array of parallel domain walls with either sawtooth or flat shape. Hardly any difference could be found by comparing of the electron microscopy and PFM images of earlier works with ours, which is easy to understand because we all look at the same crystal. For example, in Ref.[33] the flat domain walls appear as wide bands in their Fig. 3 but thin lines in Fig. 5, exactly the same as our Figure 3.10. An initial PFM study conducted by Berger et al.[33] denoted the domain walls to be 109° type, while the equivalent option of 180° was excluded due to the high predicted energy of 180° domain walls. A second study conducted by Jia et al.[34] using negative C_s high resolution TEM imaging found a variety of domain wall types including 71°, 109° and 180°. A third study on the same crystal[35] emphasising on the in-situ behaviour, follows the model of Jia and did not give anything new. In this chapter, we have revisited the domain structure in this same batch of crystals from various view-directions. We find that there are only two types of domains in the crystal and all domain walls are 180° type, with the sawtooth domain wall being tail-to-tail and the flat wall head-to-head. The main difficulty experienced in previous work was how to translate the flat bands in the TEM images, and the authors chose to consider them as separate flat domains with finite width, which in return confused their understanding of the sawtooth domain orientation. In our experiment, We overcome the difficulty by using FIB to prepare multiple lamellae, from the same region of crystal, with different orientations. The one perpendicular to $[\bar{1}10]$ zone-axis tells explicitly that the dark bands are atom-thin flat domain walls, which can be projected into wider bands when not seen from an edge-on direction.

Unfortunately, the above mentioned issue persists and will continue to rise whenever one attempts to investigate a three-dimensional object by its planar projection. Similar to solving a Rubik's cube, it is always helpful to check the object from multiple view-directions when planning next steps. However, in the context of electron microscopy studies on the domain structure inside ferroelectrics, it has become customary to determine the orientation of $\boldsymbol{P_s}$ solely based on a single image obtained from either the [100] or [110] view-direction. It might be suitable for PTO or BTO since their tetragonal polar structure only gives up/down $\boldsymbol{P_s}$, but the same approach can not be easily transferred to rhombohedral BFO which has eight possible $\boldsymbol{P_s}$ variations that lie at an inclined angle to the conventional [100] or [110] view-directions. In this chapter, we have demonstrated the drawbacks this approach has and the misleading it gives, and showed what a complicated structure one can end up with by combining simple projections. Additionally, we have proved [$\bar{1}$10] view-direction can potentially be a decent choice for domain determination inside rhombohedral structure from which a full polar shift is going to be projected onto the image plane.

Chapter 4

Polarization mapping at atomic scale

4.1 Introduction

Ferroelectric $\boldsymbol{P_s}$ used to be represented by experimentally measured charge density difference during a polar switch, while the modern theory of ferroelectricity describes it as the intrinsic difference between two/multiple polar states (Section 1.2). The latter model builds the relationship between the macroscopic properties of a material with its microscopic structure and enables the calculation of polarization at atomic scale. Meanwhile, it opens the possibility of studying the ferroelectric properties of the materials that are difficult for conventional electrical measurement, for example, to explain the small measured $\boldsymbol{P_s}$ value of bulk BFO from first principle, or to map the local curling behaviour of $\boldsymbol{P_s}$ vectors,

In the previous chapter, domain structure and orientations of the flux-grown single crystal BFO were established to be 180° types, separated by sawtooth and flat domain walls. In this chapter, we aim to quantitatively calculate the ferroelectric $\boldsymbol{P_s}$ vectors in this crystal and study the $\boldsymbol{P_s}$ transition around the domain walls at atomic scale by the help of aberration-corrected STEM. By calculating the $\boldsymbol{P_s}$ value and visualizing its local distribution, we are trying to answer why it is impossible to measure macroscopic $\boldsymbol{P_s}$ value of this single crystal. To achieve the goal, we will apply the $\boldsymbol{P_s}$ calculation method to the single crystal BFO, and map the $\boldsymbol{P_s}$ transition behaviours at charged and neutral 180° domain walls at atomic scale to determine the their chirality. In order to reduce influence from overlapping projections, images of the domain walls are taken from their perspective edge-on direction. That is $[\bar{1}10]$ for the $(11\bar{2})$ NDW and the (112) flat wall, and [110] for the $(3\bar{2}1)$ and $(\bar{2}32)$ CDWs.

4.2 Sawtooth domain walls

4.2.1 Seen from $[\bar{1}10]$ view-direction

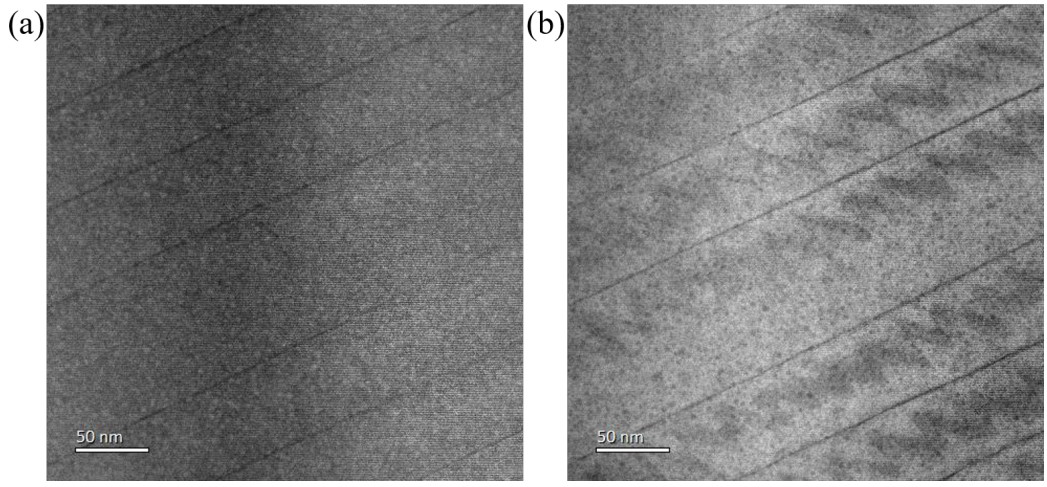

Figure 4.1: Simultaneously collected low magnification STEM (a) ADF and (b) BF image of $(\bar{1}10)$ lamella.

An example of $(11\bar{2})$ NDW is shown in the atomic resolution ADF and BF STEM image of low magnification Figure 4.1 and high magnification Figure 4.2. In the STEM BF image (Figure 4.2(b)), the $(3\bar{2}1)$ and $(\bar{2}31)$ CDWs appear as diffuse darker bands that are nearly parallel to the image plane and perpendicular to the beam direction. In contrast, the $(11\bar{2})$ NDWs are visible as sharp dark lines along the [111] direction, appearing exactly edge-on. The insets of Figure 4.2 show atomic resolution STEM ADF and ABF images of the boxed areas in two opposite domains, where the $-\boldsymbol{\delta_{FB}}$ polar shift and its direction reversal at different domains can be clearly seen. The $a^-a^-a^-$ antiphase tilting of oxygen octahedra is not visible as the view direction $[\bar{1}10]$ is perpendicular to the [111] polar axis, resulting in the oxygen columns appearing as a dumbbell in the same location of every unit cell. The result confirms that $-\boldsymbol{\delta_{FB}}$ reverses direction across the sawtooth domain walls and has roughly the same magnitude of $\sim$ 40 pm in the two domains, in good accordance with the theoretical value of 41 pm.[24] This value yields a $\boldsymbol{P_s}$ value of about 100 μCcm^{-2} when applied to Equation 2.14.

Figure 4.3(a) presents a map of the $-\boldsymbol{\delta_{FB}}$ vector, which is separated into two domains by sawtooth domain walls in the middle and flat domain walls at the corner. The dashed lines in the map were used to extract the magnitude and angle of $-\boldsymbol{\delta_{FB}}$, as shown in Figure 4.3(b). The angle of $-\boldsymbol{\delta_{FB}}$ experiences a sharp reversal

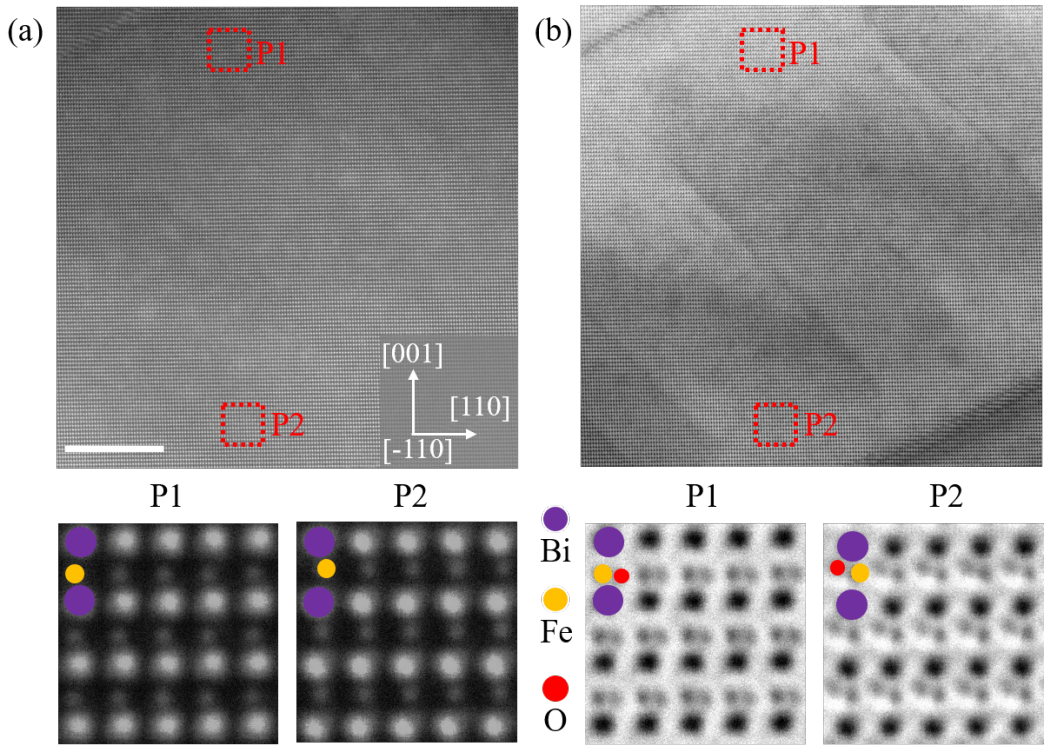

Figure 4.2: Simultaneously collected atomic resolution STEM (a) ADF and (b) BF image of ($\bar{1}10$) lamella, scale bar 10 nm. Insets show atomic resolution STEM ADF and ABF images of the boxed areas in two opposite domains.

of 180° across the sawtooth domain walls, either charged or neutral ones, whereas the change in magnitude is more gradual near the domain walls, only reaching its peak value at the center of the domains. The relationship between the CDW bands in Figures 4.2(b) and 4.3(a) is poor, as they appear diffuse in the BF image but irregular and sharp in the $-\boldsymbol{\delta_{FB}}$ map. The STEM images looks different from the diffraction-contrast TEM image from the same view-direction (Figure 3.6(c)). The diffraction-contrast TEM is sensitive to the local structure variation of the domains (Section 2.x), thus the domain boundaries appear sharp. In the BF-STEM images, according to Condurache et al.[35], the contrast of these domain walls (for example, dark lines in the middle of Figure 4.2(b)) does not follow their movement in the polar map (boundaries in the middle of Figure 4.3(a)) under an applied field, implying that the contrast may be due to an accumulation of oxygen vacancies at the original position of the domain walls. This could be the case here, as the domain walls are viewed in projection through the thickness of the FIB lamella with varying polarization along the electron beam, and as a result the polar map

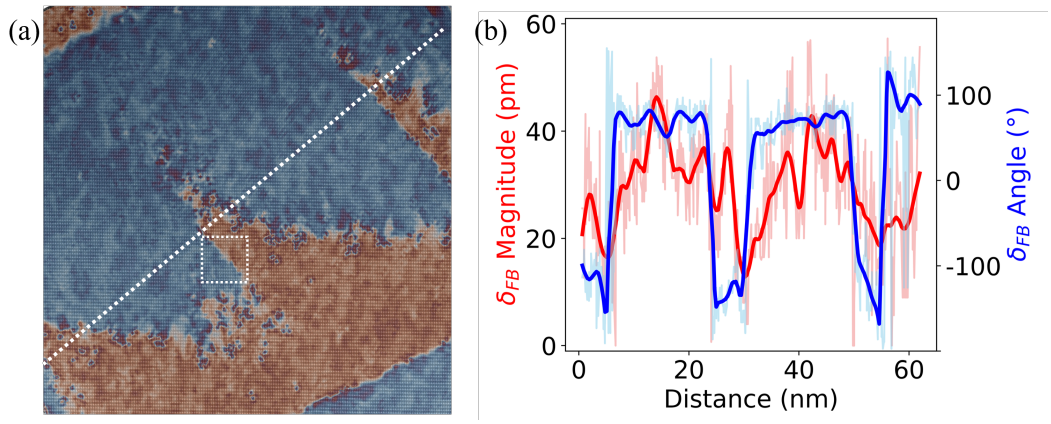

Figure 4.3: (a) Quiver map of $-\boldsymbol{\delta_{FB}}$ vectors of the STEM images in Figure 4.2. (b) Magnitude and angle data of $-\boldsymbol{\delta_{FB}}$ vector extracted at the dashed line.

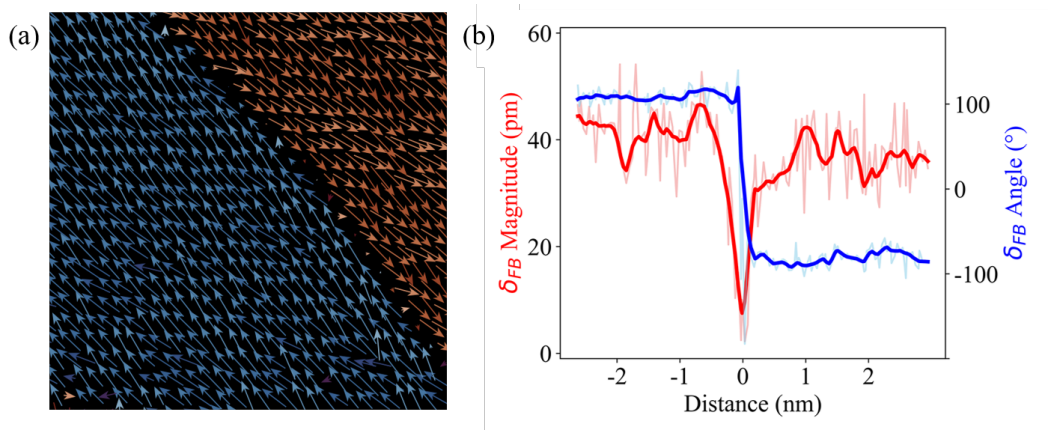

Figure 4.4: (a) Enlarged quiver map of $-\boldsymbol{\delta_{FB}}$ vectors of boxed area Figure 4.3(a), emphasising on a NDW. (b) Magnitude and angle data of $-\boldsymbol{\delta_{FB}}$ vector extracted at the NDW.

could be different from the ideal projection of the 3D model (Figure 3.14 on this view-direction. Therefore, the $-\boldsymbol{\delta_{FB}}$ measurements cannot be considered reliable at the CDWs in this projection, nor provide useful information about the local polar transition.

In comparison, the $(11\bar{2})$ NDW appears sharp and straight in Figure 4.3(a) and is consistent with the dark line in Figure 4.2(b), providing confidence in the validity of $-\boldsymbol{\delta_{FB}}$ measurements. An enlarged quiver plot of the NDW is presented in Figure 4.4(a), where no rotation of $\boldsymbol{P_s}$ noticeable at the wall. Instead, $-\boldsymbol{\delta_{FB}}$ drops to zero for a single unit cell at the wall, indicating that this NDW belongs to the Ising type. Additionally, the magnitude of $\boldsymbol{P_s}$ remains constant up to the domain wall, which is in agreement with predictions that NDWs are typically much

sharper than CDWs.[16; 89; 79; 126] This contrasts with observations of other CDWs in BFO, such as 180°[127] and 71°/109° domain walls[128; 129], as well as the tail-to-tail CDW facets discussed below.

One thing to note here is, careful observation might notice that in the ABF images of Figure 4.2, the exact position of oxygen columns in P1 and P2 is slightly different. It looks like oxygen columns are little further away from Fe in P2. Yet the reason remains unknown to us. Imperfect zone-axis alignment could be one reason, although we tried to correct the zone-axis at our best but kept seeing this difference. Local overlap of domains is plausible, since it is an inevitable problem for TEM sample preparation and we cannot make a lamella that is only one atom layer thick. Or is it the result of the image acquisition or process, for example, scan error or stack alignment? Our single scans, either quick or slow, or by another microscope where the EELS data in Chapter 5 was taken, have repeated this finding. During dozens of STEM session within the duration of this thesis, with no intention to repeat on a particular sample/imaging area or stick to a particular set-up, the structure difference has always been there as long as oxygen is visible (for example Figure 4.13), and we are confident that it is above instrumental or random error. Is it possible that an internal electrical field is pushing one domain towards another meta-stable state? But our 4D-STEM attempts found no shift of electron beam at the two domains, meaning no detectable electrical field. We are more inclined to doubt that there is an intrinsic change of the local structure, such as a monoclinic distortion, in the two domains. It is not intuitive because we tend to picture opposite ferroelectric domains merely as an inversion of polar displacement since they represent equivalent states in the energy profile (Figure 1.1), and no existing theory/model/observation suggests an additional structural distortion will be involved during $\boldsymbol{P_s}$ switch. Further investigation would be necessary to determine whether any of these possibilities is correct.

4.2.2 Seen from [110] view direction

The orientation of the $(3\bar{2}1)$ and $(\bar{2}31)$ CDW facets means that no low-index zone axis is available that would allow them to be imaged at atomic resolution and edge-on. Nevertheless, by selecting the thinnest part of the sample, projection effects can be minimized, and a reliable measurement of $-\boldsymbol{\delta_{FB}}$ at the unit cell level can be obtained. This is demonstrated in low magnification Figure 4.5 and high magnification Figure 4.6, where the CDWs are inclined at an angle of only 10° from the point of view in a (110) lamella. The $(11\bar{2})$ NDW facets lie at 20° to the plane of section in this projection, and their presence in the TEM lamella could lead to unreliable

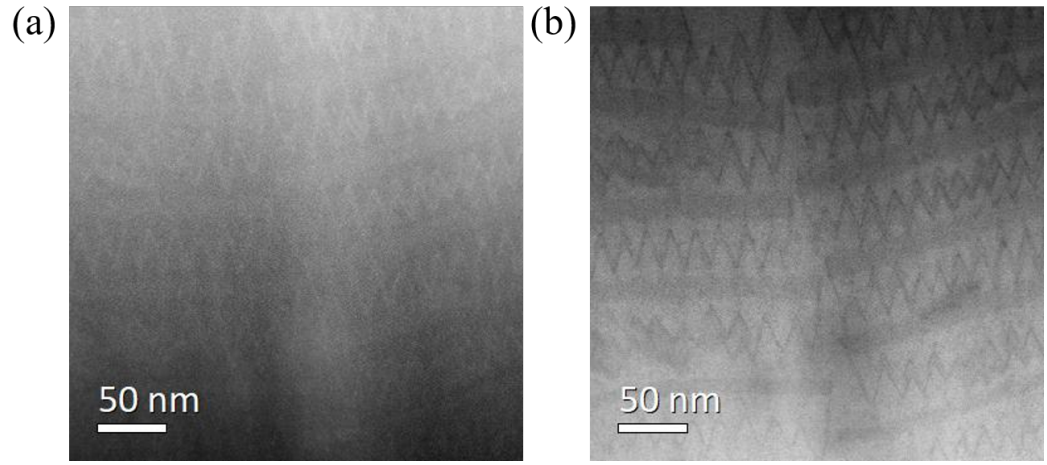

Figure 4.5: Simultaneously collected low magnification STEM (a) ADF and (b) BF image of (110) lamella.

results due to a 180° change of polarisation at some point in the specimen. However, since the distance between NDW facets is $\sim$ 40 nm, and the estimated specimen thickness is $\sim$ 7 nm, it is unlikely that they are captured in the region of Figure 4.6, and the $\boldsymbol{P_s}$ should not change significantly through the specimen thickness.

The results are further supported by the coincidence between the domain wall location in the BF image Figure 4.6(b) and $-\boldsymbol{\delta_{FB}}$ map Figure 4.7(a). The average value of $-\boldsymbol{\delta_{FB}}$ away from the domain wall is $\sim$ 23 pm, which is expected for this (110) projection, and the component of $\sim$ 34 pm parallel to the electron beam is not observed. The ABF images reveal $a^-a^-a^-$ antiphase tilting of oxygen octahedra, as evidenced by the curvature of O-Fe-O-Fe-O chains (Figure 4.6(b) insets). The 23 pm in this view direction corresponds to $\sim$ 40 pm shift along [111] polar axis, equals to 100 μCcm^{-2} according to Equation 2.14.

Figure 4.8(a) show enlarged parts of the quiver plot on the sidewalls (boxed areas in Figure 4.7(a)). When crossing the domain wall from the yellow region ($\boldsymbol{P_s}$ down) to the blue region ($\boldsymbol{P_s}$ up), $\boldsymbol{P_s}$ is observed to rotate clockwise (Figure 4.8(a1)) or anticlockwise (Figure 4.8(a2)). In contrast to the NDW facets in Figure 4.4(a), this Néel-type rotation occurs over a width of nearly 2 nm. Additionally, there is a reduction in the magnitude of $\boldsymbol{P_s}$ over the same width, dropping almost to zero at the domain wall center (Figure 4.8(b)). Even though the $\boldsymbol{P_s}$ component parallel to the point of view is not seen, this reduction indicates that the domain walls also has Ising- and/or Bloch-type character, with a reduced magnitude and/or rotation of $\boldsymbol{P_s}$ to lie along [110]. This is perhaps to be expected since the mixed Néel/Bloch/Ising-type of CDWs in ferroic materials is well established,[93; 94] and both 71° and 109°

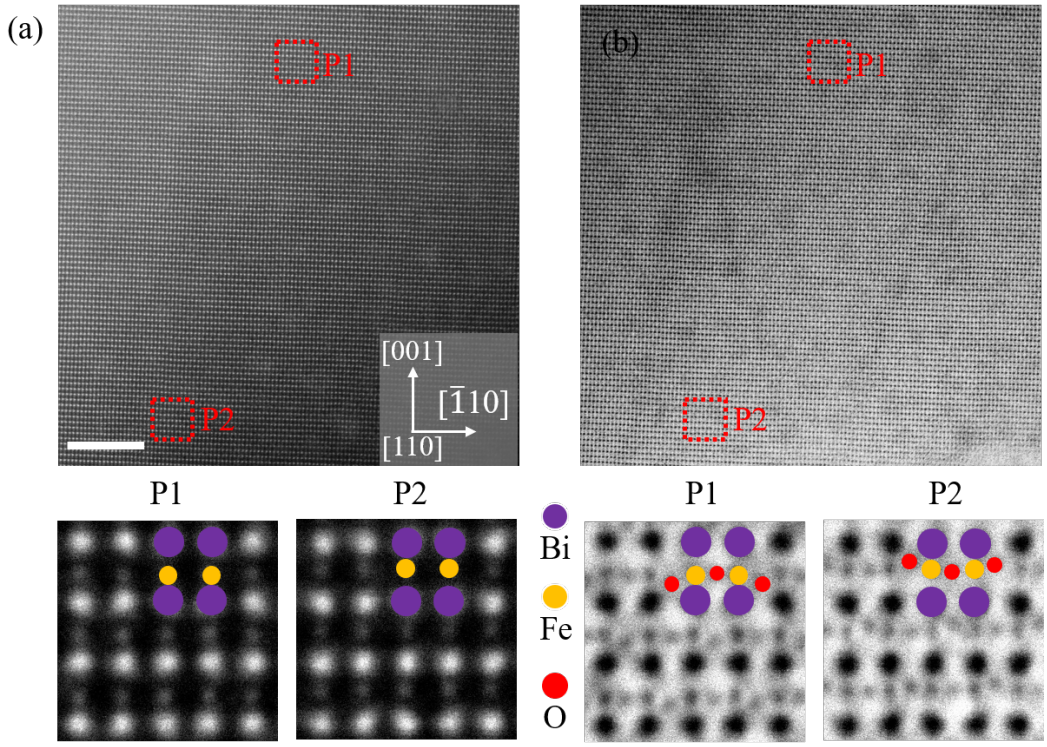

Figure 4.6: Simultaneously collected atomic resolution STEM (a) ADF and (b) BF image of (110) lamellae, scale bar 10 nm. Insets show atomic resolution STEM ADF and ABF images of the boxed areas in two opposite domains.

CDWs in thin-film BFO have been confirmed to have a chiral nature.[130]

Finally, tilting angle of the oxygen octahedra has also been mapped (Figure 4.9) around a sawtooth domain wall (boxed area 2 in Figure 4.7(a)). There is an evident fluctuation of the tilting angle in the map, while at the domain wall itself, it is easier to find 'extreme' values either much lower or higher than the bulk value (in the map it is represented as black/yellow contrast to the red background), similar to the result of Ref.[34].

4.2.3 Seen from [010] view-direction

An example of (010) FIB lamella is shown in the atomic resolution ADF and BF STEM image of Figure 4.10. From this view direction, both NDWs and CDWs are inclined to the view direction, and the overlap effect makes the $-\boldsymbol{\delta_{FB}}$ measurements less reliable at the domain walls in this projection. However, as discussed in the thin film sample, when seen from this view-direction, Fe atom stays in a more 'spacious' Bi unit cell compared to the former two view directions, and it stays further from

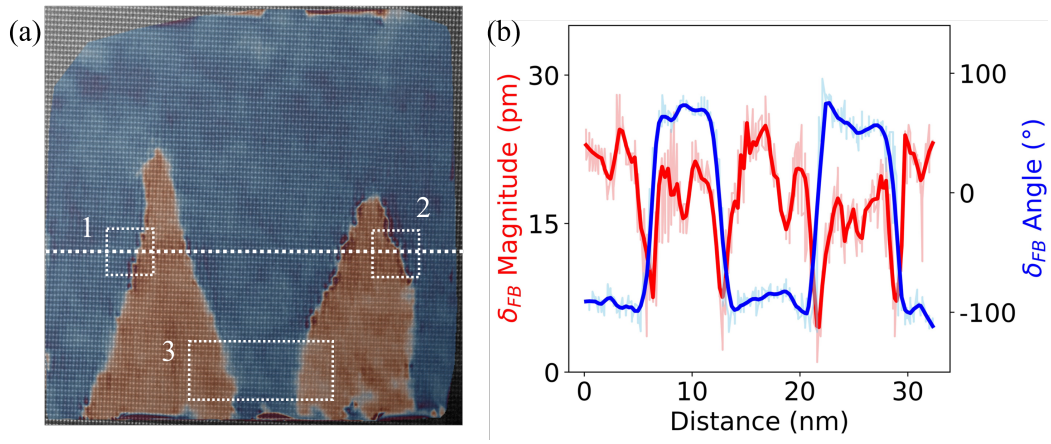

Figure 4.7: (a) Quiver map of $-\boldsymbol{\delta_{FB}}$ vectors of the STEM images in Figure 4.6. (b) Magnitude and angle data of $-\boldsymbol{\delta_{FB}}$ vector extracted at the dashed white line in the middle of (a).

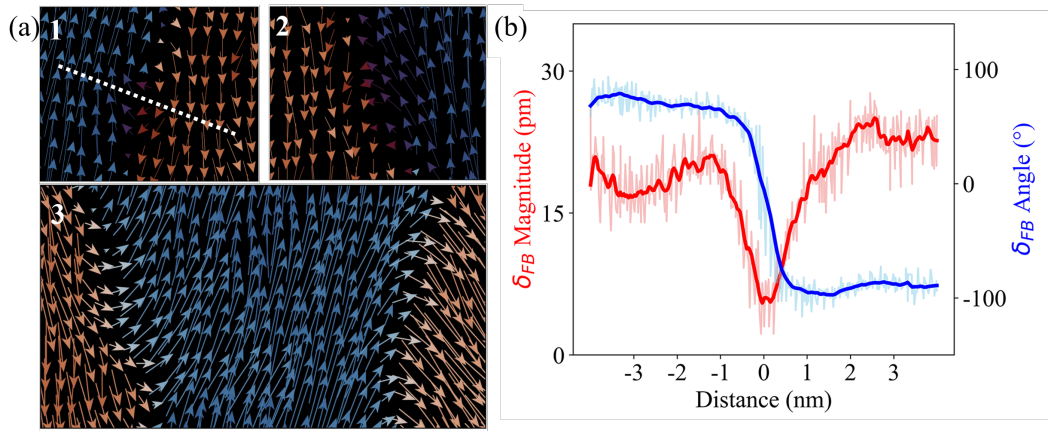

Figure 4.8: (a) Enlarged quiver map of $-\boldsymbol{\delta_{FB}}$ vectors of boxed area Figure 4.7(a), emphasising on the $\boldsymbol{P_s}$ transition behaviour at the domain wall. (b) Magnitude and angle data of $-\boldsymbol{\delta_{FB}}$ vector extracted from the dashed line in (a1).

its nearest Bi atom, which makes this view direction ideal for $\boldsymbol{P_s}$ mapping at large area.

In the BF image Figure 4.10(b), either the $(3\bar{2}1)$ or $(\bar{2}31)$ CDWs, the $(11\bar{2})$ NDWs, or the (112) flat domain walls appear as diffuse darker bands, not the sharp lines when seen from their perspective edge-on direction. The insets of Figure Figure 4.10 show atomic resolution STEM ADF and ABF images of the boxed areas in two opposite domains, where the $-\boldsymbol{\delta_{FB}}$ polar shift and its direction reversal at different domains can be clearly seen. The result confirms that $-\boldsymbol{\delta_{FB}}$ reverses direction across the sawtooth domain walls and has roughly the same magnitude of ~ 33 pm in the two domains, in good accordance with the theoretical value of 41 pm along

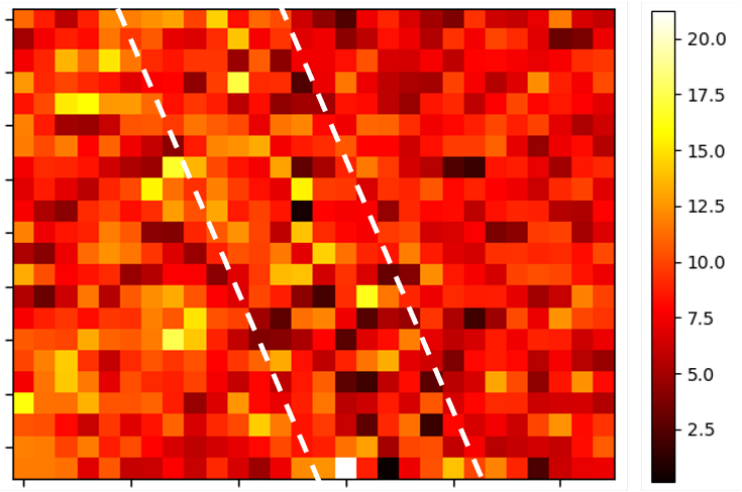

Figure 4.9: Tilting angle of oxygen octahedra of the boxed area 2 in Figure 4.7(a). Between the white dash line is the position of the sawtooth domain wall.

[111] direction.[24] This value yields a $\boldsymbol{P_s}$ value of about 100 μCcm^{-2} when applied to Equation 2.14.

The domain wall location in the BF image Figure 4.10(b) and $-\boldsymbol{\delta_{FB}}$ map Figure 4.11(a) do not align well with each other, as easily noticed that domain walls in the BF image are sharper. Figure 4.12 shows enlarged part of the quiver plot on the sidewalls (boxed areas in Figure 4.11(a)), where curling of the polar vectors can be found at the wall. However, because the overlap effect makes the $-\boldsymbol{\delta_{FB}}$ measurements less reliable at the domain walls in this projection, we are not going to analysis more on this projection.

4.3 Flat domain walls

Figure 4.13 displays atomic resolution STEM images of one of the flat domain walls, captured from the edge-on [$\bar{1}$10] view-direction in the thinnest region of the specimen. In the bulk domain region, the atomic arrangement conforms to the ideal ($\bar{1}$10) configuration (shown as inset), where the oxygen dumbbell columns appear at the same position within each unit cell. However, Figure 4.13 clearly reveals that the local structure of these flat domain walls deviates from the BFO bulk arrangement, which is illustrated in Figure 4.14(a). Examining the (001) planes formed by the bright Bi atom columns, which appear horizontally in Figure 4.13, it is noticeable that downward displacements (i.e., along [00$\bar{1}$]) are observed on the left side, starting $\sim$ 0.5 nm away from the domain wall. Conversely, upward displacements along

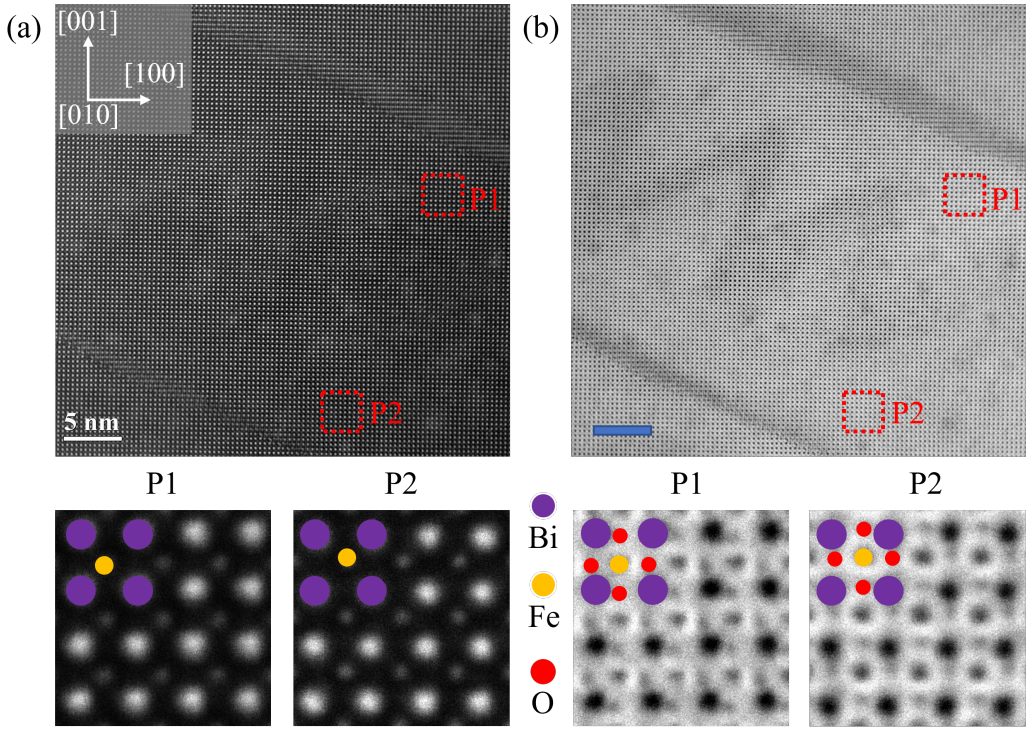

Figure 4.10: Simultaneously collected STEM ADF(a) and BF(b) image of (010) lamellae, scale bar 5 nm. Insets show atomic resolution STEM ADF and ABF images of the boxed areas in two opposite domains.

[001] are observed on the right side. These displacements reach a magnitude of ~ 0.1 nm at the domain wall itself. Further away from the boundary, the (001) planes become fully aligned, as evident from Figure 4.14(a) and the horizontal white lines in Figure 4.13. However, the vertical (110) planes do not align perfectly, exhibiting a lateral shift of 0.1 nm, approximately halfway between the [110] direction. Moreover, Figure 4.14(a) reveals a slight increase in the displacement of the (110) planes immediately adjacent to the boundary, which may not be readily noticeable in the STEM images.

The overlaid quiver map of $-\boldsymbol{\delta_{FB}}$ vectors on the ADF STEM image of Figure 4.13(b) shows that polarisation changes by 180°, pointing towards the wall on both sides. At the domain wall itself, $-\boldsymbol{\delta_{FB}}$ is not calculated because it is unclear how to define the unit cell. Away from the domain wall, the magnitude of $-\boldsymbol{\delta_{FB}}$ is generally $\sim$ 40 pm, in good agreement with the theoretical value of 41 pm for $\boldsymbol{P_s}$ of $\sim$ 100 μCcm^{-2}, as discussed above. The average value of $\boldsymbol{P_s}$ changes its sign abruptly (over $\sim$ 1 nm) at the wall (Figure 4.14(b), which is very different to the thicker ($>$ 2 nm) widths reported previously for CDWs in BFO without any local

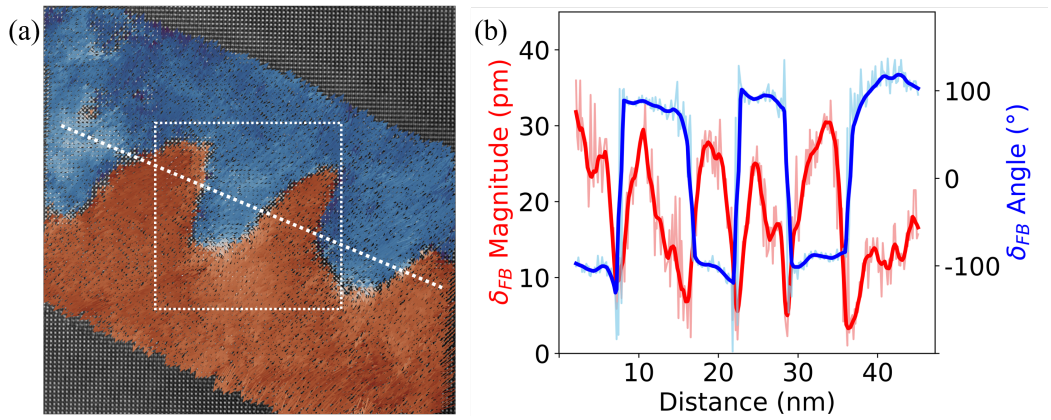

Figure 4.11: (a) Quiver map of $-\boldsymbol{\delta_{FB}}$ vectors of the STEM images in Figure 4.10. (b) Magnitude and angle data of $-\boldsymbol{\delta_{FB}}$ vector extracted at the dashed white line in the middle of (a).

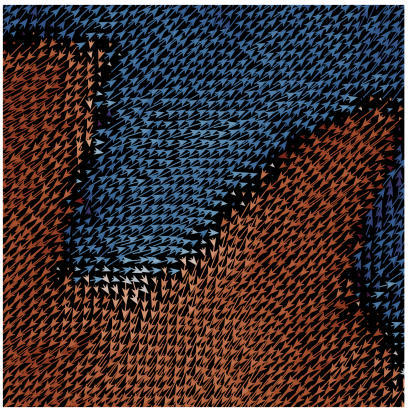

Figure 4.12: Enlarged quiver map of $-\boldsymbol{\delta_{FB}}$ vectors of boxed area Figure 4.11(a), emphasising on the $\boldsymbol{P_s}$ transition behaviour at the domain wall.

reconstruction.[127; 128; 129] As discussed in Section 3.3.4, this abrupt sign change results in ~ 188 μCcm^{-2} $\boldsymbol{P_s}$ discontinuity at the narrow domain wall, indicates the presence of a strong electrical field related to the local change in structure at the domain wall.

Figure 4.15(a) presents an image of the flat domain wall within the (010) lamella. Despite the inclination of the domain wall with respect to the beam direction, this image is captured at the thinnest portion of the lamella, and the use of a high electron collection angle results in a reduced depth of field[131]. As a result, the domain wall appears sharply defined. In this projection, the domain wall has a width of approximately 1.5 unit cells and extends along the $[\bar{2}01]$ direction. Although it may appear different from the $(\bar{1}10)$ projections in Figure 4.13, it is, in

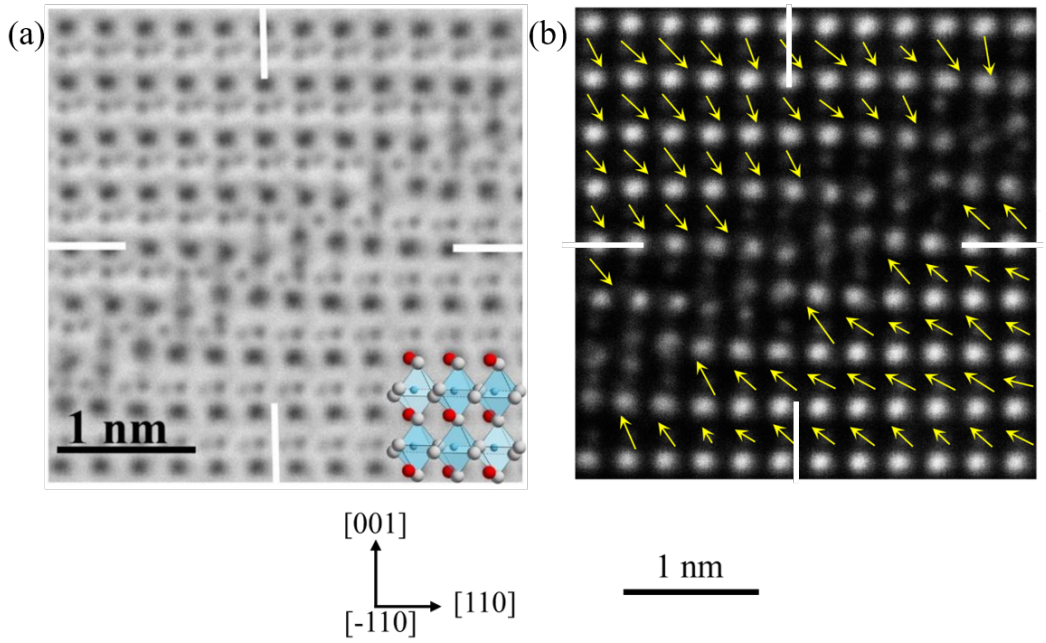

Figure 4.13: Simultaneously collected (a) STEM ABF and (b) ADF image of the flat wall seen from [$\bar{1}$10] view direction, with the quiver map of $-\boldsymbol{\delta_{FB}}$ vector overlaid on the ADF image. Overlaid inset of (a) is the ideal ($\bar{1}$10) projection of BFO (Bi is red, Fe is blue, and O is grey). White lines in both images represent (110) planes which are vertical in the image, and (001) planes which are horizontal.

fact, the same structure because the half unit cell rigid body shift is also observable here. In Figure 4.15(a), the (001) planes are fully aligned, as indicated by the horizontal white lines, while a vertical white line denotes a ½[100] displacement. Since the component along the beam direction is not visible, this observation is consistent with the ½[110] rigid body shift observed in Figure 4.13. At the domain wall itself, alternating clusters of bright and dark atoms can be observed, forming either 2×1 or 2×2 atom blocks. Detailed investigations of these clusters, including their chemical compositions, are explored in Chapter 5. Figure 4.15(b) is the quiver map of the ADF image, showing clearly the antiparallel head-to-head $\boldsymbol{P_s}$ configuration in vicinity of the flat wall.

The flat wall when viewed from the [110] perspective (Figure 4.16) exhibits no evident distinction from the bulk structure. It appears as a dark contrast where it resides in the middle of the image, but it maintains the same atomic arrangement as the bulk. And it is very likely the same structure shown in the Fig. 4 of Ref[34]. The ½[110] rigid body shift is not observable because it is parallel to the view direction, and no other body shift can be found. Overall, our observation of the flat

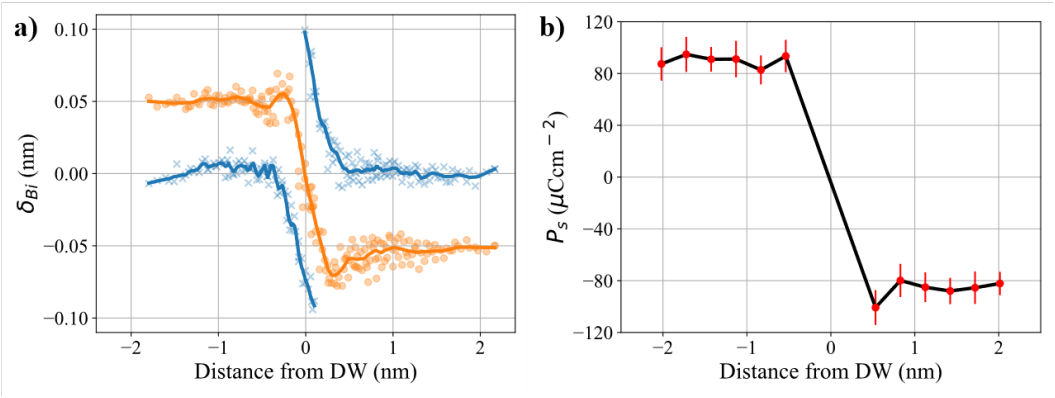

Figure 4.14: (a) Distortion of unit cells in the vicinity of the domain wall of Figure 4.13, measured by the displacement of Bi atom (δ_{Bi}) columns away from (110) planes (orange) or (001) planes (blue). Points correspond to individual measurements and solid lines are an average value. (b) Average $\boldsymbol{P_s}$ value from the $-\boldsymbol{\delta_{FB}}$ vectors, measured in bands parallel to the domain wall in Figure 4.13(b)

wall at atomic scale from various view-directions shows a local reconstructed atom arrangement with a ½[110] rigid body shift across the flat domain walls.

4.4 Summary and Discussion

In this chapter, atomic scale $\boldsymbol{P_s}$ mapping and quantification of single crystal PTO, thin film BFO and flux-grown single crystal BFO has been presented. In particular, the 180° tail-to-tail sawtooth domain walls in the single crystal BFO was revealed to have different $\boldsymbol{P_s}$ transition behaviour, with the $(11\bar{2})$ NDW facets being Ising-type wall and the $(3\bar{2}1)$ and $(\bar{2}32)$ CDWs facets being mixed Néel/Bloch/Ising-type.

It is not a novel observation that reported $\boldsymbol{P_s}$ value in some BFO crystals[23] could be one magnitude smaller than measurements in thin films[15; 38], single crystals[31] or ceramics[30]. When we tried to measure the macroscopic $\boldsymbol{P_s}$ hysteresis loop, one of the most important characteristics of ferroelectrics, there was little signal from the crystal, and we occasionally observed strong resistance behaviour, i.e. explosion of the crystal. However, at atomic scale our calculated $-\boldsymbol{\delta_{FB}}$ vectors are nearly the same as thin films[129; 38], equivalent to $\boldsymbol{P_s}$ 100 μCcm^{-2}. Now consider the flat domain walls' atomic reconstruction revealed by our results, it is natural to relate them to planar defects/dislocations rather than proper domain walls which can be repeatedly written or erased (see Chapter 1). Those reconstructed structures serve as pinning centres, and pushing them to move by external forces would be less probable if that involves the reconstruction of neighbouring bulk material (we have

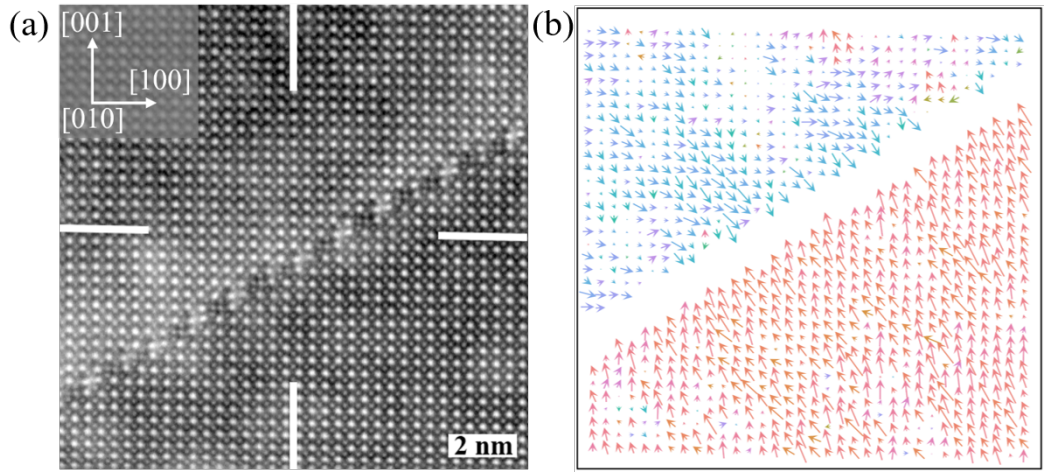

Figure 4.15: (a) STEM ADF image of the flat domain wall seen from [010] view direction. (b) STEM BF image of the flat domain wall seen from [110] view direction, where the flat domain wall is boxed by red dashed lines. [Maybe change (b) to yellow arrows only]

tried to PFM switch this sample using 200 V stimulus but still found no change, taking into consideration the unproportionally low volume ratio of the flat domain wall compared to bulk material, presented in Figure 4.2,). So, if we were strict with terminology, it is not suitable to call these reconstructed bands a 'domain wall' because it hardly fits the standard. Instead, a more general term 'domain boundary' might be better to express the fact that it separates two domains but is not part of the bulk material (although they will continue to be referred as 'flat domain walls' throughout this thesis to reduce confusion). Their stiff nature could explain why we failed to measure useful $\boldsymbol{P_s}$ value at bulk scale, although at atomic scale our calculation predicts a high $\boldsymbol{P_s}$ value close to the reported values[31; 30; 15]. On the contrary, the sawtooth domain walls, in every aspect, are proper domain wall- they are embedded within bulk BFO materials, showing local $\boldsymbol{P_s}$ transition, and although it is not easy they are reported to be moved by an applied external field.[34; 35] The sawtooth domain walls have $(11\bar{2})$ planes that contain the $\boldsymbol{P_s}$ vectors, reducing polarisation discontinuity to lowest and thus lower the system energy, and again pinned the domain structure within the rest of the crystal.

A final point to discuss is the formation mechanism of the domain structure in this BFO crystal. Looking back again at the 3D model in Figure 3.14(b), the inner structure of the flux-grown single crystal BFO can be seen as layers of bulk materials stacked perpendicular to [112] direction and adjacent layers are separated by the flat domain walls. Those layers have a quasi-2D shape with 50-100 nm thickness

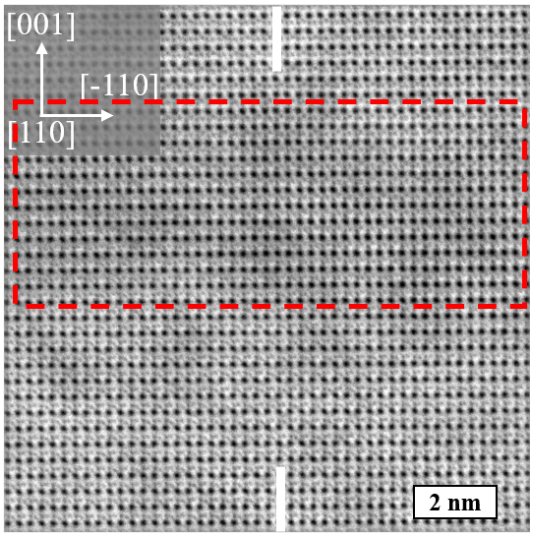

Figure 4.16: STEM BF image of the flat domain wall seen from [110] view direction, where the flat domain wall is boxed by red dashed lines.

but much larger length and width, and because their boundaries are immobile, everything inside the layer will be restrained within its finite thickness. Thus, it is natural to consider those (112) layers as the building block of this crystal, or say the minimum repeating unit. This multi-layer structure closely parallels the superlattice structure, and we call it 'intrinsic multilayer' structure of the flux-grown BFO single crystal. Then what is the boundary condition of each layer within this crystal? Our findings indicate that at the interface between two adjacent (112) layers, a highly negatively charged boundary exists, that is the flat domain walls. This charged boundary does not behave like an insulator expelling the incoming $\boldsymbol{P_s}$ vector, as observed in the work of Yadav et al.[84]; neither does it passively compensate the $\boldsymbol{P_s}$ bounding charge like a conductor, as demonstrated by Rusu et al.[85] Instead, the negatively charged boundary in our crystal dictates $\boldsymbol{P_s}$ vectors point towards it from both sides and pins the local $\boldsymbol{P_s}$, which is so strong that no $\boldsymbol{P_s}$ transition/curling/bending behaviour can be found in their vicinity; getting further from the flat walls into the middle of (112) layers, the pinning force relaxes since electrostatic Coulomb force is inversely proportional to the square of distance, rising the likelihood of polar transitions and leading to the formation of sawtooth walls as the result of local energy competition.

Theoretical simulations have predicted the formation of a sawtooth domain structure under this particular scenario in the last paragraph. Zhang et al.[123] assumed the presence of electric dipoles with opposite orientations in the system and

employed a Monte-Carlo simulation to determine the equilibrium morphology of the domain walls in between. The system exhibited reproducible formation of sawtooth domain walls as a result of the competition between long-range Coulomb energy from bound charges and short-range interaction energy. A separate work by Marton et al.[132] investigated a defect-modulated ferroelectric structure by shell-model and phase-field simulation. They constructed a broad cell with randomly distributed positive charges, and in its middle lies a narrow region with negative charges (this narrow region can be related to our flat domain walls). Later, they observed the development of charged 180° tail-to-tail domain walls within the layer, systematically adopting a zigzag profile, and demonstrated that this pattern remained stable even when varying the distribution of compensating charges, including point defect charges of different magnitudes and homogeneous charge distributions. According to their argument, the zigzag shape and formation of triangular domains arise as a consequence of the energetic requirement to compensate for the charged layer through polarization gradients while avoiding the paraelectric state and minimizing the surface area of the wall. They propose that polarization rotation, which we identify as an efficient mechanism for distributing the uncompensated polarization bound charge over the domain walls, plays a crucial role in achieving the desired energetic efficiency.

An apparent inadequacy here is we assumed the flat domain walls' existence prior to the sawtooth domain walls', which aligns with the presumption of both simulation works[123; 132]. And it is easy to find the other way around faces the same dilemma. To solve this chicken-egg scenario needs a comprehensive design of experiment to achieve in-depth understanding of the crystal growth and how it influence the final domain structure. Unfortunately, due to the limited time-frame this question is not covered in this thesis.

Chapter 5

EELS study of the flat domain walls

5.1 Introduction

In the previous chapter, it has been demonstrated that the flat domain walls have a reconstructed atomic arrangement that is different to bulk BFO. These walls contain alternating bright and dark clusters, and are very thin and highly charged. Several questions naturally rise about this unique structure: what are those bright and dark clusters, are they another phase of BFO or some impurities? How is the large $\boldsymbol{P_s}$ discontinuity compensated? How will this reconstructed structure influence the bonding of neighbouring bulk material? With these questions in mind, in this chapter, the chemical structure of the flat domain walls is investigated by high spatial and energy resolution electron energy loss spectrum to gain a clearer knowledge of its configuration. We will begin with low loss data to investigate the bandgap structure of the flat domain wall, then move to its elemental distribution mapping to reveal its chemical and structural difference with bulk BFO unit cell, and finally turning into the fine ELNES analysis of possible change of O-K and Fe-L bonding structure.

5.2 Low loss and bandgap

The bandgap value, the energy difference between the top of the valence band and the bottom of the conduction band, could be estimated by fitting the first rising edge of the low loss region and then calculating its intersection with the background baseline (Figure 5.1).[133; 134] This linear fitting is a simplistic approach yet it is quick and considerably reliable.[133]

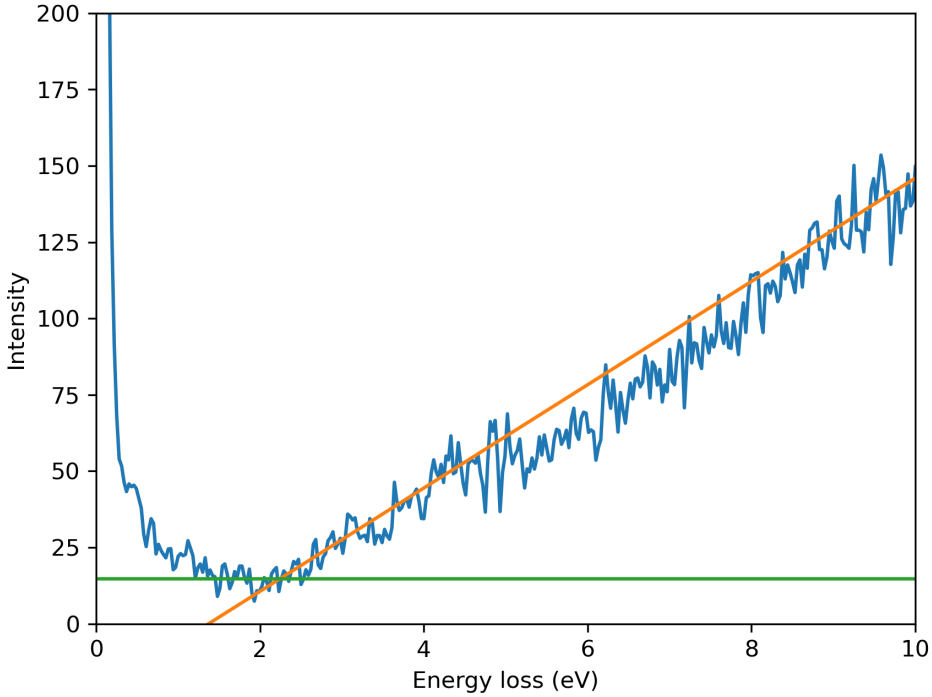

Figure 5.1: Calculation of the bandgap based on low loss EELS data. The horizontal green line shows the fitted background baseline based on raw data of energy range of $1.5 - 2.0$ eV, while the inclined orange line shows the fitted rising edge based on the raw data of $2.1 - 4.1$ eV. Where the two lines intersects on the energy loss axis is the estimated value of bandgap. Influence from thickness variation was reduced by rescale each pixel of the dataset to have a uniform maximum zero-loss peak height.

A HAADF image of the flat domain wall, seen from the edge-on $[\bar{1}10]$ view-direction and collected simultaneously with the low loss EELS, is shown in Figure 5.2(a). Compared to ADF images in Figure 4.10(a), more contamination-like features can be found in the bulk domain area in the HAADF image, due to the change of imaging condition such as accelerating voltage and collection angle.[131] Anyhow, the same reconstructed structure of the flat wall, alternating bright and dark clusters, stands out in the middle of the image. Although in a rather noisy background, there is a faint dark line in the bandgap map (Figure 5.2(b)) at the same position of the flat wall in the HAADF image, where the dark contrast corresponds to an increase of the bandgap value. Scatter values of the selected area in the bandgap map is plotted in Figure 5.2(c). Again, we noticed a slight increase around $x = 10.0$ nm against the noisy background at the same position of the flat wall, which becomes

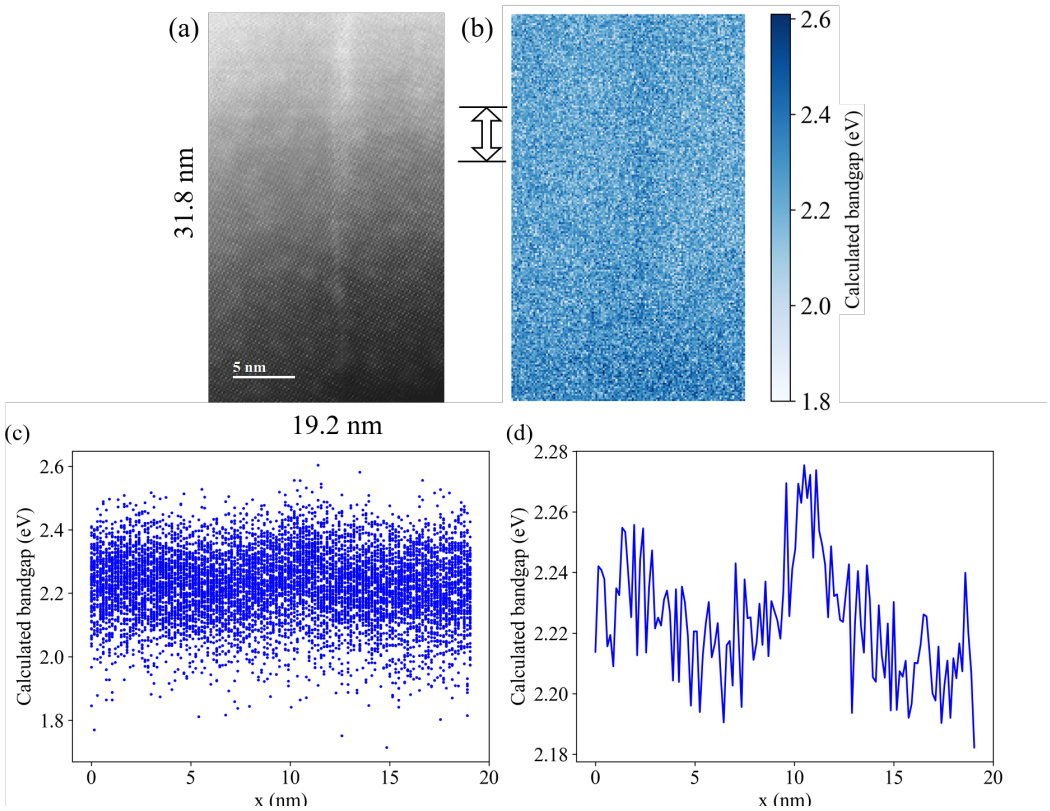

Figure 5.2: (a) HAADF and (b) calculated bandgap map of the flat domain wall seen from [$\bar{1}$10] view-direction. (c) Scatter plot of the bandgap value and (d) their average, extracted from the labelled range in (b).

more obvious after averaging (Figure 5.2(d)). From the [$\bar{1}$10] view-direction, our data shows an average bandgap of 2.21 eV of the bulk BFO, lower than the reported 2.3 to 2.8 eV (Section 1.2.5). The flat wall has a slightly higher bandgap of 2.28 eV, $\sim$ 3.1% increase compared to the bulk value.

Low loss EELS of the flat wall was also collected from the [010] view-direction (Figure 5.3), where inclination of the wall to the view-direction makes it less countable but still informative. Once again, the reconstructed flat domain wall stands out in the middle of the HAADF image (Figure 5.2(a)), and at the same position there is a dark linear feature in the bandgap map (Figure 5.3(b)), corresponding to the increase at $x = 7.5$ nm in calculated bandgap data (Figure 5.3(c)) and their average (Figure 5.3(d)). From [010] view-direction, our data shows an average bandgap of 2.08 eV of the bulk BFO, even lower than the value from [$\bar{1}$10] view-direction. The data confirms a slightly higher bandgap of 2.12 eV at the flat domain walls, $\sim$ 1.9% increase compared to the bulk value.

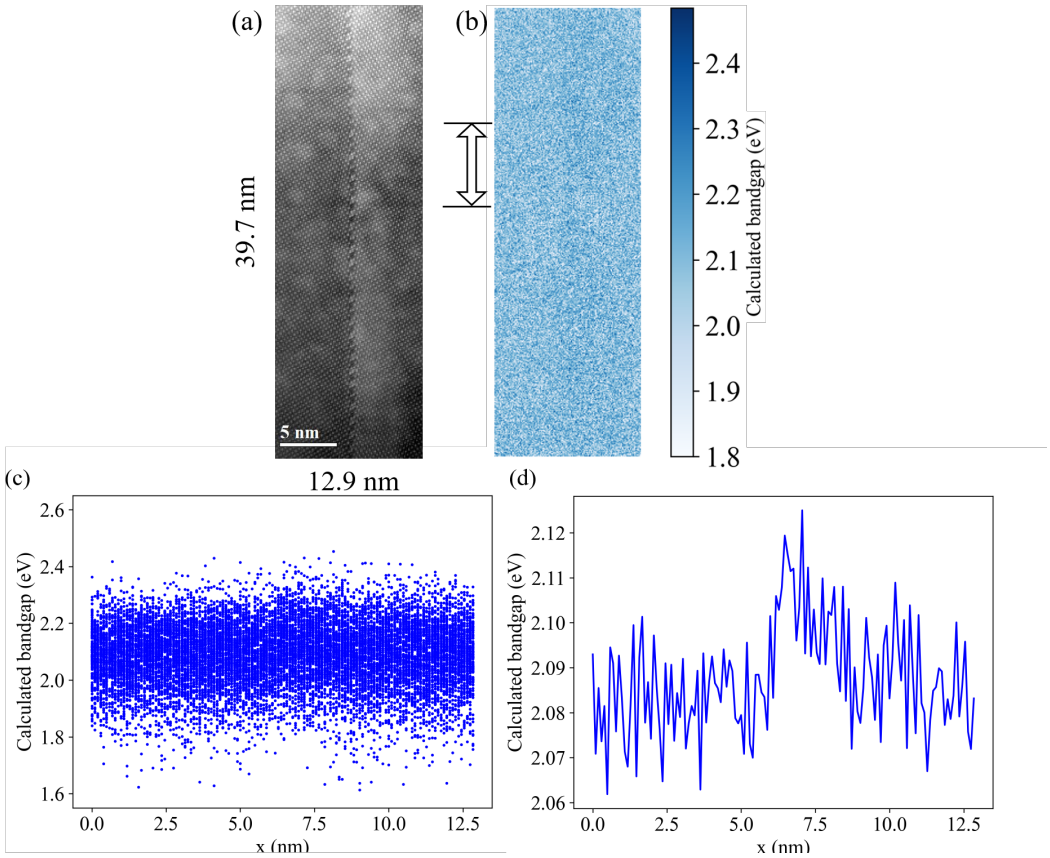

Figure 5.3: (a) HAADF and (b) calculated bandgap map of the flat domain wall seen from [010] view-direction. (c) Scatter plot of the bandgap value and (d) their average, extracted from the labelled range in (b).

5.3 Element map of the flat domain wall

The energy onset edge of Bi ($\sim$ 2600 eV) is a lot higher than O ($\sim$ 530 eV) and/or Fe ($\sim$ 710 eV) meaning that they cannot all fit into one single scan. Therefore, two different sets of simultaneously collected HAADF STEM image and EELS spectrum were recorded, almost at the same position, covering just the Bi spectral range (Figure 5.4) and O plus Fe range respectively (Figure 5.5). Figure 5.4(a) shows an atomic resolution image of a flat domain wall, taken parallel to the wall along the [010] view-direction. Features in Bi element map (Figure 5.4(b)) coincide with the large and bright dots in the Z-contrast HAADF image, indicating that those bright dots are Bi columns that forms either 2×2 or 2×1 clusters at the wall, while away from the boundary the Bi distribution corresponds to a [100] pseudocubic perovskite cell (Figure 1.9). At the flat wall itself in the HAADF images, dark clusters between two bright Bi clusters can be observed, with very similar contrast

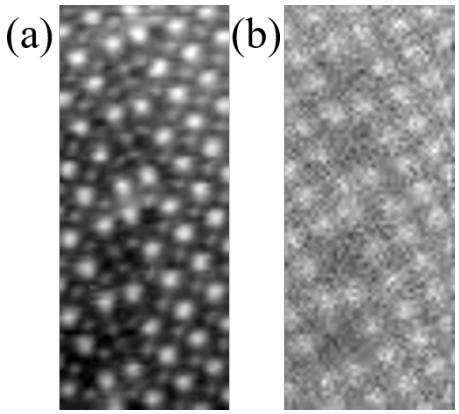

Figure 5.4: Core-loss EELS data (a) HAADF-STEM image and (b) element map of Bi. Image size is 1.31 nm × 3.15 nm.

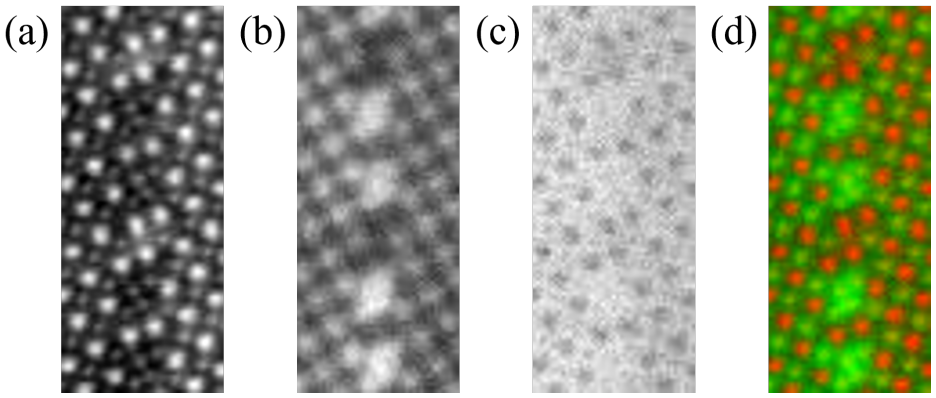

Figure 5.5: Core-loss EELS data (a) HAADF-STEM image, (b) element map of Fe, (c) element map of O and (d) overlap of HAADF (red, corresponding to Bi) and Fe (green).Image size is 1.32 nm × 3.13 nm.

to the Fe atoms in bulk BFO. Figure 5.5(b-c) shows EELS elemental distribution maps of Fe, where Fe forms diamond-like 2 × 2 clusters at the flat wall, taking up the dark regions in the HAADF image, but regular pseudocubic cells away from the flat wall. The O map (Figure 5.5(c)) shows delocalisation of the excitation of O-K edge, only showing lower signal intensities at the Bi column positions. It indicates that the dark clusters in the HAADF image have similar oxygen content to the bulk BFO matrix since the contrast is flat and even in the map, but it is difficult to determine the precise location of oxygen in the map. An overlapped figure of HAADF (mainly showing Bi position), Fe and O EELS-SI map is shown in Figure 5.5(d), which clearly shows alternating Bi and Fe+O clusters repeating along the wall direction and the flat domain wall itself has a structure and stoichiometry

different from bulk BFO. Similar structure has been reported in thin film BFO which endures either doping[19; 135; 136] or a change of substrate temperature during growth[129; 128; 137].

5.4 Onset energy difference between Fe and O

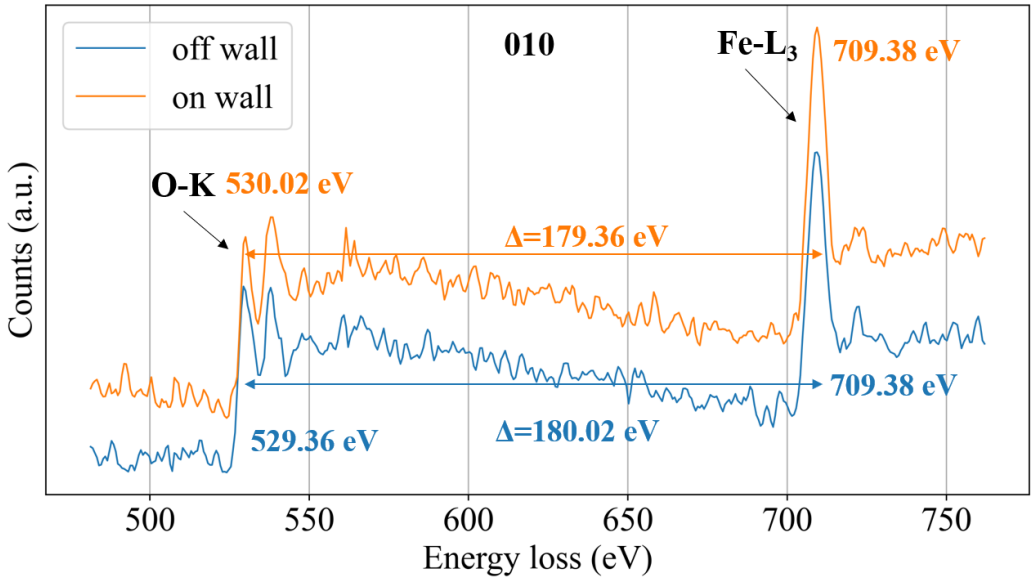

Figure 5.6: Coarse EELS acquisition taken on/off the flat domain wall from [010] view-direction, covering both O and Fe.

Oxidation state of Fe can be determined mainly by using two approaches, either based on the Fe L_3/L_2 intensity ratios[138; 139], or based on the onset energy difference (ΔE) of O-K and Fe-L_3 edges[140; 78; 35; 141]. Since the first approach using the Fe L_3/L_2 intensity ratios is not suitable for determination of the Fe^{4+} oxidation state[140], here we use the calculation of onset energy difference ΔE to determine the local Fe oxidation state.

High resolution core-loss EELS from [010] (Figure 5.6) and [$\bar{1}$10] (Figure 5.7) view-direction were conducted across the flat domain walls and ΔE between O-K and Fe-L_3 edges was extracted to investigate the chemical shift of Fe-O bonding, since there is a linear relationship between this onset energy and the oxidation state of Fe.[78; 35; 141] From [010] direction (Figure 5.6) a ΔE of 179.36 eV is found between O-K (530.02 eV) and Fe-L_3 (709.38 eV) edges on the flat domain wall, while off the wall ΔE is 180.02 eV between O-K (529.36 eV) and Fe-L_3 (709.38 eV), corresponding to a 0.66 eV increase compared to that on the flat domain wall. Both

ΔE are fingerprints of Fe^{3+} states.[40; 78] The smaller ΔE on the wall indicates a slight drop of the local Fe oxidation state[78; 35; 141]; in another word, Fe on the domain wall is slightly negatively charged compared to its counterpart in the bulk,[40] which in turn helps compensate the large polar discontinuity at the flat wall (see Section 4.3).

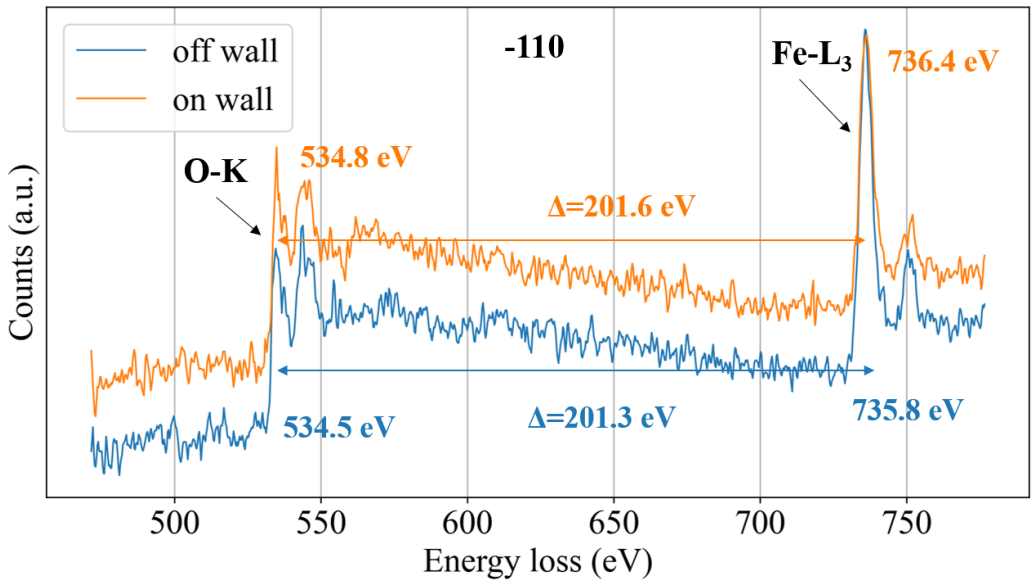

Figure 5.7: Coarse EELS acquisition taken on/off the flat domain wall from [$\bar{1}$10] view-direction, covering both O and Fe.

From [$\bar{1}$10] direction (Figure 5.7), a ΔE of 201.6 eV is found between O-K (534.8 eV) and Fe-L_3 (736.4 eV) on the flat domain wall, while off the wall ΔE is 201.3 eV between O-K (534.5 eV) and Fe-L_3 (735.8 eV). Both energy difference are higher than [010] view-direction. At the same time, there is a clear contrast of the Fe-L_3 peak intensity on/off the wall. In the plot the data are shifted vertically for better comparison, but it is obvious that on the wall there is a lower Fe-L_3 peak intensity that cancelled the offset. Approximately the ratio of Fe-L_3/O-K changes from 1.51 on wall (intensity value 929.83/616.36) to 2.15 off wall (intensity value 1146.12/531.98). The reason is likely to be that from [$\bar{1}$10] direction Fe sits closer to Bi (Figure 4.13), and since Fe is much lighter than Bi, its signal is lowered by competitive channeling onto Bi atom columns. The same pattern was also found in the fine ELNES structure of Fe (Figure 5.11) Yet to our knowledge, this is the first dataset of ELNES analysis on [$\bar{1}$10] BFO, and little reference could be found in the existing literature.

5.5 ELNES structure of Fe and O

5.5.1 Oxygen

As introduced earlier, the flat domain walls are made up of alternating Bi and Fe+O clusters, and here the O ELNES was collected at the position Fe+O clusters since the interaction of Fe with O octahedra contains more information about the structure. The O-K edge spectrum of BFO (Figure 5.8 and Figure 5.9) can be divided into two parts: a prepeak (A) region from 531 to 538 eV and a postedge peak (B) from 538 to 548 eV, in good agreement with theoretical calculations and experimental reports.[142; 141; 35] The prepeak A contains two dominant subpeaks, one around 533.5 eV (labeled A1), identified as the result of hybridization between the O-2p and Fe-3d states[142]; and a smaller one around 535.5 eV (labeled A2), which was attributed to the combined influence of backscattering on O^{2-} ions together with hybridisation of O-2p states with p-like states in Bi.[135; 141] Additionally, there is a shoulder prepeak (P) before peak A1 around 531.35 eV which arises due to the the crystal-field splitting of Fe-3d band into t_{2g} and e_g states and their hybridization with O-2p.[141] The peak B stems from the transitions to hybridized O-2p and Fe-4s states[143] and is related to the local coordination of the Fe atoms set up by the nearest oxygen neighbors.[142]

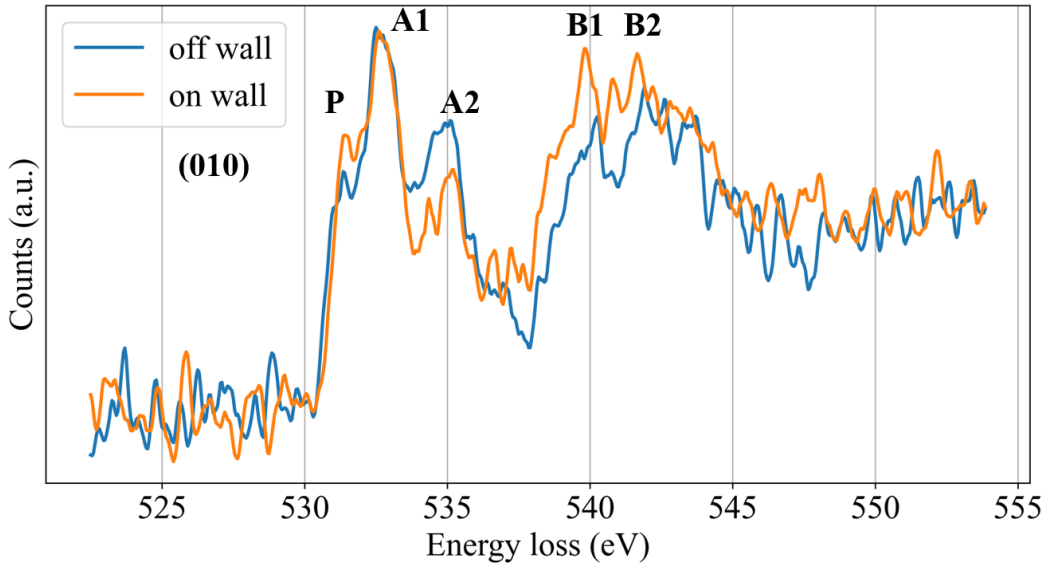

Figure 5.8: Fine O ELNES acquisition taken on/off the flat domain wall from [010] view-direction.

In Figure 5.8 there is a slight decrease of the A2/A1 ratio from 0.63 (on

Peak	Position on wall	Intensity on wall	Position off wall	Intensity off wall
P	531.40	0.72	531.35	0.62
A1	532.60	0.99	532.50	1.00
A2	535.20	0.63	535.10	0.76
B1	539.85	0.94	540.25	0.77
B2	541.65	0.93	541.90	0.84

Table 5.1: Edge position and intensity of the fine O ELNES acquisition taken on/off the flat domain wall from [010] view-direction. Intensity of A1 peak off wall is set as reference.

wall) to 0.76 (off wall), as expected that A2 peak may be depressed in the absence of Bi (since the data was collected at Fe+O clusters).[135] On comparison with spectra of α/γ-Fe_2O_3 reported by Paterson et al.[144], the flat wall displays an K-K ELNES more similar to γ-Fe_2O_3, specifically in the shape of the A peak, which mainly peaks at A1 position and displays lower intensity at A2 position. There is a clear splitting of B peak into two subpeaks on/off the wall. While A peaks stay at almost the same position, there is a $\sim$ +0.6 eV shift off the wall, and where it peaks change from B1 (539.85 eV) on wall to B2 (541.90 eV) off wall. Our observation of the ELNES variation on/off the flat wall is consistent with studies from Rossell et al.[142] and MacLaren et al.[19; 135; 136] It suggests that the ions in the flat wall are very similarly octahedrally coordinated as in the bulk BFO, but the coordination is either in tetragonally distorted or undistorted octahedra, rather than in rhombohedrally distorted octahedra. Therefore, the differences observed in the B peaks could indicate difference in the Fe-O bonding due to difference coordination geometries for Fe atoms, for example, in rhombohedral BFO and edge-sharing Fe-octahedra. This observation corroborates the atomic structure information derived from STEM.

Peak	Position on wall	Intensity on wall	Position off wall	Intensity off wall
P	532.00	0.72	531.60	0.57
A1	532.80	0.99	533.20	1.00
A2	535.45	0.69	534.85	0.67
B1	539.85	0.79	540.70	0.79
B2	540.95	0.90	542.449	0.83

Table 5.2: Edge position and intensity of the fine O ELNES acquisition taken on/off the flat domain wall from [$\bar{1}$10] view-direction. Intensity of A1 peak off wall is set as reference.

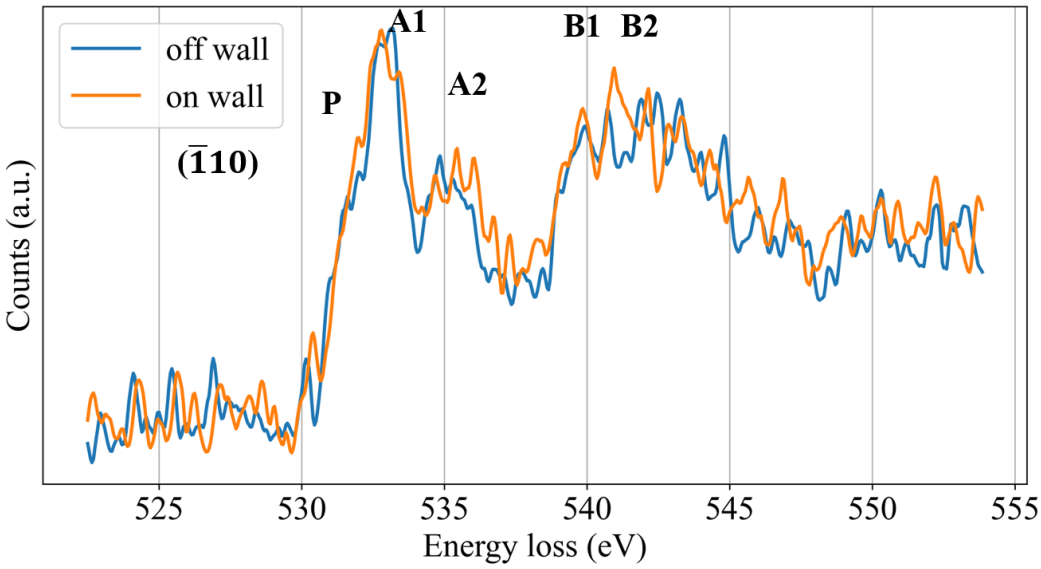

Figure 5.9: Fine O ELNES acquisition taken on/off the flat domain wall from [$\bar{1}$10] view-direction.

Above mentioned differences are less obvious in the [$\bar{1}$10] ELNES data (Figure 5.9. The shoulder peak P is not well-defined as from [010] view-direction, especially when on the wall. Position of A2 peaks moves right from 534.85 eV off wall to 535.45 eV on wall. Splitting of B peaks is less noticeable from this view-direction.

5.5.2 Fe

Peak	Position on wall	Intensity on wall	Position off wall	Intensity off wall
P	711.20	0.44	711.90	0.30
L3	712.75	1.00	712.65	0.81
L2	726.50	0.21	724.60	0.20

Table 5.3: Edge position and intensity of the fine Fe ELNES acquisition taken on/off the flat domain wall from [010] view-direction. Intensity of L3 peak on wall is set as reference.

Figure 5.8 shows the Fe $L_{3,2}$ edge on/off the flat domain wall when seen from [010] view-direction. The Fe-$L_{3,2}$ edge corresponds to excitation from the Fe-2p electrons into empty Fe-3d states.[142] These transitions produce two main features at $\sim$ 712 eV (L_3) and $\sim$ 725 eV (L_2) that are separated by $\sim$ 13 eV due to spin-orbit splitting of the Fe-2p core hole into Fe-2$p_{3/2}$ and Fe-2$p_{1/2}$ states.[135; 142] Besides,

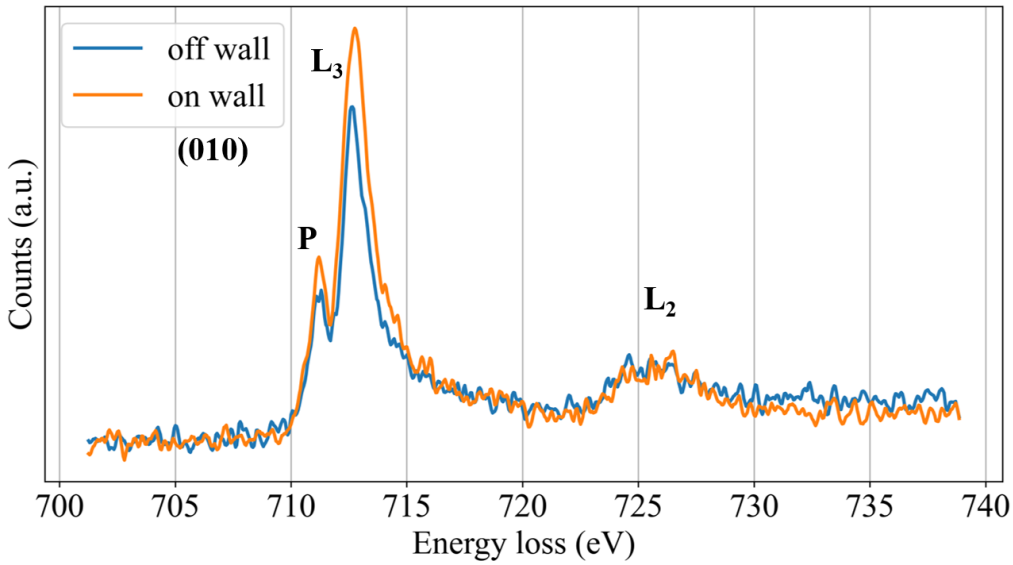

Figure 5.10: Fine Fe ELNES acquisition taken on/off the flat domain wall from [010] view-direction.

a shoulder on the left side of L_3 peak can be found, and this further splitting of the $3d$ orbital states into t_{2g} and e_g level is due to the octahedral crystal field. The measured energy separation between t_{2g} and e_g states is $\sim$ 1.5 eV. Such a well-resolved splitting of the Fe-L_3 edges is a characteristic of Fe^{3+} and inconsistent with Fe^{2+} or mixed valence[142; 35]. This conclusively demonstrates dominant Fe^{3+} both on and off the wall. The L_3 peaks slightly earlier off wall (712.65 eV) than on wall (712.75 eV). The intensity of L_3 peak is stronger on the wall, which totally makes sense as the data is taken at the Fe+O cluster in the HAADF images. There seems to be a change in where L_2 peaks, from 724.90 eV off wall to 726.50 eV on wall. Apart from that, there is no other detectable change in this ELNES between the perovskite and the wall, which would suggest that the Fe is in the same 3+ oxidation state in the wall as in the surrounding matrix.

Peak	Position on wall	Intensity on wall	Position off wall	Intensity off wall
P	710.95	0.64	711.10	0.64
L3	712.65	1.00	712.50	1.43
L2	724.60	0.31	726.40	0.35

Table 5.4: Edge position and intensity of the fine Fe ELNES acquisition taken on/off the flat domain wall from [$\bar{1}$10] view-direction. Intensity of L3 peak on wall is set as reference.

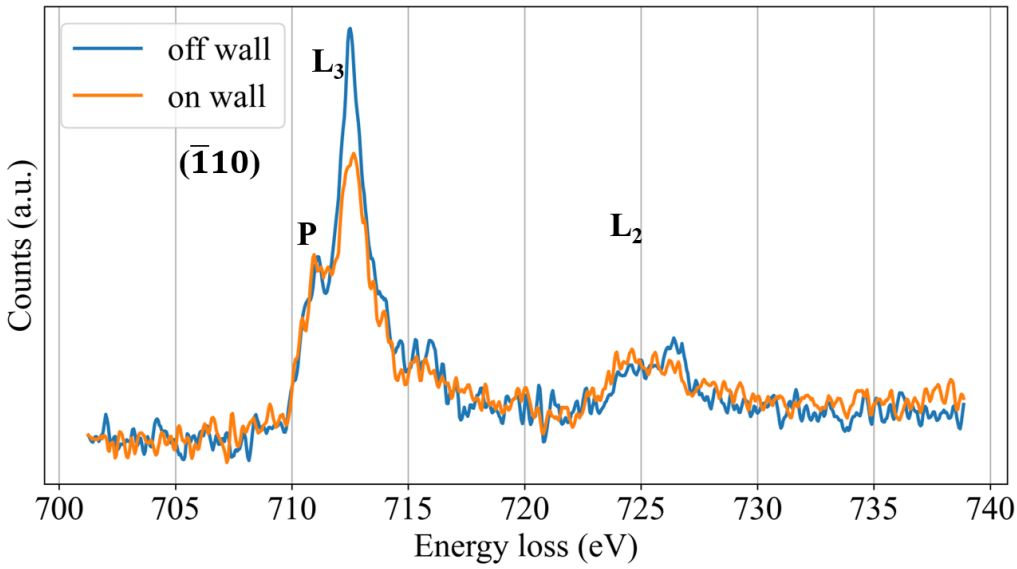

Figure 5.11: Fine Fe ELNES acquisition taken on/off the flat domain wall from [1̄10] view-direction.

The most obvious feature of the Fe ELNES structure when seen from [1̄10] view-direction (Figure 5.7) is that the intensity of Fe-L_3 is much weaker on the wall. The reason could be that from [1̄10] view-direction the flat domain wall (Figure 4.13) has a hook-like structure where Fe stays very close to Bi, and there is no separate Bi or Fe+O clusters like those from [010] view-direction. Besides, the L_2 peak moves right from 724.60 eV on wall to 726.40 eV off wall. No other difference could be found from this view-direction.

5.6 Summary and Discussion

In this chapter, high resolution EELS has been conducted with the aim to better understand the reconstructed flat domain walls. It is found to have a slightly higher bandgap value compared to the bulk BFO. EELS element map indicates the flat wall to be consist of alternating Bi and Fe+O clusters up to two unit cells in width. Both energy onset difference and fine ELNES indicate Fe and O in the flat domain walls are in very similar conditions to the adjacent bulk material, while the minor difference shows 1) Fe atoms have different coordination geometries, i.e., tetragonally-distorted and edge-sharing octahedra rather than a rhombohedrally-distorted and corner-sharing ones, which is consistent with the STEM observations; 2) oxidation state of Fe slightly drops at the flat wall, which makes sense as the local reconstructed

structure is different from the bulk, and it in turn helps compensate the local polar discontinuity.

The reconstructed nano-regions observed in the flat 180° head-to-head walls is an indication that they formed during crystal growth, while the periodic domain structure indicates a degree of self-organisation. Synthesis of BFO is only possible within a narrow range of conditions, both in the deposition of thin epitaxial layers[38; 129; 128; 19; 135; 136] and as ceramics or single crystals[citation]. In crystal growth, secondary phases like Bi-rich sillenite $Bi_{25}FeO_{39}$ and Bi-poor mullite $Bi_5Fe_4O_9$ readily form to accommodate deviations from perfect stoichiometry, e.g. due to the relative volatility of Bi_2O_3. [hlSection 1.x]. In epitaxial thin film growth, planar defects that are locally nonstoichiometric have been observed by several researchers.[19; 135; 136; 128; 129] Maclaren and co-workers[19; 135; 136] showed that either Ti or Mn doping in $Bi_{0.85}Nd_{0.15}FeO_3$ thin films causes formation of edge-sharing octahedra, resembling the structure of γ-Fe_2O_3, while Li and co-workers[129; 128] indicated an increment of substrate temperature during film growth can result in γ-Fe_2O_3 impurity phases. The atomic structure of the 180° flat domain walls in our single crystal material appear almost identical to these planar defects observed previously, as well as the ½[110] half unit-cell rigid body shift of the bulk materials across them. The deviation from stoichiometry gives a local excess of oxygen anions, giving a negative charge density estimated to be between -68 μCcm^{-2} and -110 μCcm^{-2}. We estimate a negative charge density of -188 μCcm^{-2} for the flat domain walls in our crystal, calculated by the real space reconstruction of $\boldsymbol{P_s}$ distribution. The effect of these negatively charged planar defects on the surrounding BFO matrix is to induce local polarisation towards them and stabilize an otherwise unfavourable domain structure.

Several contributions to the formation of this unique structure in our single crystals could be discussed. Influence from growth temperature has been highlighted by Li and co-workers[129; 128] as a slight increase from the optimal temperature would introduce additional Fe_2O_3 phase, thus form a similar structure. In our experiment, the crystal experienced a wide range of temperature drop from 1170 K to 875 K. The slow temperature decreasing rate might leave a window that optimises the growth condition of the structure. At the same time, similar structures have only been found at the positive bonding end of $\boldsymbol{P_s}$, i.e., $\boldsymbol{P_s}$ are pointing towards them[129; 128; 19; 135; 136], because of the highly negative charge caused by their non-stoichiometry from bulk BFO. Since most of our crystal growth happens below T_C and the material is polarized, their appearance during the growth might help compensate/modulate the large open-end spontaneous polarisation. In the mean-

while, it is plausible that their existence is also coupled with the intrinsic strain of the sample. In thin films similar structures are found to run parallel to the substrate (001) surface[129; 128; 19; 135; 136], as symmetry-lowering distortion arises from in-plane contraction or elongation because of lattice mismatch between film and substrate, and unique structure of the boundary might help to release accumulated strain along that direction. In our single crystals, which could be seen as perfect rhombohedral, the flat walls are found to run only along (112) planes, which might offer the best fit for their unique structure within the bulk and help release local strain in a narrow region. To summarise, considering the multiferroic nature of BFO, we anticipate the appearance of those unique structure happens during sample growth to accommodate the uncompensated ferroelectric $\boldsymbol{P_s}$, as well as intrinsic strain, within the crystal and help the growth process.

Chapter 6

Summary and future work

This chapter highlights the main results of the investigations introduced in this thesis and offers some perspectives for future experimentation for a further understanding of this sample and the material.

The domain structure in the flux-grown single crystal BFO has been re-examined in Chapter 3 by multiple microscopy methods, ranging from traditional transmission electron microscopy to electron diffraction. At the scale of its size, the crystal has four large ferroelastic domains. Within each ferroelastic domain, the crystal has a complex 3D domain structure that is made up of a dense array of 180° flat domain walls running along (112) planes with a spacing between $60 - 120$ nm, which also produces streaks in the electron diffraction pattern. Between each pair of flat domain walls, the bulk BFO is divided into two domains with opposite polarity, separated by 180° sawtooth domain walls comprised of three-faceted peaks consisting of a $(11\bar{2})$ NDW and two CDWs with orientations close to $(3\bar{2}1)$ and $(\bar{2}31)$. A 3D model that faithfully describes the actual domain structure inside the crystal has also been proposed by examining the sample from multiple view-directions.

In Chapter 4, atomic scale $\boldsymbol{P_s}$ mapping and quantification of the flux-grown single crystal BFO has been presented. The 180° tail-to-tail sawtooth domain walls in the single crystal BFO were revealed to have different $\boldsymbol{P_s}$ transition behaviour, with the $(11\bar{2})$ NDW facets being Ising-type wall and the $(3\bar{2}1)$ and $(\bar{2}32)$ CDWs facets being mixed Néel/Bloch/Ising-type. The 180° head-to-head flat domain walls were found to have a reconstructed atomic structure different from the bulk material which is, at the same time, highly negatively charged to compensate the polar discontinuity at the flat walls.

Finally in Chapter 5, high resolution EELS has been conducted to better understand the reconstructed flat domain walls. Our calculation shows a slight

increase of the bandgap value at the flat domain walls compared to the bulk BFO, which is assumably the result of structure variation. The flat walls are found to consist of alternating Bi and Fe+O clusters up to two unit cells in width, while both energy onset difference and fine ELNES indicate Fe and O in the flat domain walls are in very similar conditions to the adjacent bulk material, and the minor difference shows Fe atoms have different coordination geometries, i.e., tetragonally-distorted and edge-sharing octahedra rather than a rhombohedrally-distorted and corner-sharing ones, which is consistent with the STEM observations.

Looking at it another way, this thesis serves as a map to the flux-grown single crystal BFO, which leads readers to observe the sample from various view-directions across a broad scale, from reciprocal space and from the perspective of chemical properties. However, like any map, there are limitations inherent in the methodology, instruments used, and the mapmaker's perspective. Several questions remain uncovered within the duration of this work:

First, during this work we have made a handful attempts to measure potential conductivity difference of the flat/sawtooth walls versus bulk BFO by means of c-AFM,[41] but unfortunately, no useful signals can be found except background noises. It could mean there is no variation of the conductivity, yet according to the existing publication[41; 21] it is not difficult to find a hint of the conductivity change of CDWs in BFO (at least thin film BFO). It could also suggest a refinement of our experimental design, since the domain structure in this single crystal is much complicated than thin films. For example, in thin film systems the domain walls generally penetrates straightly through the film,[38; 129; 118; 41] i.e., from the substrate to the film surface, so it is easy to form a current path between the AFM tip and the bottom electrode. While it might not be the case in the single crystal-the sawtooth walls are often found to terminate at the flat walls (Figure 3.3),[48] as a result the current path might be interrupted somewhere inside the crystal, rather than reaching the bottom electrode. A possible solution is to polish another bulk crystal to be wedge-shaped, and at its thinnest part there might be a complete current path to enable conductivity measurement.

Second, sample growth is the core induction of the domain structure reported in this work, while it is hard to repeat the growth and find out the growth detail of the flat domain walls within the duration of this electron microscopy-orientated thesis, as the growth process was very complicated and nearly two decades ago. We are still curious about what causes the formation of the reconstructed flat domain walls? Could it be local concentration/temperature/electrostatic/magnetic variation? And what causes its periodicity? Can it be reproduced in thin film systems?

This reconstructed flat domain walls are the reason of the low $\boldsymbol{P_s}$ measurement of this crystal, is it also the case of the crystals/ceramics grown by other groups? From the perspective of electron microscopy, it is worthwhile to study other single crystals, down to atomic scale, to make an easy but helpful comparison. At the same time, it is also very tempting to find out if the application of external electrical/magnetic field during the sample growth can influence the final domain structure.

Lastly, this work focuses primarily on analyzing the electrostatic energy contributing to the final domain structure, while other factors also play a role but are not explored in our research. The magnetic component, for instance, has not be discussed due to the limits of current methodology, and the potential influence from these components cannot be taken for granted. As discussed, BFO is multiferroic and the chiral properties of the domain walls is the result of coupling of multiple orders,[94] it is likely to find possible change of magnetic properties at the domain walls. Magnetic force microscopy (MFM, the magnetism-dedicated mode of SPM) could be a powerful tool to study the magnetic domain and domain walls of this crystal. At the same time, the rapid development of 4D-STEM could help study the distribution of (uncompensated) magnetic/electrical field inside the sample.

Bibliography

[1] Alexander K. Tagantsev, L. Eric Cross, and Jan Fousek. *Domains in Ferroic Crystals and Thin Films*. Springer New York, NY, 2010.

[2] James F. Scott. *Ferroelectric Memories*. Springer Berlin, Heidelberg, 2000.

[3] Nicola A. Hill. Why are there so few magnetic ferroelectrics? *The Journal of Physical Chemistry B*, 104(29):6694–6709, 2000.

[4] Hans Schmid. Multi-ferroic magnetoelectrics. *Ferroelectrics*, 162(1):317–338, 1994.

[5] W. Eerenstein, N. D. Mathur, and J. F. Scott. Multiferroic and magnetoelectric materials. *Nature*, 442:759–765, 8 2006.

[6] R. Ramesh and N. Spaldin. Multiferroics: progress and prospects in thin films. *Nature Materials*, 6:21–29, 2007.

[7] Manfred Fiebig, Thomas Lottermoser, Dennis Meier, and Morgan Trassin. The evolution of multiferroics. *Nature Reviews Materials*, 1:16046, 2016.

[8] M. Ye. Zhuravlev, R. F. Sabirianov, S. S. Jaswal, and E. Y. Tsymbal. Giant electroresistance in ferroelectric tunnel junctions. *Phys. Rev. Lett.*, 94:246802, Jun 2005.

[9] J. P. Velev, Chun-Gang Duan, K. D. Belashchenko, S. S. Jaswal, and E. Y. Tsymbal. Effect of ferroelectricity on electron transport in Pt/batio$_3$/Pt tunnel junctions. *Phys. Rev. Lett.*, 98:137201, Mar 2007.

[10] Evgeny Y. Tsymbal and Hermann Kohlstedt. Tunneling across a ferroelectric. *Science*, 313(5784):181–183, 2006.

[11] Andy Quindeau, Vladislav Borisov, Ignasi Fina, Sergey Ostanin, Eckhard Pippel, Ingrid Mertig, Dietrich Hesse, and Marin Alexe. Origin of tunnel elec-

troresistance effect in $PbTio_3$-based multiferroic tunnel junctions. *Phys. Rev. B*, 92:035130, Jul 2015.

[12] M. Fiebig, Th. Lottermoser, D. Frohlich, A. V. Goltsev, and R. V. Pisarev. Observation of coupled magnetic and electric domains. *Nature*, 419:818–820, 2002.

[13] T. Kimura, T. Goto, H. Shintani, K. Ishizaka, T. Arima, and Y. Tokura. Magnetic control of ferroelectric polarization. *Nature*, 426:55–58, 2003.

[14] N. Hur, S. Park, P. A. Sharma, J. S. Ahn, S. Guha, and S-W. Cheong. Electric polarization reversal and memory in a multiferroic material induced by magnetic fields. *Nature*, 429:392–395, 2004.

[15] J. Wang, J. B. Neaton, H. Zheng, V. Nagarajan, S. B. Ogale, B. Liu, D. Viehland, V. Vaithyanathan, D. G. Schlom, U. V. Waghmare, N. A. Spaldin, K. M. Rabe, M. Wuttig, and R. Ramesh. Epitaxial BiFeO3 Multiferroic Thin Film Heterostructures. *Science*, 299(5613):1719–1722, 2003.

[16] Gustau Catalan and James F. Scott. Physics and applications of bismuth ferrite. *Advanced Materials*, 21(24):2463–2485, 2009.

[17] Naoshi Ikeda, Hiroyuki Ohsumi, Kenji Ohwada, Kenji Ishii, Toshiya Inami, Kazuhisa Kakurai, Youichi Murakami, Kenji Yoshii, Shigeo Mori, Yoichi Horibe, and Hijiri Kito. Ferroelectricity from iron valence ordering in the charge-frustrated system lufe2o4. *Nature*, 436:1136–1138, 2005.

[18] Jeroen van den Brink and Daniel I Khomskii. Multiferroicity due to charge ordering. *Journal of Physics: Condensed Matter*, 20(43):434217, oct 2008.

[19] Ian MacLaren, Liqiu Wang, Owen Morris, Alan J. Craven, Robert L. Stamps, Bernhard Schaffer, Quentin M. Ramasse, Shu Miao, Kambiz Kalantari, Iasmi Sterianou, and Ian M. Reaney. Local stabilisation of polar order at charged antiphase boundaries in antiferroelectric (Bi0.85Nd0.15)(Ti0.1Fe 0.9)O3. *APL Materials*, 1, 2013.

[20] S. H. Baek and C. B. Eom. Reliable polarization switching of BiFeO3. *Philosophical Transactions of the Royal Society A: Mathematical, Physical and Engineering Sciences*, 370(1977):4872–4889, 2012.

[21] Akash Bhatnagar, Ayan Roy Chaudhuri, Young Heon Kim, Dietrich Hesse, and Marin Alexe. Role of domain walls in the abnormal photovoltaic effect in BiFeO3. *Nature Communications*, 4:2835, 2013.

[22] S. H. Baek, H. W. Jang, C. M. Folkman, Y. L. Li, B. Winchester, J. X. Zhang, Q. He, Y. H. Chu, C. T. Nelson, M. S. Rzchowski, X. Q. Pan, R. Ramesh, L. Q. Chen, and C. B. Eom. Ferroelastic switching for nanoscale non-volatile magnetoelectric devices. *Nature Materials*, 9(4):309–314, 2010. Number: 4.

[23] James R. Teague, Robert Gerson, and W. J. James. Dielectric hysteresis in single crystal BiFeO3. *Solid State Communications*, 8:1073–1074, 7 1970.

[24] F. Kubel and H. Schmid. Structure of a ferroelectric and ferroelastic monodomain crystal of the perovskite BiFeO3. *Acta Crystallographica Section B*, 46(6):698–702, 1990.

[25] Karin M. Rabe, Charles H. Ahn, and Jean-Marc Triscone. *Physics of Ferroelectrics*. Springer Berlin, Heidelberg, 2007.

[26] A. von Hippel. Ferroelectricity, domain structure, and phase transitions of barium titanate. *Rev. Mod. Phys.*, 22:221–237, Jul 1950.

[27] Walter J. Merz. Double hysteresis loop of batio$_3$ at the curie point. *Phys. Rev.*, 91:513–517, Aug 1953.

[28] J. Harada, T. Pedersen, and Z. Barnea. X-ray and neutron diffraction study of tetragonal barium titanate. *Acta Crystallographica Section A*, 26(3):336–344, 1970.

[29] G. Shirane, R. Pepinsky, and B. C. Frazer. X-ray and neutron diffraction study of ferroelectric PbTiO3. *Acta Crystallographica*, 9(2):131–140, 1956.

[30] V. V. Shvartsman, W. Kleemann, R. Haumont, and J. Kreisel. Large bulk polarization and regular domain structure in ceramic BiFeO3. *Applied Physics Letters*, 90(17):172115, 04 2007.

[31] D. Lebeugle, D. Colson, A. Forget, and M. Viret. Very large spontaneous electric polarization in BiFeO3 single crystals at room temperature and its evolution under cycling fields. *Applied Physics Letters*, 91(2):022907, 2007.

[32] Xavi Martí, Pilar Ferrer, Julia Herrero-Albillos, Jackeline Narvaez, Vaclav Holy, Nick Barrett, Marin Alexe, and Gustau Catalan. Skin layer of bifeo$_3$ single crystals. *Phys. Rev. Lett.*, 106:236101, Jun 2011.

[33] A. Berger, D. Hesse, A. Hähnel, M. Arredondo, and M. Alexe. Regular nanodomain vertex arrays in BiFeO3 single crystals. *Phys. Rev. B*, 85:064104, 2012.

[34] Chun-Lin Jia, Lei Jin, Dawei Wang, Shao-Bo Mi, Marin Alexe, Dietrich Hesse, Helena Reichlova, Xavi Marti, Laurent Bellaiche, and Knut W. Urban. Nanodomains and nanometer-scale disorder in multiferroic bismuth ferrite single crystals. *Acta Materialia*, 82:356–368, 2015.

[35] Oana Condurache, Goran Dražić, Tadej Rojac, Hana Uršič, Brahim Dkhil, Andraž Bradeško, Dragan Damjanovic, and Andreja Benčan. Atomic-level response of the domain walls in bismuth ferrite in a subcoercive-field regime. *Nano Letters*, 0(0):null, 0. PMID: 36458590.

[36] P. Ravindran, R. Vidya, A. Kjekshus, H. Fjellvåg, and O. Eriksson. Theoretical investigation of magnetoelectric behavior in $BiFeo_3$. *Phys. Rev. B*, 74:224412, Dec 2006.

[37] Claude Ederer and Nicola A. Spaldin. Effect of epitaxial strain on the spontaneous polarization of thin film ferroelectrics. *Phys. Rev. Lett.*, 95:257601, Dec 2005.

[38] Christopher T. Nelson, Benjamin Winchester, Yi Zhang, Sung-Joo Kim, Alexander Melville, Carolina Adamo, Chad M. Folkman, Seung-Hyub Baek, Chang-Beom Eom, Darrell G. Schlom, Long-Qing Chen, and Xiaoqing Pan. Spontaneous vortex nanodomain arrays at ferroelectric heterointerfaces. *Nano Letters*, 11(2):828–834, 2011. PMID: 21247184.

[39] G. Catalan, J. Seidel, R. Ramesh, and J. F. Scott. Domain wall nanoelectronics. *Rev. Mod. Phys.*, 84:119–156, Feb 2012.

[40] Tadej Rojac, Andreja Bencan, Goran Drazic, Naonori Sakamoto, Hana Ursic, Bostjan Jancar, Gasper Tavcar, Maja Makarovic, Julian Walker, Barbara Malic, and Dragan Damjanovic. Domain-wall conduction in ferroelectric BiFeO3 controlled by accumulation of charged defects. *Nature Materials*, 16(3):322–327, 2017. Number: 3.

[41] J. Seidel, L. W. Martin, Q. He, Q. Zhan, Y.-H. Chu, A. Rother, M. E. Hawkridge, P. Maksymovych, P. Yu, M. Gajek, N. Balke, S. V. Kalinin, S. Gemming, F. Wang, G. Catalan, J. F. Scott, N. A. Spaldin, J. Orenstein, and R. Ramesh. Conduction at domain walls in oxide multiferroics. *Nature Materials*, 8(3):229–234, 2009. Number: 3.

[42] Ming-Min Yang, Zheng-Dong Luo, Dong Jik Kim, and Marin Alexe. Bulk photovoltaic effect in monodomain BiFeO3 thin films. *Applied Physics Letters*, 110(18):183902, 2017.

[43] Jonathan J. P. Peters, Geanina Apachitei, Richard Beanland, Marin Alexe, and Ana M. Sanchez. Polarization curling and flux closures in multiferroic tunnel junctions. *Nature Communications*, 7:13484, 2016.

[44] M. Dawber, K. M. Rabe, and J. F. Scott. Physics of thin-film ferroelectric oxides. *Reviews of Modern Physics*, 77(4):1083–1130, 2005.

[45] M. E. Lines and A. M. Glass. *Principles and Applications of Ferroelectrics and Related Materials*. Oxford University Press, 02 2001.

[46] Makoto Tachibana. *Beginner' s Guide to Flux Crystal Growth*. Springer Tokyo, 2017.

[47] W. Ge, R. Beanland, M Alexe, and A. M. Sanchez. 180° head-to-head flat domain walls in single crystal bifeo3. *Microstructures*, 3(3), 2023.

[48] Wanbing Ge, Richard Beanland, Marin Alexe, and Ana M. Sanchez. 3d reconstruction of sawtooth 180° tail-to-tail domain walls in single crystal bifeo3. *Advanced Functional Materials*, n/a(n/a):2301171, 2023.

[49] J. Valasek. Piezo-electric and allied phenomena in rochelle salt. *Phys. Rev.*, 17:475–481, Apr 1921.

[50] A. von Hippel, R. G. Breckenridge, F. G. Chesley, and Laszlo Tisza. High dielectric constant ceramics. *Ind. Eng. Chem.*, 38:1097–1109, 1946.

[51] Jürgen Rödel, Wook Jo, Klaus T. P. Seifert, Eva-Maria Anton, Torsten Granzow, and Dragan Damjanovic. Perspective on the development of lead-free piezoceramics. *Journal of the American Ceramic Society*, 92(6):1153–1177, 2009.

[52] Markys G. Cain, editor. *Characterisation of Ferroelectric Bulk Materials and Thin Films*. Springer Dordrecht, 2016.

[53] R. Clausius. *Die Mechanische Wärmetheorie*, volume 2, page 62 –97. Braunschweig, 1879.

[54] O.F. Mossotti. Mem. di math. *e Fisica d. Soc. Italiana d. Scienze*, 24, 1850.

[55] R. Resta. Theory of the electric polarization in crystals. *Ferroelectrics*, 136(1):51–55, 1992.

[56] Nicola A. Spaldin. A beginner's guide to the modern theory of polarization. *Journal of Solid State Chemistry*, 195:2–10, 2012. Polar Inorganic Materials: Design Strategies and Functional Properties.

[57] R. D. King-Smith and David Vanderbilt. Theory of polarization of crystalline solids. *Physical Review B*, 47(3):1651–1654, 1993. Number: 3.

[58] R. Resta, M. Posternak, and A. Balderescrt. First-principles theory of polarization in ferroelectrics. *MRS Online Proceedings Library*, 291, 1992.

[59] J. B. Neaton, C. Ederer, U. V. Waghmare, N. A. Spaldin, and K. M. Rabe. First-principles study of spontaneous polarization in multiferroic $BiFeo_3$. *Phys. Rev. B*, 71:014113, Jan 2005.

[60] V. M. Goldschmidt. Die gesetze der krystallochemie. *Naturwissenschaften*, 14, 1926.

[61] Ronald E. Cohen. Origin of ferroelectricity in perovskite oxides. *Nature*, 358(6382):136–138, 1992.

[62] J.P. Remeika and A.M. Glass. The growth and ferroelectric properties of high resistivity single crystals of lead titanate. *Materials Research Bulletin*, 5(1):37–45, 1970.

[63] A.M. Glazer. The classification of tilted octahedra in perovskites. *Acta Cryst.*, B28:3384–3392, 1972.

[64] David I. Woodward and Ian M. Reaney. Electron diffraction of tilted perovskites. *Acta Crystallographica Section B*, 61(4):387–399, Aug 2005.

[65] Richard Beanland and Pam A. Thomas. Symmetry and defects in rhombohedral single-crystalline $na_{0.5}bi_{0.5}tio_3$. *Phys. Rev. B*, 89:174102, May 2014.

[66] R. Palai, R. S. Katiyar, H. Schmid, P. Tissot, S. J. Clark, J. Robertson, S. A. T. Redfern, G. Catalan, and J. F. Scott. phase and − metal-insulator transition in multiferroic bi fe o 3. *Physical Review B*, 77(1):014110, 2008. Number: 1.

[67] Donna C. Arnold, Kevin S. Knight, Finlay D. Morrison, and Philip Lightfoot. Ferroelectric-paraelectric transition in $bifeo_3$: Crystal structure of the orthorhombic β phase. *Phys. Rev. Lett.*, 102:027602, Jan 2009.

[68] Igor A. Kornev, S. Lisenkov, R. Haumont, B. Dkhil, and L. Bellaiche. Finite-temperature properties of multiferroic bifeo$_3$. *Phys. Rev. Lett.*, 99:227602, Nov 2007.

[69] R. Haumont, J. Kreisel, P. Bouvier, and F. Hippert. Phonon anomalies and the ferroelectric phase transition in multiferroic bifeo$_3$. *Phys. Rev. B*, 73:132101, Apr 2006.

[70] Tadej Rojac, Andreja Bencan, Barbara Malic, Goknur Tutuncu, Jacob L. Jones, John E. Daniels, and Dragan Damjanovic. BiFeO3 ceramics: Processing, electrical, and electromechanical properties. *Journal of the American Ceramic Society*, 97:1993–2011, 2014.

[71] J A Mejía Gómez, C Canaria, R Ochoa Burgos, C A Ortiz, G I Supelano, and C A Parra Vargas. Structural study of yttrium substituted bifeo3. *Journal of Physics: Conference Series*, 687(1):012091, feb 2016.

[72] H. D. Megaw and C. N. W. Darlington. Geometrical and structural relations in the rhombohedral perovskites. *Acta Crystallographica Section A*, 31(2):161–173, March 1975.

[73] J.M. Moreau, C. Michel, R. Gerson, and W.J. James. Ferroelectric bifeo3 x-ray and neutron diffraction study. *Journal of Physics and Chemistry of Solids*, 32(6):1315–1320, 1971.

[74] D. Lebeugle, D. Colson, A. Forget, M. Viret, P. Bonville, J. F. Marucco, and S. Fusil. Room-temperature coexistence of large electric polarization and magnetic order in BiFeo$_3$ single crystals. *Phys. Rev. B*, 76:024116, Jul 2007.

[75] Yu Xu and Mingrong Shen. Structure and optical properties of nanocrystalline bifeo3 films prepared by chemical solution deposition. *Materials Letters*, 62(20):3600–3602, 2008.

[76] J. F. Ihlefeld, N. J. Podraza, Z. K. Liu, R. C. Rai, X. Xu, T. Heeg, Y. B. Chen, J. Li, R. W. Collins, J. L. Musfeldt, X. Q. Pan, J. Schubert, R. Ramesh, and D. G. Schlom. Optical band gap of BiFeO3 grown by molecular-beam epitaxy. *Applied Physics Letters*, 92(14), 04 2008. 142908.

[77] S. J. Clark and J. Robertson. Band gap and Schottky barrier heights of multiferroic BiFeO3. *Applied Physics Letters*, 90(13), 03 2007. 132903.

[78] Yi Zhang, Haidong Lu, Xingxu Yan, Xiaoxing Cheng, Lin Xie, Toshihiro Aoki, Linze Li, Colin Heikes, Shu Ping Lau, Darrell G. Schlom, Longqing Chen, Alexei Gruverman, and Xiaoqing Pan. Intrinsic conductance of domain walls in BiFeO $_3$. *Advanced Materials*, 31(36):1902099, 2019.

[79] Axel Lubk, S. Gemming, and N. A. Spaldin. First-principles study of ferroelectric domain walls in multiferroic bismuth ferrite. *Phys. Rev. B*, 80:104110, Sep 2009.

[80] L.D. Landau and E.M. Lifshitz. On the theory of the dispersion of magnetic permeability in ferromagnetic bodies. *Phys. Z. Sowjetunion*, 8:153–164, 1935.

[81] Charles Kittel. Theory of the structure of ferromagnetic domains in films and small particles. *Phys. Rev.*, 70:965–971, Dec 1946.

[82] J F Scott. Nanoferroelectrics: statics and dynamics. *Journal of Physics: Condensed Matter*, 18(17):R361, apr 2006.

[83] G Catalan, J F Scott, A Schilling, and J M Gregg. Wall thickness dependence of the scaling law for ferroic stripe domains. *Journal of Physics: Condensed Matter*, 19(2):022201, dec 2006.

[84] A. K. Yadav, C. T. Nelson, S. L. Hsu, Z. Hong, J. D. Clarkson, C. M. Schlepütz, A. R. Damodaran, P. Shafer, E. Arenholz, L. R. Dedon, D. Chen, A. Vishwanath, A. M. Minor, L. Q. Chen, J. F. Scott, L. W. Martin, and R. Ramesh. Observation of polar vortices in oxide superlattices. *Nature*, 530(75897589):198–201, Feb 2016. container-title: Nature.

[85] Dorin Rusu, Jonathan J. P. Peters, Thomas P. A. Hase, James A. Gott, Gareth A. A. Nisbet, Jörg Strempfer, Daniel Haskel, Samuel D. Seddon, Richard Beanland, Ana M. Sanchez, and Marin Alexe. Ferroelectric incommensurate spin crystals. *Nature*, 602(7896):240–244, Feb 2022.

[86] Takashi Kurumaji, Taro Nakajima, Victor Ukleev, Artem Feoktystov, Takahisa Arima, Kazuhisa Kakurai, and Yoshinori Tokura. Néel-type skyrmion lattice in the tetragonal polar magnet vose$_2$o$_5$. *Phys. Rev. Lett.*, 119:237201, Dec 2017.

[87] S. D. Seddon, D. E. Dogaru, S. J. R. Holt, D. Rusu, J. J. P. Peters, A. M. Sanchez, and M. Alexe. Real-space observation of ferroelectrically induced magnetic spin crystal in srruo3. *Nature Communications*, 12, 2021.

[88] J. Sapriel. Domain-wall orientations in ferroelastics. *Phys. Rev. B*, 12:5128–5140, Dec 1975.

[89] Petr S. Bednyakov, Boris I. Sturman, Tomas Sluka, Alexander K. Tagantsev, and Petr V. Yudin. Physics and applications of charged domain walls. *npj Computational Materials*, 4(1):65, 2018. Number: 1.

[90] Chun-Lin Jia, Valanoor Nagarajan, Jia-Qing He, Lothar Houben, Tong Zhao, Ramamoorthy Ramesh, Knut Urban, and Rainer Waser. Unit-cell scale mapping of ferroelectricity and tetragonality in epitaxial ultrathin ferroelectric films. *Nature Materials*, 6(11):64–69, 2007.

[91] Tomas Sluka, Petr Bednyakov, Petr Yudin, Arnaud Crassous, and Alexander Tagantsev. *Charged Domain Walls in Ferroelectrics*, pages 103–138. Springer International Publishing, 2016.

[92] Donghwa Lee, Rakesh K. Behera, Pingping Wu, Haixuan Xu, Y. L. Li, Susan B. Sinnott, Simon R. Phillpot, L. Q. Chen, and Venkatraman Gopalan. Mixed bloch-néel-ising character of 180° ferroelectric domain walls. *Phys. Rev. B*, 80:060102, Aug 2009.

[93] Donghwa Lee, Rakesh K. Behera, Pingping Wu, Haixuan Xu, Y. L. Li, Susan B. Sinnott, Simon R. Phillpot, L. Q. Chen, and Venkatraman Gopalan. Mixed bloch-néel-ising character of 180° ferroelectric domain walls. *Phys. Rev. B*, 80:060102, Aug 2009.

[94] B Houchmandzadeh, J Lajzerowicz, and E Salje. Order parameter coupling and chirality of domain walls. *Journal of Physics: Condensed Matter*, 3(27):5163, jul 1991.

[95] M. H. Lee, C.-P. Chang, F.-T. Huang, G. Y. Guo, B. Gao, C. H. Chen, S.-W. Cheong, and M.-W. Chu. Hidden antipolar order parameter and entangled néel-type charged domain walls in hybrid improper ferroelectrics. *Phys. Rev. Lett.*, 119:157601, Oct 2017.

[96] Rik Brydson and Nicole Hondow. *Electron Energy Loss Spectrometry and Energy Dispersive X-ray Analysis*, chapter 7, pages 163–210. John Wiley & Sons, Ltd, 2011.

[97] C. Barry Carter and David B. Williams, editors. *Transmission Electron Microscopy*. Springer Cham, 2018.

[98] Jonathan Peters. *Structure and ferroelectricity at the atomic level in perovskite oxides*. PhD thesis, University of Warwick, 2017.

[99] Dorin Rusu. *Spin-like polar textures in ferroelectrics*. PhD thesis, University of Warwick, 2021.

[100] P. P. Ewald. *Fifty Years of X-Ray Diffraction*. Springer New York, NY, 2012.

[101] Michiyoshi Tanaka and Kenji Tsuda. Convergent-beam electron diffraction. *Journal of electron microscopy*, 60 Suppl 1:S245–67, 1994.

[102] Lewys Jones, Hao Yang, Timothy J. Pennycook, Matthew S. J. Marshall, Sandra Van Aert, Nigel D. Browning, Martin R. Castell, and Peter D. Nellist. Smart align—a new tool for robust non-rigid registration of scanning microscope data. *Advanced Structural and Chemical Imaging*, 1(1):8, 2015. Number: 1.

[103] F Hofer, F P Schmidt, W Grogger, and G Kothleitner. Fundamentals of electron energy-loss spectroscopy. *IOP Conference Series: Materials Science and Engineering*, 109(1):012007, 2016.

[104] TC Lovejoy, GC Corbin, N Dellby, MV Hoffman, and OL Krivanek. Advances in Ultra-High Energy Resolution STEM-EELS. *Microscopy and Microanalysis*, 24(S1):446–447, 08 2018.

[105] R. Resta, M. Posternak, and A. Baldereschi. Towards a quantum theory of polarization in ferroelectrics: The case of KNbO3. *Physical Review Letters*, 70(7):1010–1013, 1993.

[106] L. Bellaiche and David Vanderbilt. Intrinsic piezoelectric response in perovskite alloys: Pmn-pt versus pzt. *Physical Review Letters*, 83(7):1347–1350, 1999.

[107] Ralph Abraham, Jerrold E. Marsden, and Tudor Ratiu. *Manifolds, tensor analysis and Applications*. Addison-Wesley Publishing Company, 1983.

[108] Chun-Lin Jia, Knut W. Urban, Marin Alexe, Dietrich Hesse, and Ionela Vrejoiu. Direct observation of continuous electric dipole rotation in flux-closure domains in ferroelectric pb(zr,ti)o₃. *Science*, 331(6023):1420–1423, 2011.

[109] Ivan I Naumov, L Bellaiche, and Huaxiang Fu. Unusual phase transitions in ferroelectric nanodisks and nanorods. *Nature*, 432:737, 2004.

[110] Ivan Naumov and Alexander M. Bratkovsky. Unusual polarization patterns in flat epitaxial ferroelectric nanoparticles. *Phys. Rev. Lett.*, 101:107601, Sep 2008.

[111] Igor Kornev, Huaxiang Fu, and L. Bellaiche. Ultrathin films of ferroelectric solid solutions under a residual depolarizing field. *Phys. Rev. Lett.*, 93:196104, Nov 2004.

[112] S. Prosandeev and L. Bellaiche. Asymmetric screening of the depolarizing field in a ferroelectric thin film. *Phys. Rev. B*, 75:172109, May 2007.

[113] Bo-Kuai Lai, I. Ponomareva, I. I. Naumov, I. Kornev, Huaxiang Fu, L. Bellaiche, and G. J. Salamo. Electric-field-induced domain evolution in ferroelectric ultrathin films. *Phys. Rev. Lett.*, 96:137602, Apr 2006.

[114] Lewys Jones, Hao Yang, Timothy J. Pennycook, Matthew S. J. Marshall, Sandra Van Aert, Nigel D. Browning, Martin R. Castell, and Peter D. Nellist. Smart align—a new tool for robust non-rigid registration of scanning microscope data. *Advanced Structural and Chemical Imaging*, 1(8), 2015.

[115] Magnus Nord, Per Erik Vullum, Ian MacLaren, Thomas Tybell, and Randi Holmestad. Atomap: a new software tool for the automated analysis of atomic resolution images using two-dimensional gaussian fitting. *Advanced Structural and Chemical Imaging*, 3, 2017.

[116] Alexei Gruverman, Marin Alexe, and Dennis Meier. Piezoresponse force microscopy and nanoferroic phenomena. *Nature Communications*, 10(1661), 2019.

[117] A. Gruverman, D. Wu, and J. F. Scott. Piezoresponse force microscopy studies of switching behavior of ferroelectric capacitors on a 100-ns time scale. *Phys. Rev. Lett.*, 100:097601, Mar 2008.

[118] F. Zavaliche, P. Shafer, R. Ramesh, M. P. Cruz, R. R. Das, D. M. Kim, and C. B. Eom. Polarization switching in epitaxial BiFeO3 films. *Applied Physics Letters*, 87(25):252902, 2005.

[119] P. Paruch, T. Giamarchi, and J.-M. Triscone. Domain wall roughness in epitaxial ferroelectric $\mathrm{pbzr_{0.2}ti_{0.8}o_3}$ thin films. *Phys. Rev. Lett.*, 94:197601, May 2005.

[120] S. K. Streiffer, C. B. Parker, A. E. Romanov, M. J. Lefevre, L. Zhao, J. S. Speck, W. Pompe, C. M. Foster, and G. R. Bai. Domain patterns in epitaxial rhombohedral ferroelectric films. i. geometry and experiments. *Journal of Applied Physics*, 83(5):2742–2753, 1998.

[121] D. Lebeugle, D. Colson, A. Forget, M. Viret, A. M. Bataille, and A. Gukasov. Electric-field-induced spin flop in BiFeO3 single crystals at room temperature. *Phys. Rev. Lett.*, 100:227602, Jun 2008.

[122] M. Y. Gureev, A. K. Tagantsev, and N. Setter. Head-to-head and tail-to-tail 180-degree domain walls in an isolated ferroelectric. *Phys. Rev. B*, 83:184104, May 2011.

[123] J. Zhang, Y. J. Wang, J. Liu, J. Xu, D. Wang, L. Wang, X. L. Ma, C. L. Jia, and L. Bellaiche. Origin of sawtooth domain walls in ferroelectrics. *Physical Review B*, 101, 2 2020.

[124] Fei Xue, Yijia Gu, Linyun Liang, Yi Wang, and Long-Qing Chen. Orientations of low-energy domain walls in perovskites with oxygen octahedral tilts. *Phys. Rev. B*, 90:220101, Dec 2014.

[125] Richard Beanland. Structure of planar defects in tilted perovskites. *Acta Crystallographica Section A*, 67(3):191–199, 2011.

[126] Yi Wang, Chris Nelson, Alexander Melville, Benjamin Winchester, Shunli Shang, Zi-Kui Liu, Darrell G. Schlom, Xiaoqing Pan, and Long-Qing Chen. $bifeo_3$ domain wall energies and structures: A combined experimental and density functional theory+**U** study. *Phys. Rev. Lett.*, 110:267601, Jun 2013.

[127] Wen-Yuan Wang, Yun-Long Tang, Yin-Lian Zhu, Yao-Bin Xu, Ying Liu, Yu-Jia Wang, Suriyaprakash Jagadeesh, and Xiu-Liang Ma. Atomic level 1d structural modulations at the negatively charged domain walls in BiFeO3 films. *Advanced Materials Interfaces*, 2(9):1500024, 2015.

[128] Linze Li, Xiaoxing Cheng, Jacob R. Jokisaari, Peng Gao, Jason Britson, Carolina Adamo, Colin Heikes, Darrell G. Schlom, Long-Qing Chen, and Xiaoqing Pan. Defect-induced hedgehog polarization states in multiferroics. *Phys. Rev. Lett.*, 120:137602, Mar 2018.

[129] Linze Li, Yi Zhang, Lin Xie, Jacob R. Jokisaari, Christianne Beekman, Jan-Chi Yang, Ying-Hao Chu, Hans M. Christen, and Xiaoqing Pan. Atomic-scale

mechanisms of defect-induced retention failure in ferroelectrics. *Nano Letters*, 17(6):3556–3562, 2017. PMID: 28471679.

[130] Han Gao, Chao Chen, Lu You, Fei Sun, Chengliang Lu, Sijie Yang, Guofu Zhou, Deyang Chen, Yibo Han, and Jun-Ming Liu. Co-polarized second harmonic generation induced by ferroelectric domains and domain wall arrays. *Advanced Optical Materials*, 10(21):2200831, 2022.

[131] P. D. Nellist and S. J. Pennycook. The principles and interpretation of annular dark-field z-contrast imaging. *Advances in Imaging and Electron Physics*, 113:147–203, 1 2000.

[132] Pavel Marton, Mauro A. P. Gonçalves, Marek Paściak, Sabine Körbel, Věnceslav Chumchal, Martin Plešinger, Antonín Klíč, and Jirka Hlinka. Zigzag charged domain walls in ferroelectric PbTiO3. *Physical Review B*, 107(9):094102, 2023.

[133] Jucheol Park, Sung Heo, Jae-Gwan Chung, Heekoo Kim, HyungIk Lee, Kihong Kim, and Gyeong-Su Park. Bandgap measurement of thin dielectric films using monochromated stem-eels. *Ultramicroscopy*, 109(9):1183–1188, 2009.

[134] M. Stöger-Pollach. Optical properties and bandgaps from low loss EELS: Pitfalls and solutions. *Micron*, 39(8):1092–1110, 2008.

[135] Ian MacLaren, Liqiu Wang, Alan J. Craven, Quentin M. Ramasse, Bernhard Schaffer, Kambiz Kalantari, and Ian M. Reaney. The atomic structure and chemistry of fe-rich steps on antiphase boundaries in ti-doped Bi0.9Nd0.15FeO3. *APL Materials*, 2, 6 2014.

[136] I. MacLaren, B. Sala, S. M.L. Andersson, T. J. Pennycook, J. Xiong, Q. X. Jia, E. M. Choi, and J. L. MacManus-Driscoll. Strain localization in thin films of Bi(Fe,Mn)O3 due to the formation of stepped Mn4+ rich antiphase boundaries. *Nanoscale Research Letters*, 10, 12 2015.

[137] Nicola A. Spaldin, Ipek Efe, Marta D. Rossell, and Chiara Gattinoni. Layer and spontaneous polarizations in perovskite oxides and their interplay in multiferroic bismuth ferrite. *The Journal of Chemical Physics*, 154(15):154702, 2021.

[138] P. A. van Aken, B. Liebscher, and V. J. Styrsa. Quantitative determination of iron oxidation states in minerals using fe l2,3-edge electron energy-loss near-

edge structure spectroscopy. *Physics and Chemistry of Minerals*, 25(5):323–327, 1998.

[139] H.K. Schmid and W. Mader. Oxidation states of mn and fe in various compound oxide systems. *Micron*, 37(5):426–432, 2006. Proceedings of the International Workshop on Enhanced Data Generated with Electrons (EDGE).

[140] Haiyan Tan, Jo Verbeeck, Artem Abakumov, and Gustaaf Van Tendeloo. Oxidation state and chemical shift investigation in transition metal oxides by eels. *Ultramicroscopy*, 116:24–33, 2012.

[141] Ragnhild Sæterli, Sverre Magnus Selbach, Ponniah Ravindran, Tor Grande, and Randi Holmestad. Electronic structure of multiferroic $bifeo_3$ and related compounds: Electron energy loss spectroscopy and density functional study. *Phys. Rev. B*, 82:064102, Aug 2010.

[142] M. D. Rossell, R. Erni, M. P. Prange, J.-C. Idrobo, W. Luo, R. J. Zeches, S. T. Pantelides, and R. Ramesh. Atomic structure of highly strained $bifeo_3$ thin films. *Phys. Rev. Lett.*, 108:047601, Jan 2012.

[143] F. M. F. de Groot, M. Grioni, J. C. Fuggle, J. Ghijsen, G. A. Sawatzky, and H. Petersen. Oxygen 1s x-ray-absorption edges of transition-metal oxides. *Phys. Rev. B*, 40:5715–5723, Sep 1989.

[144] James H. Paterson and Ondrej L. Krivanek. Elnes of 3d transition-metal oxides ii variations with oxidation state and crystal sffucture. *Untramicroscopy*, 1990.